Progress in Particle and Nuclear Physics 114 (2020) 103790

Contents lists available at ScienceDirect

Progress in Particle and Nuclear Physics

journal homepage: www.elsevier.com/locate/ppnp

Review

Low energy nuclear physics with active targets and time projection chambers

D. Bazin [a,b,*], T. Ahn [c], Y. Ayyad [a], S. Beceiro-Novo [b], A.O. Macchiavelli [d], W. Mittig [a,b], J.S. Randhawa [a]

[a] National Superconducting Cyclotron Laboratory, 640 S. Shaw Lane, East Lansing, MI 48824-1321, United States
[b] Department of Physics and Astronomy, Michigan State University, East Lansing, MI 48824-1321, United States
[c] Department of Physics, University of Notre Dame, 225 Nieuwland Science Hall, Notre Dame, IN 46556, United States
[d] Nuclear Science Division, Lawrence Berkeley National Laboratory, Berkeley, CA 94720, United States

ARTICLE INFO

Article history:
Available online 15 May 2020

Keywords:
Active target
Time projection chamber
Nuclear reactions
Nuclear spectroscopy
Nuclear decay
Nuclear astrophysics

ABSTRACT

This article aims at covering various low energy nuclear physics themes that can benefit from taking advantage of active targets and time projection chambers. They are naturally oriented towards the study of short-lived radioactive nuclei, for which high efficiency and thick targets are necessary to boost the luminosity of the experiments due to the weak intensity of the available beams. The use of active targets is particularly crucial when the recoil energy of the kinematically important particle is small and looses too much energy or does not emerge from a solid target.

Contents

* Corresponding author at: National Superconducting Cyclotron Laboratory, 640 S. Shaw Lane, East Lansing, MI 48824-1321, United States.
E-mail address: bazin@nscl.msu.edu (D. Bazin).

https://doi.org/10.1016/j.ppnp.2020.103790
0146-6410/

1. Introduction

The past decade has seen a rapid increase of the number of active targets implemented in time projection chambers used in low energy nuclear physics experiments. This growth is directly linked to two main factors: the availability of radioactive beams with good emittance properties, and the technological advances in time projection chambers used as active targets. Because many nuclear reactions performed with radioactive beams are done in inverse kinematics, the energies of the recoil particles that carry the kinematic information of the reaction can vary over a wide range. The low intensities of these beams severely limit the luminosity of experiments that use inert- or passive -materials as targets. An increase in target thickness can mitigate this limitation, but at the expense of the resolutions that can be achieved, and a difficult compromise has to be reached between luminosity and resolution that can impact the quality of the data and scientific reach of the experiment.

Active targets directly address this issue by using the target material as the detector medium simultaneously. As the vertex of the reactions can be determined for each event, there is no impact of the target thickness on the determination of the energies of the particles before and after the reaction. Likewise, recoil particles of low energies do not need to escape a layer of inert target material to be detected, therefore the target thickness can be increased without impacting the energy and angular resolutions. In addition, the implementation of active targets in time projection chambers allows a large solid angle coverage of the emitted reaction products, which further contributes to the increase in luminosity.

Although the number of applications of active targets and time projection chambers keeps increasing, they have now reached a level from which the physics themes they cover can be reviewed. It is the aim of this work to provide the reader with an overview of some of the nuclear physics subjects that can take advantage of this new experimental technique. For more details on existing active targets that are in operation and the technologies they employ, the reader is referred to previous reviews [1] and [2], respectively. The topics covered in the following chapters is a collection of low energy nuclear physics themes related to the study of the nucleus in its various degrees of freedom. After a section dedicated to the experimental methods and observables that are relevant to active targets, the subsequent sections are organized in a topical manner: the study of shell evolution in nuclei as their isospin is varied (Section 3), followed by the effects of pairing on the strong force that binds nuclei together (Section 4), and clustering effect in nuclei (Section 5). Then comes a section on studies of exotic decay modes (Section 6), fusion–fission process (Section 7) and studies of reactions that are of interest for nuclear astrophysics (Section 8). Finally, the last section is devoted to other direct reactions, in particular

Table 1
List of active-target detectors mentioned in this review. The laboratory acronyms are as follows: NSCL (National Superconducting Cyclotron Laboratory, USA), FRIB (Facility for Rare Isotope Beams, USA), Leuven (Katholieke Universiteit Leuven, Belgium), GANIL (Grand accelérateur d'ions lourds, France), Texas A&M (Texas A&M University, USA), RCNP (Research Center for Nuclear Physics, Japan), CENBG (Centre d'Études Nucléaires de Bordeaux-Gradignan, France), Warsaw (University of Warsaw, Poland), GSI (Helmholtzzentrum für Schwerionenforschung, Germany), LLNL (Lawrence Livermore National Laboratory, USA), ANL (Argonne National Laboratory, USA), CNS (Center for Nuclear Studies, Japan).

Name	Location	Main physics theme	Reference	Section(s)
pAT-TPC	NSCL/FRIB	Cluster structure	[3]	5.3.1, 5.3.3, 6.2, 7.2, 8.2.2, 8.3
AT-TPC	NSCL/FRIB	Shell evolution	[4]	2, 3.2.1, 4.3, 4.4, 6.4, 7.1, 7.3, 8.2.2, 9.1
SPECMAT	Leuven	Shell evolution	[5]	2.1, 6.4
MAYA	GANIL	Giant resonances	[6]	2.1, 4.2, 7.3, 9.4
ACTAR	GANIL	Shell evolution	[7]	2.1, 3.2.2, 7.1, 7.3
TexAT	Texas A&M	Shell evolution	[8]	3.2.2, 6.4
MAIKo	RCNP	Cluster structure	[9]	5.3.2
TPC	CENBG	Exotic decays	[10]	6.3
O-TPC	Warsaw	Exotic decays	[11]	6.2, 6.3
MUSIC	GSI	Fusion–fission	[12]	7.1
fissionTPC	LLNL	Fusion–fission	[13]	7.1
MUSIC	ANL	Astrophysics	[14]	8.2
GADGET	NSCL/FRIB	Astrophysics	[15]	6.4
IKAR	GSI	Matter distributions	[16]	9.2
CAT	CNS	Giant resonances	[17]	9.3

those that involve higher beam energies (Section 9). Each section ends with a short summary that captures the main motivations for using this type of detector for this particular topic.

There is a number of active target time projection chambers that are mentioned in this review. To give an overview and facilitate readability and cross reference, they are listed in Table 1, indicating their (primary) location, (primary) use, reference and section(s) where they appear.

2. Experimental methods and observables

The purpose of this section is to introduce a number of general remarks on the experimental methods and observables that are most relevant with active targets, since the methods used to perform these measurements are common to all physics themes covered in this article.

2.1. Inverse kinematics

The main focus of using active target time projection chambers is based on the use of radioactive beams in inverse kinematics. It has already been discussed for instance in [1] how active targets can boost the luminosity of such experiments that usually suffer from weak beam intensities. Performing reactions in inverse kinematics is challenging experimentally because the kinematic properties of the reaction can usually not be extracted accurately from the heavy recoil. Instead, the light partner of the reaction must be detected in the exit channel to reach the level of accuracy necessary to characterize the reaction. Because this light partner is at rest before the reaction, its energy and scattering angle in the laboratory frame vary enormously as a function of the center-of-mass angle. This has several implications: (i) at the low energy range it becomes difficult for the light partner to escape the target, or its energy loss becomes too large, and (ii) a wide range of scattering angles needs to be covered in the laboratory frame in order to achieve a reasonable solid angle coverage of the reaction. The comparison between normal and inverse kinematics is illustrated by an example in Fig. 1 for the case of the transfer reaction ^{38}S(d,p). The properties of the emitted proton are much more challenging experimentally in the case of inverse kinematics. It is clear from this figure that the measurement of the scattering angle in inverse kinematics is critical to recover a good energy resolution, whereas it is much less important in normal kinematics.

Active targets are particularly well suited to address these issues. Because the light recoiling particle can be detected directly without having to escape an inert amount of target material, the low-energy detection limit is greatly reduced. At the same time, increasing the target thickness does not induce any loss of resolution, because the vertex location and, therefore, the energy of each reaction can be determined. Finally, the gas volume in which the reactions take place acts as a near-4π geometry that greatly enhances the detection efficiency. The scattering angle regions where efficiency is likely to suffer the most are those close to the beam direction, both in forward and backward directions, due to the large ionization and possible screening effects from the beam particles.

The wide energy range of the light recoil can be covered in different ways. Some active target concepts place the active volume inside a wide bore solenoid in order to apply a magnetic field aligned with the beam direction. The resulting curvature of the charged particle's tracks has two effects. The trajectories of the particles are lengthened within the active volume, up to their total range depending on their energy and the strength of the field. The measured range can be directly related to the energy of the particles, with a typical accuracy of 5% [3]. Secondly, the curvature of the trajectory gives a

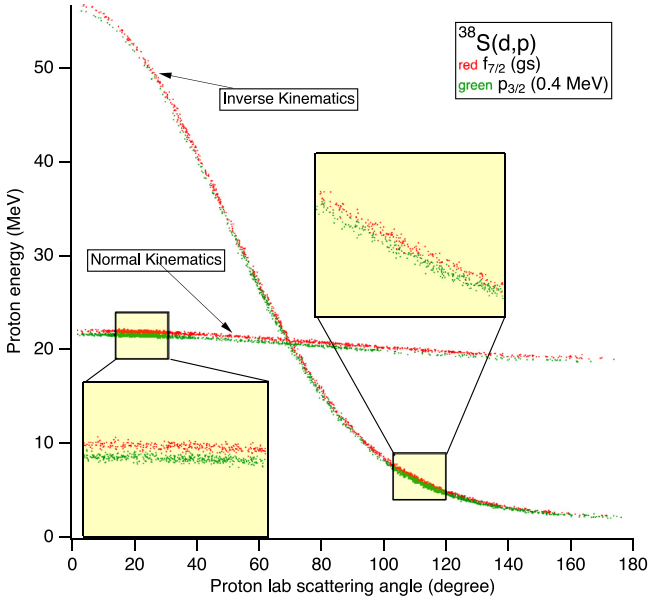

Fig. 1. Comparison between normal and inverse kinematics properties of the light recoil in the laboratory frame for a ^{38}S(d,p) reaction at 10 MeV/u. This plot shows the energy of the recoiling protons as a function of the laboratory scattering angle, simulated for both the ground state ($f_{7/2}$ gs in red) and an excited state at 0.4 MeV ($p_{3/2}$ in green). The energy and angular resolutions used in the simulations are 0.2 MeV FWHM and 1 degree FWHM respectively. Note that the yield distributions are reversed in the laboratory frame between the normal and inverse kinematics for this particular reaction, and that the same number of events were simulated for both final states. The two inserts show details of the plotted events near the maxima of the angular distributions in the center-of-mass frame. Whereas in normal kinematics the two states are clearly separated, this is no longer the case in inverse kinematics, even though all experimental conditions are the same. This illustrates the added difficulty in performing reactions in inverse kinematics, due to the strong dependence of the recoil energy on the scattering angle. A much better angular resolution is required in inverse kinematics in order to experimentally separate final states. Fortunately, Time Projection Chambers have typical angular resolutions below 1 degree, for instance the angular resolution of a track 200 millimeters long assuming a 0.5 millimeter position resolution would be 2.5 mrad or 0.14 degree. Note that this effect is common to most reactions performed in inverse kinematics, and does not depend on the detector used in the experiment.

measure of the particle's magnetic rigidity, also related to its energy and mass-to-charge ratio. Combining the magnetic rigidity information with the kinematics properties of the emitted particles can be used for particle identification and the identification of elastic and inelastic channels. This is the approach used in the AT-TPC [4] and SPECMAT [5] active-target detectors.

Another concept for dealing with the wide range of energies is combining the active gas volume detection with conventional Silicon and scintillator technologies that cover much of the geometry of the active target. The usual energy-loss vs. total-energy measurements can then be used to identify and characterize the light recoils that leave the active volume due to their large energy. This type of geometry is inherently smaller to limit the cost of covering a large solid angle with an expensive detector. This is the approach used in the MAYA [6] and ACTAR [7] active-target detectors for instance.

2.2. Excitation functions

Excitation functions show the evolution of a particular cross section as a function of the reaction energy. They can be directly extracted from active target data using energy loss tables: as the beam particles travel through the gas medium, they slow down progressively from electromagnetic interactions with the gas molecules. Therefore, a determination of the vertex location of a reaction can be directly related to the energy at which it occurred. The range of energies covered in the excitation function can be tuned using the incident beam energy as well as the gas pressure for a given length in the beam direction.

The energy resolution achieved with this method depends on two factors. The first is the energy resolution of the incoming beam. This is especially critical when using radioactive beams that are produced via nuclear reactions, because of the wide momentum width involved in this type of reaction. To attain energy resolutions below 50 keV typically requires to produce the radioactive beams from a thermalized source injected into a post-accelerator, as opposed to directly from nuclear reactions. The second is the position resolution of the reaction vertex location measurement in the direction of the beam. The resolution obtained for this parameter depends on many details of the detector, including the drift direction of the electrons released by the particle's ionization with regard to the beam direction. When the two are perpendicular, the geometry of the pad plane and its granularity determine the vertex location resolution, whereas when

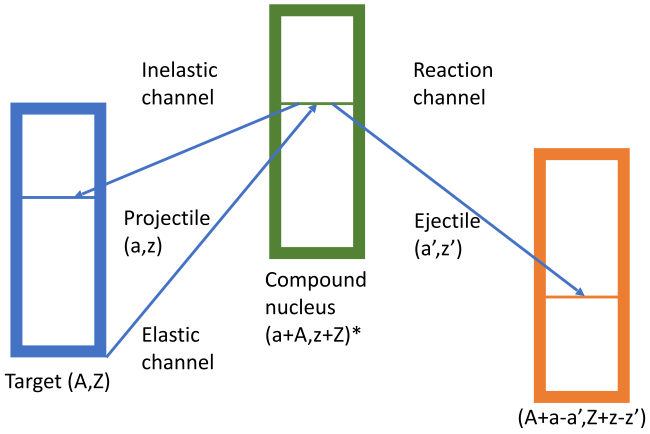

Fig. 2. Illustration of the population of resonant states (or simply resonances) in a compound nucleus briefly created during a nuclear collision, followed by its de-excitation into either the same components or different ones when some nucleons are transferred. Note that it is possible for some reactions to proceed via an excited state of the target or projectile, offering the rather unique possibility to deduce spectroscopic factors between excited states of different nuclei.

they are parallel the shaping time of the signals and the time resolution of the digital electronics system recording the pulses are the important factors. Typical resolution obtained in examples shown below are close to a few millimeters [4], which correspond to energy resolutions of about 50 keV typically for excitation functions.

The physical phenomena that are probed with excitation functions are prominently resonances. A resonance is usually interpreted as a compound nucleus state that lives significantly longer than the transition time of the projectile. Resonances can be either isolated if their width is smaller than the mean energy difference between their centroids, or overlapping if that is not the case.

The transition probability from a single particle resonant state can be written as a characteristic width

$$\Gamma_{sp} = \frac{2\hbar^2}{mr^2} P_l(E) \tag{1}$$

where P_l is the penetrability, m the reduced mass and r the channel radius [18]. The spectroscopic factor that measures the amount of single-particle configuration in the wave function is $S = \Gamma_{experimental}/\Gamma_{sp}$ [19] where $\Gamma_{experimental}$ is deduced from fitting the experimental excitation function with a model of the reaction. Note that spectroscopic factors are always model-dependent and are therefore not observables [20]. Compared to transfer reactions like for instance (d, p), where overlaps with the ground state can only be extracted, resonance reactions can be used to obtain them between excited states (see Fig. 2).

2.3. Scattering-angle distributions

The polar scattering angle of the recoil particles after a reaction is an essential observable that can be used in various ways to extract information about the nuclear states involved in the reaction. In an active-target detector, it can be deduced from the measured trajectory information of the recoil particle relative to the beam axis. The influence of the incoming beam quality can be significant if its position and angular spreads are large, as is often the case for radioactive beams directly extracted from a nuclear reaction. Unlike for the energy spread discussed in the previous Section 2.2, however, active-target detectors offer the possibility to measure the positions and angles of the beam particles on an event-by-event basis, and, therefore, mitigate the effects of a large geometrical emittance.

The extraction of the scattering angle from track data is relatively straightforward when no magnetic field is present and the electron drift field of the TPC is uniform. A method particularly well suited in this case is the RANdom SAmple Consensus model (RANSAC) that has been successfully applied to AT-TPC data taken on elastic scattering where a resolution of about 1° was obtained [21]. Another determination gave a resolution of 0.12° [22], however, from a detector with drastically different geometry and using a laser beam instead of charged particles from a nuclear reaction. The determination of the scattering angle becomes more involved when a magnetic field is applied that bends the trajectories of the recoil particles. In this case the location of the reaction vertex discussed in the previous Section 2.2 plays a crucial role in determining the beginning of the recoil track where the scattering angle corresponds to the tangent to the curved trajectory. An example of the complex analysis required can be found in Ref. [4].

Differential cross section distributions as a function of scattering angle are the primary observable used, for instance, in transfer reactions to extract the ℓ-value of the transferred nucleon (see Section 3.1). The scattering-angle selection of excitation functions also plays a crucial role in the identification of resonances and their comparison with theoretical

calculations (see Section 3.2.1). Finally, as mentioned in Section 2.1, the large dependence of the recoil energy on the scattering angle due to inverse kinematics directly affects the ability to separate excited states populated in nuclear reactions, for which a kinematically corrected energy has to be extracted, and where the resolution of the scattering angle measurement plays a dominant role.

2.4. Kinetic energy and particle identification

The identification of the recoil particles and the measurement of their kinetic energy are intimately related. The classic method for identification of light recoils such as p, d, ^{3}He, and so forth, uses energy-loss and total kinetic-energy measurements. The number of electrons collected from the gas ionization is directly related to the energy deposited by the particles in the active volume, and assuming the particles stop inside the volume, provides a measure of their total kinetic energy. The energy loss can be extracted from the amount of charge deposited by the particles at the beginning of the tracks. However, because of the fluctuations in gain inherent to the electron amplification process that takes place at the level of the sensor plane, the resolution is only in the range of 5%–10% [3,22]. Another method for measuring the kinetic energy relies on the length of the trajectories, or range, and is usually more accurate, with results down to a few percent [3].

When the recoil particle energies are too large to stop in the active volume however, the range method cannot be used and only the energy loss can be obtained from the charge measurement. Two different approaches are then used to extend kinetic energy measurement and particle identification to higher energies. The first relies on the addition of solid-state detectors such as Silicon diodes and/or CsI scintillators to capture the escaping particles and stop them while measuring their energies. This is the method used in the ACTAR detector for instance [7] where these detectors are placed on the walls of the active target chamber. The second method consists of adding a magnetic field aligned with the electron drift electric field applied in the active volume. The curvature of the charged particle trajectory induced by the magnetic field B is related to its velocity v via the relation

$$B\rho = 3.107\beta\gamma\frac{A}{Q} \tag{2}$$

where ρ is the radius of curvature in meters, $\beta = v/c$, γ is the relativistic factor, and A, Q are the mass and charge number of the particle, respectively. $B\rho$ in Tesla$\times$meter is the magnetic rigidity of the particle. Since for light particles the ionic charge is equal to the atomic number, the magnetic rigidity obtained from the radius of curvature of their trajectories can be used for particle identification, however the procedure is more complex because it also involves the measurement of their energy loss as well as their scattering angle. Combining these various measurements, it is possible to establish criteria that can distinguish between particles that originate from different reaction channels. An example is best to illustrate this rather unusual method. Fig. 3 shows a Monte-Carlo simulation of the reconstructed magnetic rigidity, scattering angle and deposited charge for four different reaction channels induced by a 9 MeV/u ^{10}Be beam on a deuterium target. The separation between the different channels relies on these three parameters rather than the usual energy loss vs. total energy identification performed with solid-state detectors. The parameters result from simple fits of the point cloud extracted from each simulated track.

Finally, methods based on machine learning algorithms that can provide efficient particle identification via event classification are being considered. These methods are still in early stages of development, but a recent attempt shows for instance how neural networks can be used to separate scattering events on protons or ^{12}C based only on the image data from the sensor plane of an active-target detector [23].

3. Shell evolution

It is now well established that the shell closures observed in stable nuclei are not conserved across the chart of nuclei, and that the corresponding magic numbers can vanish with changing numbers of neutrons or protons, while new ones can appear [24]. The breakdown of the N=28 neutron shell closure for instance is well known and illustrated by the evolution of collectivity across the N=28 shell closure for different isotopic chains. Fig. 4 shows the evolution of the first 2^+ states and the transition strength of their decay to the ground state in even–even isotopes. While N=28 is still a magic number in ^{48}Ca, it quickly vanishes as the number of protons is reduced. This kind of behavior is rooted in the evolution of single-particle energies, themselves subject to changes in the various components of the nuclear force. A well-known example is found in the effects of the monopole average of the central and spin–isospin components of the nuclear force [25,26] that can drive the evolution of single-particle energies based on the relative angular momentum of the valence nucleons. Another component of the strong force that affects the evolution of shell structure and the reordering of orbitals is the three-nucleon force, that has been shown to play a major role in the evolution of single-particle energies, and for instance explain the location of the neutron drip-line in oxygen isotopes [27].

These developments are intimately tied to the tremendous theoretical progress on new methods to solve the many-body problem and optimize the Hamiltonians to make the calculations practical and reliable [29]. The so-called ab-initio methods that attempt to describe the nucleus from first principles [30], and were initially limited to light nuclei only (lighter than ^{12}C), are now able to reach much heavier and complex nuclei, where the evolution of shell gaps is observed

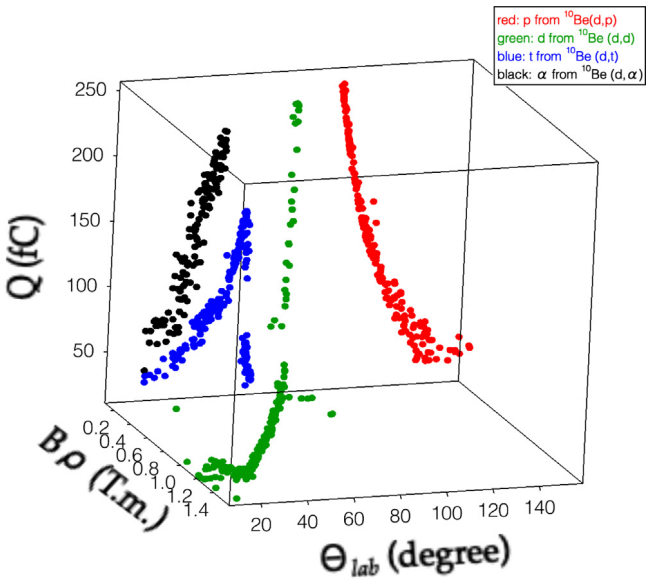

Fig. 3. Simulation of the identification of four reaction channels induced by a 9 MeV/u ^{10}Be beam on a deuterium active target placed in a magnetic field. The four reactions are simulated with their relevant kinematics, flat angular distributions and equal number of events to better visualize the differences between channels. The three parameters used to build this 3-dimensional spectrum are the magnetic rigidity ($B\rho$), scattering angle in the laboratory frame (Θ_{lab}), and deposited charge inside the target (Q). In this geometry where the magnetic field is parallel to the beam axis, the scattering angle is obtained from fitting the two projections perpendicular to the beam axis with sine line shapes. The magnetic rigidity is obtained from a fit of the radius of curvature of the hit pattern on the pad plane, and subtracting the effect of the scattering angle. The charge Q is simply the amount of charge collected on the pad plane.

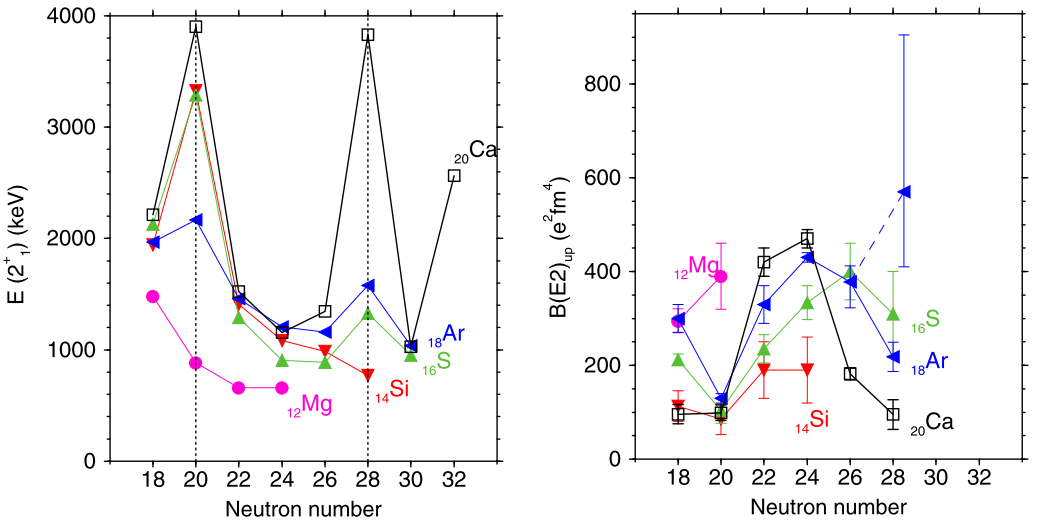

Fig. 4. Evolution of the first 2^+ states and their transition strength B(E2) for even–even isotopes along the isotopic chains from Z=12 (Mg) to 20 (Ca). The single-particle characteristic high energy and low strength observed in the doubly magic nucleus ^{48}Ca progressively gives way to lower energies and larger strengths signaling the onset of collectivity as the number of protons is reduced.
Source: From [28].

experimentally. The study of the single-particle structure of nuclei away from stability is therefore a crucial ingredient in testing and shaping the models that describe their static properties.

One of the emerging features of shell evolution is orbital inversion, where an orbital in the normal ordering of the single-particle sequence becomes energetically more favorable than the ones below. This phenomenon has been observed in light nuclei such as in ^{11}Be for instance where the $1/2^+$ ground state is a clear indication of an inversion between the $0p_{1/2}$ and $1s_{1/2}$ orbitals, and extracted spectroscopic factors relative to ^{12}Be illustrate the breakdown of the N=8 magic number in that nucleus [31]. Another famous example is the so-called "island of inversion" centered around ^{32}Mg, where

several nuclei exhibit similar inversions as well as large deformations (see for instance [32]). It is becoming clear that this type of phenomenon is widespread within the nuclear chart, in particular on the neutron-rich side, and has therefore become a very active area of research, both experimentally and theoretically. For example the N=40 region centered around ^{64}Cr [33], or more recently the region predicted to lie beyond the N=50 neutron shell closure [34], which has sparked recent experimental results on the doubly magic nucleus ^{78}Ni [35]. However, as the production of neutron-rich nuclei that exhibit these properties gets ever more challenging with increasing mass, the experiments that use these weak beams have to rely on new techniques to recover the luminosity necessary to perform meaningful measurements. The use of active target time projection chambers is emerging as one of the promising concepts that can achieve this goal.

Experimentally, the study of shell evolution has been conducted using a variety of techniques, from β-decay spectroscopy to reaction-based methods ranging from transfer reactions to quasi-elastic proton scattering at relativistic energies. In this section we explore the impact of using active target time projection chambers on some of these techniques and how this new technology is helping pushing the limits of these studies, in particular for studying shell evolution in rare isotopes. The particular use of pair transfer reactions to study shell evolution near islands of inversion is covered in Section 4.4.

3.1. Transfer reactions

Transfer reactions have been and continue to be used extensively to probe the single-particle nature of nuclear states. They can also reveal pairing correlations and collective degrees of freedom. First developed in experiments with light nuclear beams on stable targets, they have more recently been extended to experiments in inverse kinematics using radioactive beams. There are many examples in the literature of how they can be used to probe the occupancy in various orbitals [36] and to extract spectroscopic factors between nuclear states, for instance leading to the observation of quenching with respect to independent particle models [37]. It is therefore essential to extend the use of transfer reactions to rare isotopes where new features and phenomena are often found in nuclear physics.

However, as explained in Section 2.1, the experimental conditions of inverse kinematics are very challenging. A clever solution to the inverse kinematics challenges has been implemented in the HELIOS solenoid spectrometer [38] that converts the scattering angle measurement into a position measurement, eliminating the energy resolution losses due to the energy compression effect of inverse kinematics when using conventional telescope technology. Some examples of the excellent results obtained with this technique can be found in [39] and [40]. Nevertheless, the solenoid spectrometer method remains limited to beam intensities greater than a few 10^4 particles per second, and a compromise between target thickness and resolution is still necessary. Using an active target for beam intensities below the above limit seems therefore like a logical step. The identification of the angular momentum of the transferred nucleon is based on the comparison of the scattering angle distributions with scattering theory calculations such as Distorted Wave Born Approximation (DWBA). Since in active targets the reaction can happen at a wide range of energies, from the incident beam energy to almost 0, the accumulated angular distribution would be washed out by the variation of the diffraction pattern with energy. However, as demonstrated in Fig. 5, this variation scales approximately as $\sqrt{E}$ where E is the beam energy at the location where the reaction takes place within the target. By using the combined parameter $\Theta_{cm}\sqrt{E}$ instead of just Θ_{cm} to accumulate statistics on the angular distributions, it is therefore possible to keep a good identification of the l-value of the transferred nucleon.

Although there is not yet examples of transfer reaction studies using active targets at the time of this writing, several proposals and programs are already under way to take advantage of the high luminosity provided by this type of device. Due to their near-4π solid-angle coverage, active targets can detect many open channels simultaneously, hence boosting the scientific value of experiments. In particular, elastic and inelastic scattering channels are always going to be present and dominant in any experiment. The elastic channel is of interested on its own (see following section), if not just to constrain the optical model parameters that are used in the transfer reaction calculations. This inclusiveness of active targets can pose some difficulty when the sought cross sections are small compared to other channels, although some methods to filter events originating from different reactions are possible (see Section 2.4 and Fig. 3). In addition, the first attempts at using machine learning techniques to classify events in this type of imaging device seem very promising [23].

The determination of spectroscopic factors using transfer reactions is a well-known technique. However, it is subject to large uncertainties due to the model-dependency rooted in the choice of optical model parameters used in the calculations. At or below the Coulomb barrier, transfer reactions can be used to determine the Asymptotic Normalization Coefficients (ANC), which are a measure of the extent of the tail of the nuclear wave function. There are prospects to reduce the model-dependency using measurements above and below the Coulomb barrier [41]. This method could be favorably implemented using active targets, thanks to the large range of energies at which transfer reactions can be measured as the beam slows down in the gas. With cross sections measured above and below the Coulomb barrier, both spectroscopic factors and ANC could be deduced from a single experiment.

3.2. Resonant proton scattering

3.2.1. Spectroscopic factors

An alternate method to explore the single-particle structure of unstable nuclei is via the population of resonances in light particle scattering such as protons. This method was used extensively on stable targets since proton beams became

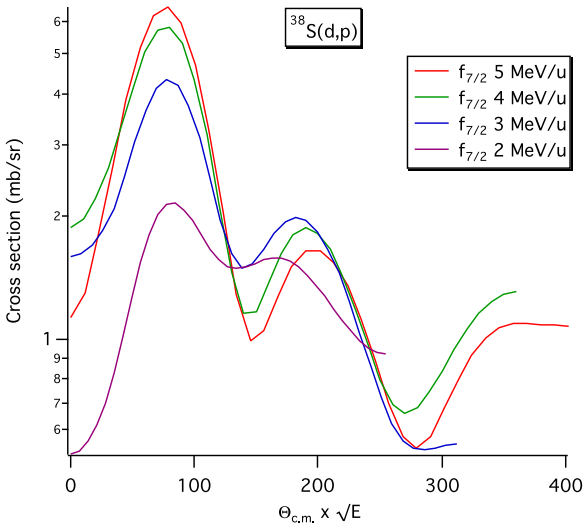

Fig. 5. Calculated scattering angle distributions in the reaction ^{38}S(d,p) at different incident energies, plotted as a function of $\Theta_{cm}\sqrt{E}$. Even though the diffraction pattern of the distributions varies significantly with energy, they can be reconciled and experimentally accumulated when plotted as a function of this combined parameter.

available from Tandem accelerators. By measuring the strength of $T_>$ analog resonances in a ^{A}Z + proton compound system, spectroscopic factors related to the corresponding neutron-rich $^{A+1}$Z nucleus could be inferred using isospin symmetry. The $T_>$ resonances can be observed on top of a background consisting of Rutherford scattering and $T_<$ resonances in an excitation function measurement. Because of the high level density of $T_<$ states above the ^{A}Z + proton threshold, the usual procedure is to average them out by smoothing the excitation function curves to a given energy resolution. Examples of such experiments can be found in [42] for instance for the ^{40}Ar + p system. Series of articles describe comparisons between results obtained with this method and (d,p) transfer reaction results [43–46]. The agreement in the determination of spectroscopic factors is in general good, although it is well known that model dependency plays an important role, especially in the choice of the optical potential used to calculate the single-particle cross sections for transfer reactions. This sensitivity is less pronounced in the model-dependency of R-matrix calculations used to extract spectroscopic factors from analog resonances.

As important as these studies were, they were limited to stable targets. The measurement of elastic and inelastic scattering excitation functions on protons in inverse kinematics is now enabling these experiments on radioactive nuclei. Although the statistics are still far from what was achieved with proton beams, the first result obtained with a ^{46}Ar beam are encouraging. In Fig. 6, a normalized excitation function obtained for this reaction using the AT-TPC [4] could be measured [47] and spectroscopic factors extracted via a comparison with R-Matrix calculations. This recent example demonstrates the potential of active targets in reviving the proton resonant scattering method for extracting spectroscopic factors on radioactive nuclei, in particular on the neutron-rich side.

3.2.2. Unbound states

Unbound resonant states play an increasingly important role in nuclear spectroscopy as the studied nuclei approach or even cross the drip lines. They directly relate to the evolution of shell structure far from stability by probing nuclear excitations that are located in the continuum. They also pose a particular challenge to nuclear structure models that must include the effects of the continuum. In weakly bound nuclei close to the drip lines, the density of $T_<$ resonances is low and resonant proton scattering can be used to study individual unbound excited states, or even the ground state of an unbound nucleus. Recent examples that used proton resonant scattering on ^{9}C and ^{8}B radioactive beams to study resonances in ^{10}N [48] and ^{9}C [49], respectively, were obtained with the TexAT active target [8]. Excitation functions measured in two different ranges of scattering angles are shown in Fig. 7 for resonances in ^{9}C. Another recent result using the ACTAR active-target detector [7], although not performed with a radioactive beam, further supports the idea of performing this type of reaction in inverse kinematics for spectroscopy studies. The geometry of the ACTAR and TexAT detectors enables measurements at backward angles in the center-of-mass frame, where the effects of the nuclear potential are more pronounced. Fig. 8 shows the results obtained in [7] during a commissioning run using an ^{18}O in inverse kinematics on an isobutane target.

3.3. Summary and outlook

The study of shell evolution is a major topic in nuclear physics. Although several other methods involving beams with energies far above the Fermi energy are actively used, the two methods presented above (transfer reactions and proton

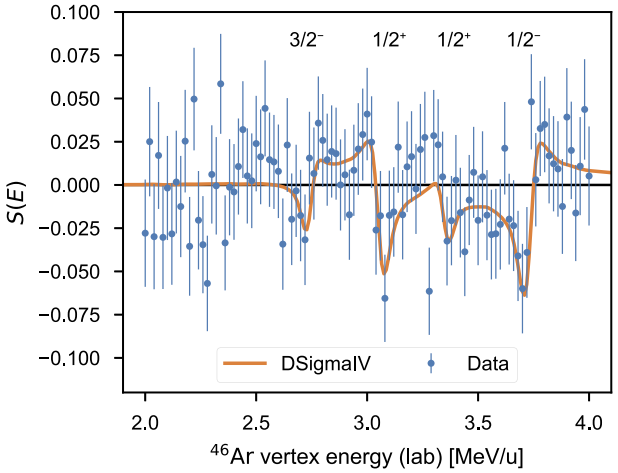

Fig. 6. Normalized excitation function S(E) (defined in [47]) of the proton scattering on ^{46}Ar in inverse kinematics measured in the AT-TPC. The spin/parity assignment of the resonances is based on comparison with R-Matrix calculations. The spectroscopic factors are extracted from the strength of the resonances. Note that only the negative parity resonances correspond to analog states in the ^{47}Ar nucleus.
Source: Taken from [47].

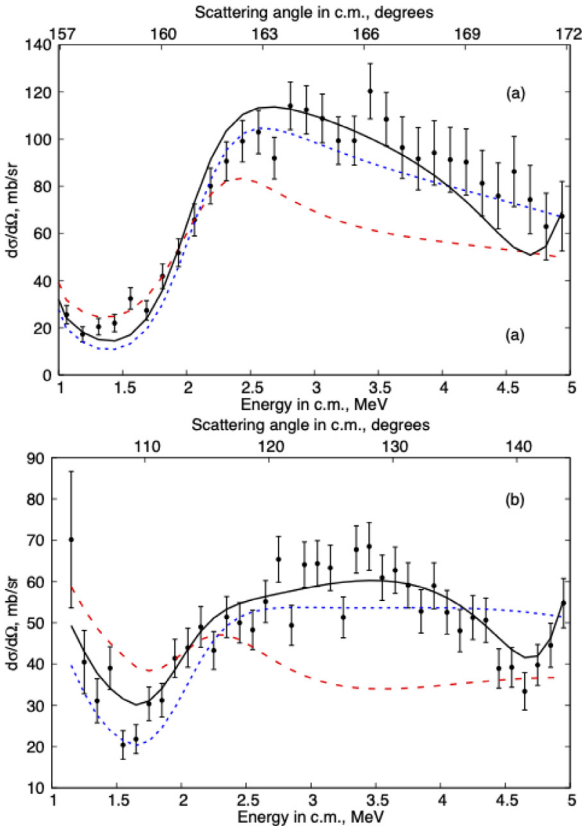

Fig. 7. Excitation function of the elastic scattering of ^{8}B on proton, between the angular ranges of 157–172° (a) and 100-145° (b). The curves represent various R-matrix calculations that incorporate a number of resonances in order to reproduce the experimental data.
Source: Taken from [49].

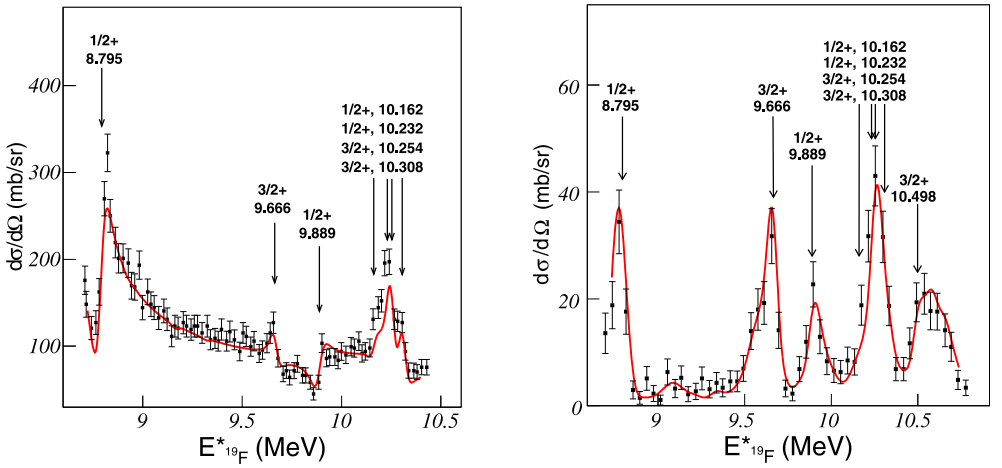

Fig. 8. Excitation functions of the proton scattering on ^{18}O measured in inverse kinematics using the ACTAR detector. Both the (p,p) and (p, α) channels could be measured simultaneously at a scattering angle $\theta_{cm} = (160 \pm 5)^\circ$.
Source: Taken from [7].

resonant scattering) have been used extensively for exploring the single-particle nature of nuclear states. Although they were recently mostly confined to stable or near-stable isotopes, the advent of active targets has opened the door to applying these methods to rare isotopes far from stability, where shell effects are expected to evolve under the influence of the nuclear force. They are therefore crucial to our understanding of the latter and its characteristics.

4. Pairing

As discussed earlier, by combining both the target and detector in one device, active targets provide large efficiency and excellent resolving power to maximize the physics reach of exotic beam facilities.

In this section we discuss the unique opportunities offered by active target time projection chambers to study pairing correlations in exotic nuclei, which is a topic that has received much attention in recent years. Following a short introduction, we will discuss specific examples regarding weakly bound systems, neutron–proton pairing, and shape coexistence.

4.1. Brief introduction

The nuclear pairing mechanism has been, for many years, a central topic in low-energy nuclear physics. Although the energy gain of the nuclear system due to pairing is relatively modest, pairing correlations have a strong influence on many properties of the nucleus including rotational moments of inertia, deformations, excitation spectra, and a variety of other phenomena [50–53]. An early approach to describing pair correlations in nuclei was the derivation of a collective Hamiltonian by Bès and co-workers, in formal analogy to the Bohr collective Hamiltonian, describing the quadrupole degree of freedom for the nuclear shape [54].

The analogy between particle–hole (shape) and particle–particle (pairing) excitations became well established and thoroughly explored in Ref. [55]. The key concept in the treatment of pair correlations as a collective mode is the pairing field [56], an average potential acting on the nucleons due to the effects of pair correlations. The form of this potential is

$$U_{pair} = \Delta \sum_j a_j^\dagger a_{\bar{j}}^\dagger \tag{3}$$

which creates two nucleons in time-reversed orbits, and is analogous to the deformed potential associated with distortions of the nuclear shape, proportional to $a_j^\dagger a_{\bar{j}}$. Considering a constant force, the pairing gap parameter is

$$\Delta = G \sum_j a_j a_{\bar{j}} \tag{4}$$

and represents the average value of the pairing density, from which a deformation parameter of the field can be introduced, $\beta_{pair} \approx \Delta/G$. In a single-j approximation $\Delta \propto G(2j+1)/2)$, that is proportional to the degeneracy of the level. Thus, in general, β_{pair} gives a measure of the effective number of levels, Ω, available for scattering of the pairs.

In the same way as a deformed potential violates angular momentum (I) conservation, the pairing potential in Eq. (3) violates particle number (N), thus there is a clear correspondence between N and I. In analogy to the 5-dimensional

oscillator of the Bohr collective Hamiltonian, this is a two-dimensional oscillator in what is usually referred as "gauge" space with the correspondences $\beta_{pair} \leftrightarrow (\beta, \gamma)$ and a "gauge" angle $\leftrightarrow$ the Euler angles [52,55].

On general grounds, we expect that nuclei with two identical particles added or removed from a closed-shell configuration should be close to a normal fluid, since the pairing correlations are not strong enough to overcome the large single-particle energy required to add a pair. In this limit, there is no static deformation of the pair field which fluctuates about $\beta_{pair} = 0$, and gives rise to a vibrational spectrum (Pairing Vibration). The ground state energies, referenced to that of the doubly-magic core, will follow a linear dependence as a function of the number of pairs added, i.e. $\Delta E_{gs}(N) \propto (N - N_0)$. The pair addition and removal spectrum near ^{208}Pb is perhaps the best example of this type of behavior [56].

Nuclei with many pair quanta outside of a closed-shell configuration correspond to a superfluid limit, where there is a static deformation of the pair field and rotational behavior results, i.e. $\Delta E_{gs}(N) \propto (N - N_0)^2$. A beautiful example would be the pair-rotational sequence comprising the ground states of the even–even Sn isotopes around ^{116}Sn [52]. In Ref. [57], simple analytical approximations to the pairing collective Hamiltonian were used to describe the transition from normal to superfluid behavior. Taking the analogy even further, a measure of the collectivity in the pairing channel, the 2-nucleon transfer operator plays a similar role to the $B(E\lambda)$ for surface modes. This is expected to enhance the observed cross sections as the different amplitudes for the two-particle transfer operator have the same sign and add coherently [58].

Consider the low-lying 0^+ states near a doubly magic nucleus. Given a set of single particle orbits $|n\ell j\rangle \equiv |j\rangle$, the wave function of the pairing vibration (PV) state can be written:

$$|PV\rangle = \sum_j \alpha_j |j^2\rangle;$$

The matrix element for the transfer of a pair of L=0 neutrons to the PV state in nucleus $|A_0 + 2\rangle$ from the ground state of $|A_0\rangle$ is

$$\langle PV|T|A_0\rangle = \sum_j \alpha_j \langle j^2|T|0\rangle;$$

and the cross section

$$\sigma(PV) \propto \langle PV|T|A_0\rangle^2 = (\sum_j \alpha_j)^2 \sigma_{sp};$$

making the further assumption that the single particle matrix elements are all approximately equal, $\langle j^2|T|0\rangle^2 \approx \sigma_{sp}$. The limiting case of Ω degenerate levels provides an estimate of the maximum collective enhancement (EF). Here we have $\alpha_j \approx \frac{1}{\sqrt{\Omega}}$ and thus

$$EF = \frac{\sigma(PV)}{\sigma_{sp}} \sim \Omega \tag{5}$$

which in the harmonic oscillator should scale with mass number as $\sim A^{2/3}$ [56].

In the superfluid limit, where a BCS condensate is a realistic approximation, the cross-section is should be proportional to β^2_{pair} and thus

$$EF = \frac{\sigma(BCS)}{\sigma_{sp}} \sim (\Delta/G)^2 \approx \Omega^2 \tag{6}$$

EF can be interpreted as a kind of "Weisskopf units" for two-nucleon transfer probabilities.

Based on the qualitative arguments above, the evolution of pairing correlations (as measured by 2n-transfer cross-sections) with the addition of pairs from a closed shell nucleus is expected to follow the schematic behavior shown in Fig. 9. Experimentally, low-lying pair-vibrational structures have been observed and characterized around ^{208}Pb by using conventional pair-transfer reactions such as (p,t) and (t,p) and similar studies in the Sn isotopes provided clear evidence as to their superfluid nature [53,55].

4.2. Weakly bound systems

The effect of weak binding on nuclear structure, decay, and reactions is an open question in nuclear physics. On the neutron-rich side of stability, as the neutron separation energy approaches zero, weakly bound neutrons in the single-particle levels at the Fermi surface approach the edge of the nuclear potential and may move outside the core of well-bound nucleons, and possibly couple to unbound continuum states. The nature of this transition from a closed to an open quantum system [59], where binding is dominated by correlations rather than the mean field, is just beginning to be explored. Perhaps the most famous example to date is ^{11}Li. This nucleus consists of a ^{9}Li core surrounded by two weakly bound neutrons (S_{2n}=294 keV) forming a dilute halo with 20–30 times the volume of the core [60,61]. Despite intense study of its structure and decay, a detailed understanding of the binding of ^{11}Li remains inconclusive.

The ground state of ^{11}Li is known to be roughly equal admixtures of halo neutrons in the $s^2_{1/2}(0^+)$ and $p^2_{1/2}(0^+)$ configurations [62]. In general, the pairing force is associated with the short-range (high-multipole order) parts of the

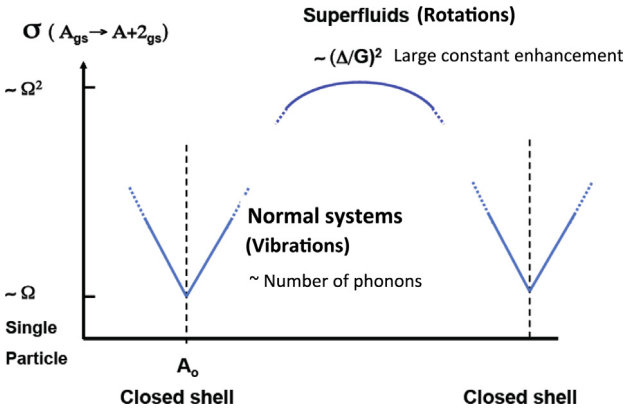

Fig. 9. Schematic illustration of the evolution of pairing correlations with particle number, as measured by two-nucleon transfer reactions. Near a doubly-closed shell a pairing phonon develops and the transfer strength is expected to increase linearly with the number of phonons. At mid-shell the correlations are maximized and give rise to a pairing gap and in turn a large enhancement of the cross-section.

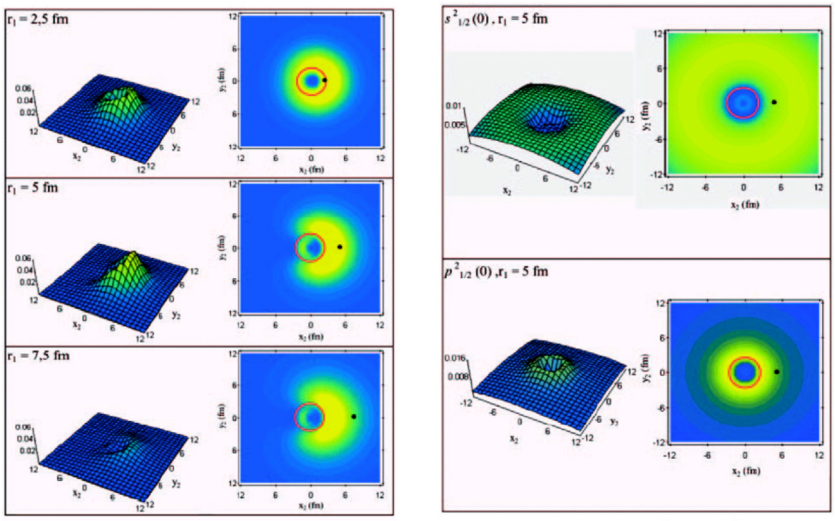

Fig. 10. Spatial structure of the two-neutron Cooper pair in ^{11}Li. The distribution of the second halo neutron is shown for a given position of the first neutron (black dot): On the left, when the effects of phonon-exchange are included and on the right, the distributions for pure configurations. The ^{9}Li core is shown as the red circle.
Source: Adapted from [63].

nucleon–nucleon interaction. Here, however, these will not be effective due to the low-angular momentum of the single-particle states involved (s and p waves). This has led to the proposal [63] that the halo neutrons of ^{11}Li are, in fact, bound only because of the extra pairing interaction mediated by the exchange of low-frequency surface vibrational modes. The spatial correlations generated in the two-neutron wavefunction by this phonon exchange are clearly illustrated in Fig. 10. Note how the second neutron in the halo is strongly correlated to the first when dynamical pairing effects arising from the phonon exchange are present, as compared to the case of pure configurations shown in the right panel. This mechanism is strictly analogous to the lattice phonon exchange responsible for the binding of electron Cooper pairs in a superconductor, and suggests the interpretation of the ^{11}Li halo as an isolated Cooper pair.

The reaction ^{11}Li(p,t) was studied in inverse kinematics at TRIUMF [64] using the active-target detector MAYA [6] at 4 MeV/A. Kinematic correlations and the Q-value spectrum shown in Fig. 11 demonstrate the power of an active target for these type of reactions with low beam intensities. From the analysis of experimental angular distributions in terms of a unified nuclear-structure and direct-reaction theory it is possible to show that the experiment provides direct evidence of phonon-mediated pairing [65].

Following from the discussion above, it is of particular interest to understand the density dependence of nucleon pairing in heavier neutron-rich isotopes. In Fig. 12 we show the results from nuclear matter calculations using both a bare nucleon–nucleon force G3RS and the Gogny D1 effective interaction for the interaction acting in the ^{1}S$_0$ channel [66]. The figure shows the average separation distance, d and the pair coherence length, $\xi_{rms} \sim \hbar^2 k_F/\pi m\Delta$, as a function of

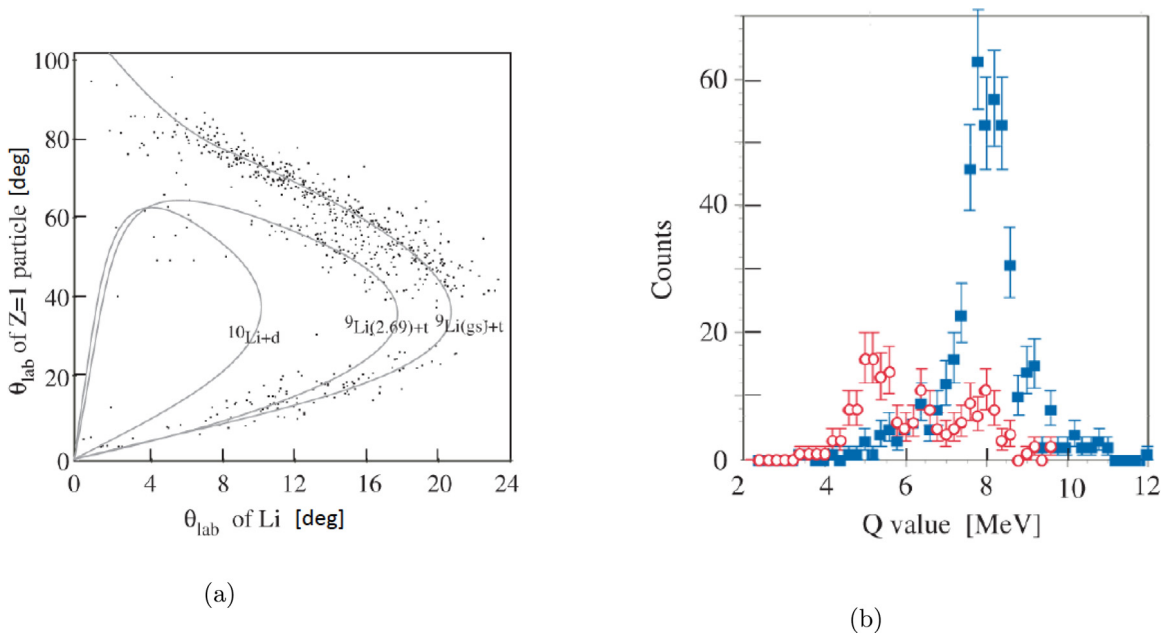

Fig. 11. (a) Kinematic angular correlations for the ^{11}Li(p,t) reaction studied at TRIUMF with the MAYA active-target detector. (b) Q-value spectrum for the ground state (blue) and first excited state in ^{9}Li.
Source: Adapted from Ref. [64].

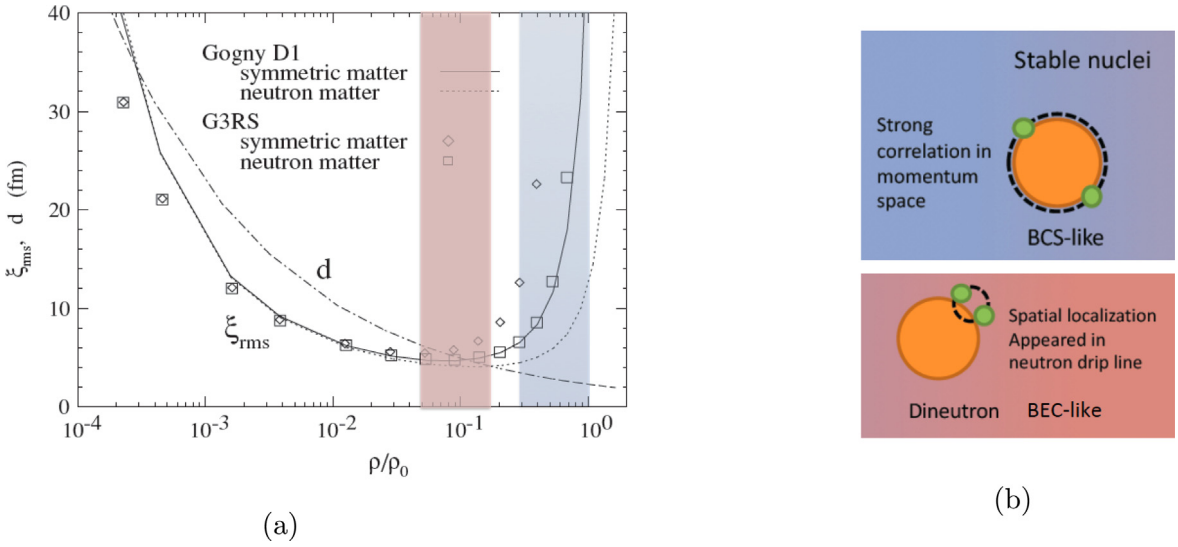

Fig. 12. (a) Nuclear matter calculations of the distance and coherence length of a nn pair as a function of the density. (b) The behavior observed in (a) suggests, as a general feature, a potential crossover between BCS and BEC phases in the surface of loosely bound nuclei.

the density, ρ. Independently of the interaction used, at densities $\rho/\rho_0 \sim 0.1$, we have $d > \xi_{rms}$ signaling the formation of di-neutrons. One could then anticipate a transition from normal Cooper pair condensation at normal densities to a Bose–Einstein-like di-neutron condensate (BEC) when the density is lowered to values characteristic in the region of the nuclear surface in neutron-rich systems.

While the nuclear matter results may not be fully applicable to finite nuclei, realistic calculations in the Sn isotopes based on Skyrme-Hartree–Fock mean field and continuum RPA predict a significant increase in the neutron pair-transfer strength to low-lying excited 0^+ states (pairing vibrations) for $N = 82-90$ nuclei [67]. For very neutron-rich Sn nuclei with $A > 140$ a large increase in the pairing gap is expected, which results in and increased ground state to ground state pair-transfer strength [67]. This behavior is attributed to the weakly bound $3p_{1/2}$ and $3p_{3/2}$ orbitals, which extend far beyond the nuclear surface. Currently it is not possible to study Sn nuclei with $A > 140$, where the abrupt changes in the pairing

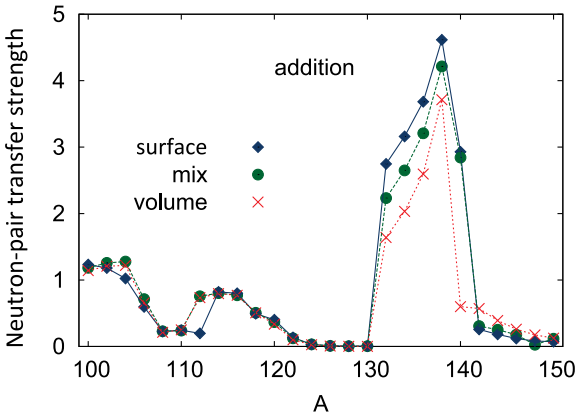

Fig. 13. Calculated pair-addition strength for the pair vibrational mode (excited 0_2^+ states) as a function of mass number A for the Sn isotopes. The lines indicate different pairing interactions used in the calculations.
Source: Figure adapted from [67].

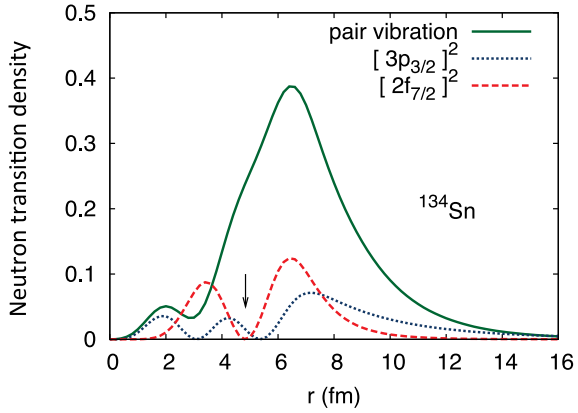

Fig. 14. Neutron transition density in ^{134}Sn, for neutron two-quasi-particle excitations to the $2f_{7/2}$ and $3p_{3/2}$ states, compared to the transition density for the pair-vibrational mode. The arrow indicates the rms radius of the total nucleon density for ^{134}Sn (4.84 fm).
Source: Figure adapted from [67].

transfer strength from excited states to the ground state occur. However, the region where pairing vibrations dominate, characterized by strong transitions to excited 0^+ states in pair-transfer, comes within reach of present accelerator facilities. As shown in Fig. 13 the calculated pair-addition strength for the pair vibrational mode differs significantly between nuclei with $N > 82$ and below.

The first excited 0_2^+ state can be regarded as a pairing vibrational mode built on the weakly bound $p_{3/2}$ and $p_{1/2}$ orbits, which shows a rather long tail in the transition density extending beyond the nuclear surface (see Fig. 14), resulting in a large strength, comparable to that populating the ground state.

As shown in Fig. 13 the large increase in the pair-transfer probability for $N > 82$ is almost independent of the form of the pairing parametrization used in the mean field calculations.

These predictions and the arguments presented in the introduction suggest that an experimental program to study (p,t) and (t,p) reactions on neutron rich nuclei has clearly the potential to obtain an experimental signal of this intriguing prediction. Absolute and relative measurements of the ℓ=0 pair transfer strength to the ground and excited 0^+ states along the Sn isotopic chain will provide insights into the nature of pairing and superfluidity, by systematically probing any change in the pair transfer strength to the pairing rotational ground states vs. the pairing vibrational excited 0_2^+ states across the $N = 82$ magic number.

Recent theoretical advances in combining detailed structure information with reaction theory [68] resulted in the calculation of absolute values of two-particle transfer cross sections along the Sn-isotopic chain which agree with measurements within errors and to some extent without free parameters (except for the Optical Model potentials). The success of this model, concerning the predictions of the absolute value of the two-particle transfer cross sections associated with the excitation of the pairing vibrational spectrum, appears as a promising (quantitative) tool to use in conjunction with experiments to study pairing phenomena in neutron rich nuclei.

4.3. Neutron–proton pairing

The dominant pairing in almost all known nuclei with $N > Z$ is that in which superconducting pairs of neutrons (nn) and protons (pp) couple to a state with angular momentum zero and isospin $T = 1$, known as isovector or spin–singlet pairing. However, for nuclei with $N \approx Z$, neutrons and protons occupy the same single-particle orbits at their respective Fermi surfaces and Cooper pairs, consisting of a neutron and a proton (np), may form. These types of pairs may couple in either isovector or isoscalar (spin–triplet with $J = 1$ and $T = 0$) modes, the latter being allowed by the Pauli principle. Contrary to the case of nuclei with large isospin imbalance, in nuclei with $N \approx Z$ the isoscalar mode is expected to dominate. Since the nuclear force is charge independent, one would also expect that pairing should manifest equivalently for np pairs with $T = 1$ and $S = 0$, akin to nn and pp pairs. In spite of the fact that there are convincing arguments for the existence of isovector np pairs, the existence of a correlated isoscalar np pair in condensate form, and the magnitude of such collective pairing remains a controversial and fascinating topic in nuclear structure physics [69].

Long-standing theoretical predictions of the onset of isoscalar pairing strength, the interplay between both pairing modes, and the presence of a condensate composed of both isoscalar and isovector pairs have remained without experimental confirmation [69,70]. This is mainly because the region of the nuclear landscape near the proton drip line where such phenomena are expected to appear is largely unreachable, and because the experimental observables are either inconclusive and/or complicated to interpret.

The rapid quenching of np pairs as one moves away from N=Z [71] suggests that the transfer of a np pair from even–even to odd–odd self-conjugate nuclei is a uniquely powerful tool to study np correlations [72,73]. The (p, ^{3}He) and (^{3}He,p) reactions appear as the best choice since the np pair can be transferred in both isospin states. Beyond ^{40}Ca, these studies require radioactive beams and the use of inverse kinematics techniques. The feasibility of the (^{3}He,p) reaction in inverse kinematics has been shown in a series of experiments at the ATLAS facility [74] using a gas cell target and a simple S1-type Si detectors setup. The reaction (p, ^{3}He) with radioactive beams of ^{56}Ni and ^{52}Fe were also successfully studied at GANIL [75].

In these experiments one measures cross-sections for np transfers from an even–even projectile to the lowest $J^\pi = 0^+, 1^+$ states in the odd–odd neighbor. While absolute cross-sections will be of interest, we note that the ratio $\sigma(0^+)/\sigma(1^+)$ itself is sensitive to the pairing collectivity in the respective channels, thus reducing systematic effects of absolute normalization.

Active targets, combining both target and detection systems in a single device, will be the perfect instrument to carry out this exciting program. As an example we consider the reaction ^{3}He(^{56}Ni, ^{58}Cu)p at 6 MeV/u. The Q-value for these reactions is typically +5 MeV. The range of ^{56}Ni in ^{3}He at 300 torr is about 150 cm. As a conservative estimate we consider an effective target thickness given by the first 2 mg/cm^2 corresponding to beam energies from 6 MeV/u to 4 MeV/u, a regime where the shape of the angular distribution remains sensitive to the transferred ℓ. The proton energy vs. lab angle is shown in Fig. 15 for the ground-state, and an excited state at 1 MeV. The estimated energy and angle resolutions are 1% and 1 deg respectively, They are shown as error bars on the graph and will be sufficient to resolve contributions from other near low-lying states in the odd–odd nucleus for most of the cases. With typical cross sections of 1 mb/sr in the forward center of mass angular region (backward lab angles) where the $\ell = 0$ pair transfer dominates, it is estimated that for a 10^3 pps beam ^{56}Ni running for 5 days, one would obtain approximately 150 counts in the peaks of interest.

The reaccelerated N=Z beams that will become available with new facilities worldwide, such as the ReA6/12 upgrade at FRIB [76], offer a unique opportunity to study the (^{3}He,p) reaction using beams from ^{40}Ca to ^{88}Ru and make a strong impact in answering this interesting facet of pairing in nuclei. This is clearly illustrated in Fig. 16, where the expected yields are shown as a function of the mass of the beam. Based on the realistic estimates above, a successful measurement will require intensities of 10^3 pps, thus reaching nuclei (superfluid systems) in between the closed shells of ^{56}Ni and ^{100}Sn (normal systems). This is the region where pairing collective effects are expected to fully develop.

4.4. Island of Inversions

Understanding the so-called "Islands of Inversion" has been the subject of intense work, both experimentally and theoretically [24] (see also Section 3). This phenomenon has been found in several regions of the nuclear chart, notably in neutron rich nuclei with $N = 8$, 20, and 40. The microscopic origin of this effect follows from the removal of protons from the corresponding spherical doubly-magic nuclei, $^{16}O_8$, $^{40}Ca_{20}$, and $^{68}Ni_{40}$, inducing changes in the effective single-particle energies (ESPE). Due largely to the monopole average of the central and spin–isospin components of the nuclear force [25], ESPE's for a given isotonic chain change as protons are removed from the systems. The delicate balance between the monopole effects and the residual pairing plus quadrupole interactions leads to a competition between spherical and deformed configurations. At some point, the pairing and quadrupole correlations dominate over the single particle energy and erode the shell gaps. Furthermore, depending on the number of valence protons, the remaining valence between the pairing and quadrupole forces leads to deformed or superfluid ground states in nuclei, expected *a-priori* to be semi-magic and spherical.

Early studies of shape coexistence showed that (p,t) and (t,p) reactions also provided a sensitive tool to understand the nature of this transition and determine mixing amplitudes between deformed and spherical configurations [77,78].

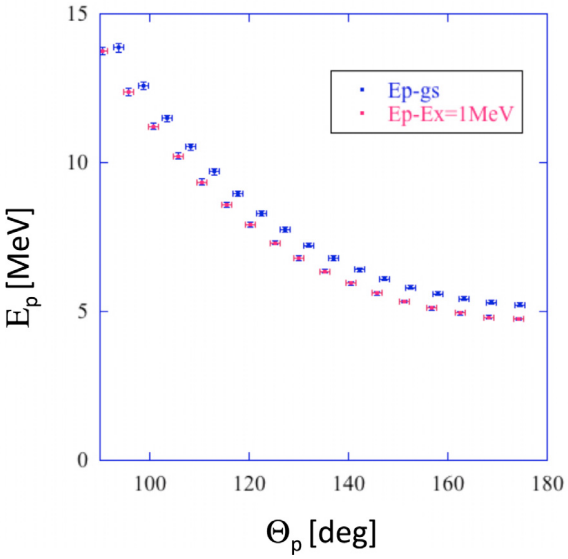

Fig. 15. AT-TPC Simulation of Kinematic correlations for the ^{56}Fe(^{3}He, ^{58}Cu)p reaction for the conditions discussed in the text.

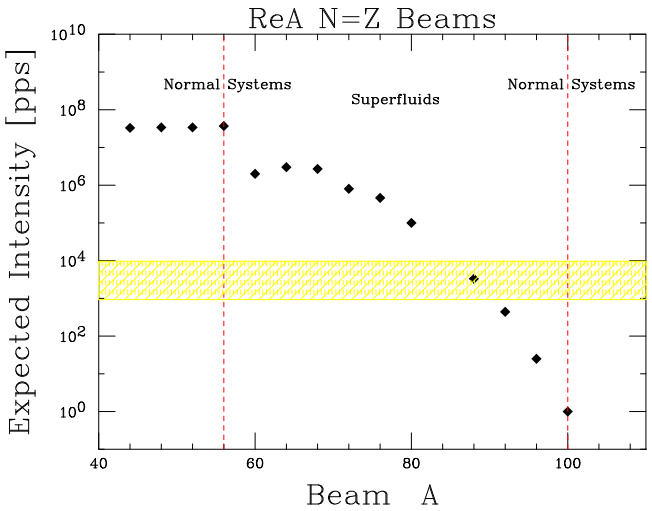

Fig. 16. Estimated Yields for re-accelerated N=Z beams for the ReA Energy Upgrade [76]. Using an active target TPC will require beam intensities of $\gtrsim 10^3$ pps (yellow shaded area), and a systematic study up to ^{88}Ru will be possible.

Perhaps the best known example is that of the $N = 20$ Island of Inversion, centered around ^{32}Mg. Deformed intruder configurations, with neutron pairs promoted from the *sd* to the *fp* shell across the narrowed $N = 20$ gap, are energetically favored [79–82], leading to well-developed deformation in the ground states of the affected nuclei. Particles promoted to the *fp* shell and holes created in the *sd* shell take full advantage of the quadrupole–quadrupole force and the gain in correlation energy overcomes the cost of crossing the shell gap. The available evidence points, indeed, to a picture consistent with deformed ground states. The two-neutron transfer reaction ^{30}Mg(t, p)^{32}Mg was studied at ISOLDE in Ref. [83]. A shape-coexistence two-level model analysis [84,85] of the data leads to the puzzling conclusion that in ^{32}Mg the 0^+_1 ground state is dominated by the *sd*-shell components (≈80%) and the excited 0^+_2 by the *fp*-shell 2*p*2*h* intruder configuration, contrary to the accepted interpretation. Further analysis of the transfer reaction data, extending it to a three-level mixing [86] of coexisting 0*p*0*h*, 2*p*2*h* and 4*p*4*h* states resolved the "puzzle", confirming the sensitivity of this reaction to the wavefunction.

We consider this case as an example of the performance of an active target for this type of studies. While the (t,p) reaction can be studied by using tritium loaded targets as done in Ref. [83], here we consider using tritium gas. A conceptual design for an inner cell containing the gas and minimizes the amount of tritium (and thus safety requirements)

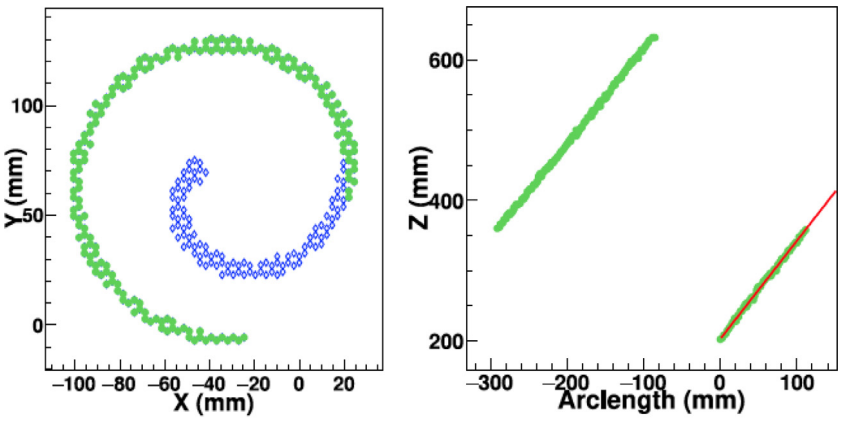

(a)

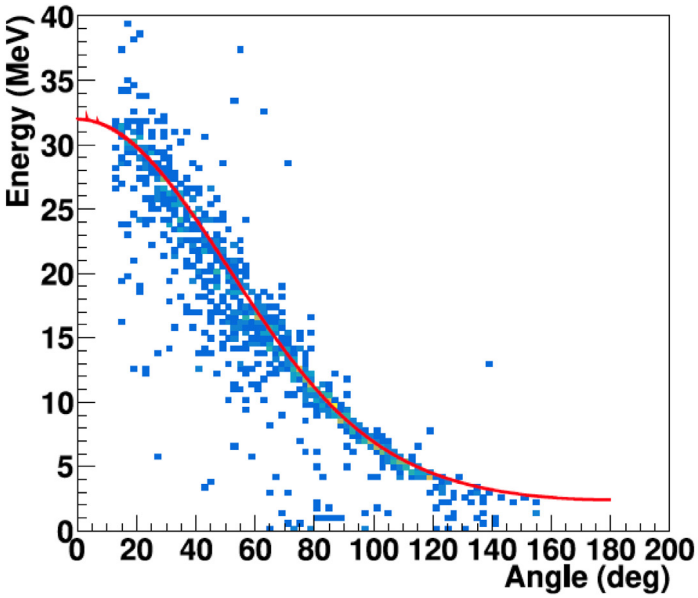

(b)

Fig. 17. (a) Left panel: Simulated proton track projected into the TPC pad plane. Open blue diamonds and solid green dots refer to the full hit pattern and the part of the hit pattern used to calculate the radius of curvature, respectively. Right panel: Arc length of each hit pattern point as a function of the z coordinate. The red line is the least-squares fit performed to extract the scattering angle from the slope. (b) Proton energy vs. lab angle for the ^{30}Mg(t, p)^{32}Mg reaction at 5 MeV/u reconstructed from the radius of curvature and angle inferred from the Hough transform and RANSAC method. The red solid line represents the kinematics calculation.
Source: Adapted from Ref. [87].

has been put forward in Ref. [87]. In Fig. 17 we show our simulations assuming a Mylar cell of 5 μm thickness and 1 cm diameter with 200 torr of pure tritium. The equivalent target thickness is 3.2 mg/cm^2, $\approx$ 100 times thicker than currently available foils. The tracking medium consists of 40 torr of isobutane and the magnetic field was set to 2 T.

The simulated tracks are analyzed in the same way as the experimental data. Use of pattern recognition algorithms allows the extraction of features from the hit pattern to infer the initial track parameters. For this (simple) preliminary study we have used the circle Hough transform combined with the RANdom SAmple Consensus (RANSAC) method to determine the center and the radius of curvature of each track (see Ref. [87] for details). Once the radius of curvature is determined, the scattering angle can be inferred by parameterizing the position along the Z axis as a function of the

arc length as shown in the right panel of Fig. 17(a). From the radius of curvature and the scattering angle, one infers the energy of the proton, considering that the magnetic field is parallel to the beam direction.

The kinematics plot for the ^{30}Mg(t, p)^{32}Mg reaction at 5 MeV/u populating the ground state and reconstructed using the initial parameters estimated above is shown in Fig. 17(b). As illustrated, the agreement with the calculation is very good, particularly the angular resolution provided by the method is around 0.5 deg. On the other hand, the energy resolution that this method provides is around 2.0 MeV, not yet competitive with a Si-detector array as in the ISOLDE results. Nevertheless, it is anticipated that further processing of the data by using a Monte Carlo fit will provide a resolution of better than 100 keV and 0.32 deg for the energy and angle of the protons [4]. Furthermore, the large angle coverage and higher luminosity achieved with an active target will be mandatory to extend these measurements towards the neutron drip line, for example the case of the Mg isotopes up to ^{40}Mg [88].

As a final note we mention that, besides the technical development of the cell above, the tritium activity is $\sim$20 Ci posing a radioactivity hazard that requires a careful mitigation plan. Safety layers with double/triple enclosing volumes will likely be needed. However, in order to maximize the physics reach of the exotic beams available, we believe the development of a dedicated tritium cell to operate inside a time projection chamber should be considered seriously. It goes without saying that such a cell can also be used with other rare gases that, although not radioactive, are currently very expensive like ^{3}He.

4.5. Summary and outlook

Transfer reactions have provided a wealth of information that has shaped our current understanding of the structure of atomic nuclei. In particular, two-nucleon transfers have firmly established the ubiquitous role of nuclear pairing correlations. Unquestionably they will continue to provide a unique tool as we embark in our experimental study of very-neutron and -proton rich nuclei.

Existing and planned exotic beam facilities worldwide and new detector systems like active targets with unparalleled sensitivity and resolving power not only will allow us to answer some burning questions we have today, but most likely will open up a window to new and unexpected phenomena. In this section we addressed some specific examples focusing on two-nucleon transfer reactions with light ions. Obviously, given the flexibility of time projection chambers to operate with several gases, reactions like (^{18}O, ^{16}O) can be studied to provide additional information on pairing phenomena [89].

5. Clustering in nuclei

Nuclei have been known to exhibit cluster structure especially in the light mass region. There has been much progress in understanding the nature of clustering theoretically and this has spurred experimental work to find evidence to test theoretical predictions. Ultimately, a deep understanding of clustering from a fundamental and microscopic perspective is desired. A recent review of understanding nuclear clusters from a microscopic perspective can be found in Ref. [90] as well as various other aspects of clustering in Refs. [91–94]. Although experimental evidence for prominent cluster structure has been accumulating over the past five decades, there is still a lack of data especially for unstable nuclei both close and far from the valley of stability. Radioactive beams are required to access information on these unstable nuclei and active targets are well suited to study a variety of reactions that can be used to probe their cluster structure.

5.1. Physics of clusters

The formation of clusters is rooted in correlations between nucleons in the nuclear medium. There has been recent insights into some of these short-range correlations that have been found through high-energy electron scattering [95]. In this study, proton–neutron short-range correlations related to the EMC effect were found to dominate in the nuclear medium [96]. Both short-range correlations and the EMC effect have a sensitivity to the clustered nature of ^{9}Be when scaled to nucleon number or average density [97,98]. On the theoretical side, a number of microscopic approaches have shown cluster structure to be a prominent and robust feature, especially in light nuclei. These approaches include the no-core shell model [99], Green's function Monte Carlo [100], lattice effective field theory [101], symplectic shell model [102], antisymmetrized molecular dynamics (AMD) and fermionic molecular dynamics [103,104]. For ground-state properties, relativistic mean-field theories have also shown prominent clustering in light nuclei. The important aspect to note is that these microscopic approaches do not assume any cluster structure *a priori* but clusterization as seen in the resulting density distribution of particles emerges naturally from the model. For example, a deformed AMD calculation shows the density distribution of protons and the most weakly-bound neutron in ^{14}C (Fig. 18) and the emergence of clusters can be seen [105]. These calculations show that cluster structure is a fundamental and important part of structure that comes from the underlying nucleon–nucleon interactions.

One of the smallest and most prominent clusters is the α cluster consisting of two protons and two neutrons that are highly correlated. The α particle is known as one of the most stable nuclei. It has a very large binding energy per nucleon, and a total spin and isospin of zero, making it a symmetric system in spin and isospin. Evidence for α-cluster structure is found in light nuclei starting with neutron-rich He isotopes and continues in nuclei as heavy as ^{44}Ti [106]. It is especially prominent in nuclei that can be divided into an integer number of α clusters that are called α-conjugate nuclei. Beyond

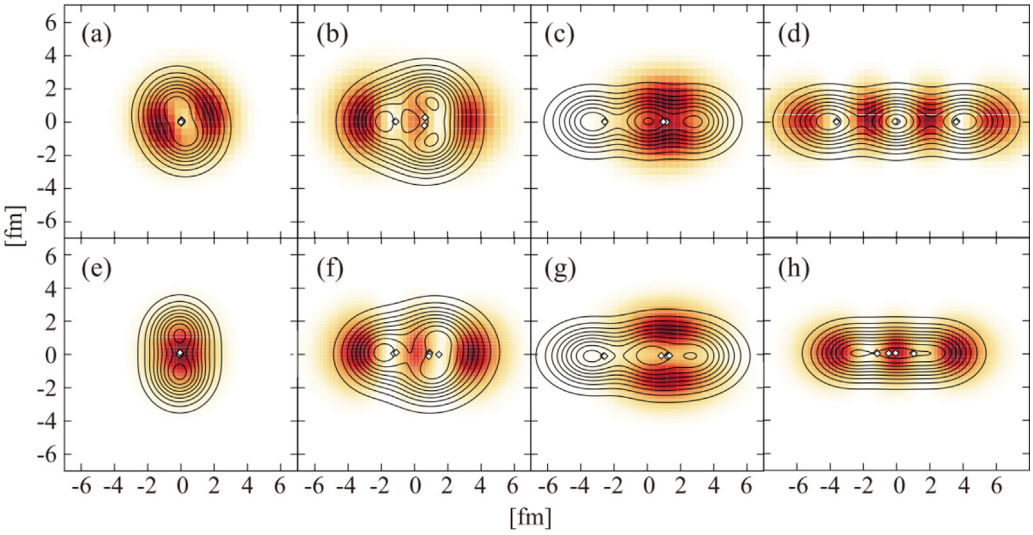

Fig. 18. Density distribution of nucleons in ^{14}C in the intrinsic frame of reference for different positive-parity (top row) and negative-parity (bottom row) states. The contour lines show the proton density distribution and the color density shows the density distribution for the most weakly-bound neutron.
Source: Figure from Ref. [105].

these α-conjugate nuclei, certain α non-conjugate nuclei, ones that can be divided into an integer number of α particles plus additional protons, neutrons, or other light clusters, also contain prominent cluster states. These α non-conjugate nuclei are sometimes referred to as nuclear molecules. Searches for α-cluster states are typically carried out near the α threshold, as they have been experimentally found to appear near this region. This is the basis of the Ikeda diagram, which gives an approximation of where various clusters in the light-mass region may appear based on their separation energies (see Fig. 19) [107].

More experimental data is needed to elucidate where cluster structures exist in nuclei, especially in unstable nuclei where there is a lack of data due to the need for high-quality radioactive beams.

5.2. Reactions and observables

Reactions that involve α particles in the entrance and/or exit channels may be particularly sensitive to α-cluster structure. Reactions that have large α widths would be consistent with an interpretation that a certain nuclear level or resonance (see Section 2) has a prominent α-cluster structure. For this reason, there have been a number of experiments that have searched for α-cluster structure using resonant α scattering. In (α, α) and (α, α') reactions, large α widths would result in prominent resonances with large cross sections. The properties of these resonances, such as their width and energy, can then be interpreted or compared to theoretical predictions [90–92].

The measurement of resonances through other α-induced reactions such as (α, p), (α, n), and (α, γ) also yield insight into the nature of the resonances. Many of these type of reactions also play a central role in the synthesis of elements and the energy generation of stars and explosive astrophysical phenomena [108] (see also Section 8). As many of these also involve radioactive nuclei with reactions at low energy, active targets are well suited for those cross section measurements.

5.3. Examples of cluster structure from theory and experiment

There have been a number of experiments aimed at finding and studying clustering in nuclei using active targets and in this section, we highlight a few examples, note the utility of the active target method, and suggest future possibilities for future experiments.

5.3.1. Nuclear molecules

It has been known that α-cluster structure is prominent in the Be isotopes [109]. A prime example is the decay of the ground state of ^{8}Be. This unique decay into two α particles gave a strong clue for the clustered nature of ^{8}Be's ground state. A number of cluster models have also predicted strong cluster states in the isotope ^{10}Be. One of these models is the Anti-Symmetrized Molecular Dynamics (AMD) where each nucleon in a nucleus is represented by a Gaussian wave packet [103]. These wave packets interact with a given nuclear interaction and the wave functions are found using the variational principle. By looking at the resulting density distributions, one can study the formation and dissolution of

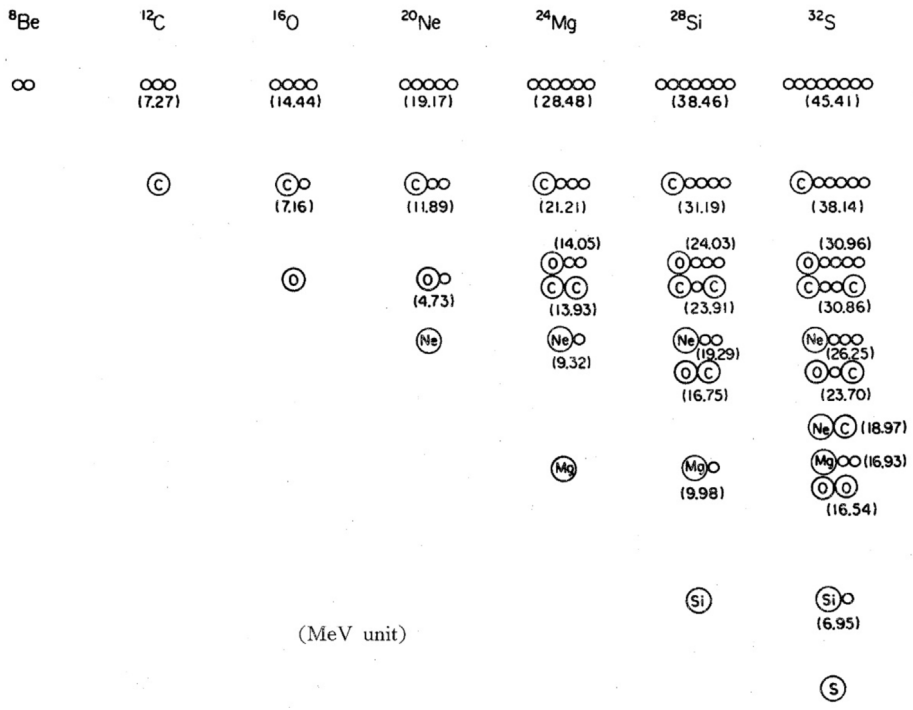

Fig. 19. The Ikeda diagram shows various cluster configurations based on the cluster separation energies. *Source:* Figure from Ref. [107].

cluster states as the AMD model does not assume any cluster structure in the model *a priori*. The predictions of the AMD model show a strong two α-cluster structure with the two "valence" neutrons configured in what are called the π and σ orbits, drawing the labels from an analogy with atomic molecules. The prominent α clusters should result in large α widths while the differing arrangements of the valence neutrons should result in differing resonance energies. In addition, the rotation of such structures should result in rotational bands that have differing moments of inertia that can be inferred from their $J(J+1)$ energy spacing.

An experiment was performed to look for strong α-cluster states in ^{10}Be using a radioactive beam of ^{6}He and a ^{4}He gas target filling the prototype Active Target Time Projection Chamber (pAT-TPC) [110]. In this experiment, the scattered particles were imaged by the pAT-TPC and the position of the reaction vertex was deduced, then converted into the energy at which the reaction occurred through the knowledge of the beam's initial energy and calculated stopping power in the 1 atm of He gas. In addition, both the ^{6}He and ^{4}He reaction products were stopped in the gas target, from which the energy of the reaction products were deduced. This allowed for the measurement of excitation functions and angular distributions over a wide angular range.

The ^{6}He beam intensity for this experiment was on the order of 1000 pps and ran over a period of approximately four days. The thick gas target allowed for a higher luminosity while the very high geometrical efficiency and angular resolution of the pAT-TPC allowed for detailed angular distributions that were able to constrain *R*-matrix calculations (see Section 2).

The experimental results were compared to AMD calculations. The 2^+ and 4^+ members of the rotational band for the σ configuration were observed, but only the 2^+ member of the π-configuration rotational band was seen. The fact that the 4^+ level of the π configuration was not observed was predicted by the AMD calculations from the interpretation that higher angular momentum limited the formation of clusters for the π configuration [110].

5.3.2. Searching for cluster structure in isobaric analog states

A similar study of the isospin mirror of ^{10}Be, ^{10}C, was performed using inelastic resonant α scattering using a radioactive beam of ^{10}C at 75 MeV/u and the MAIKo detector [9,111]. In this case, small scattering angles in the center-of-mass frame translate to scattering near 90° in the laboratory frame. As the scattering angle approaches 90°, the energy of the scattered α particles approaches zero and thus a very thin target is needed to allow for the α particle to be detected. An active-target detector gives a significantly lower threshold for detection compared to the use of a gas target with external particle detectors. For example, to detect 400 keV α particles, the lowest energy α particles detected in the experiment, one would need to use target chamber foils that are thinner than 1 μm in order to prevent all of the energy to be lost in the foils. The use of thin foils becomes challenging for holding a significant gas pressure such as 0.5–1.0 atm as was done in this experiment.

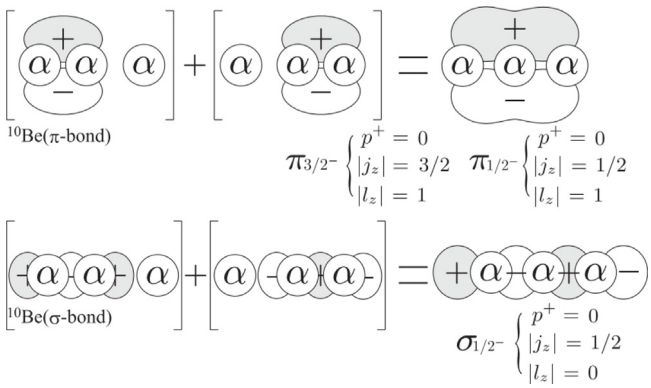

Fig. 20. Linear-chain states from AMD calculations.
Source: Figures from Ref. [105].

5.3.3. Exotic cluster structures: Linear-chain states

For heavier nuclei, it is possible to have structures that contain more than two clusters. The next structure naturally has three clusters and these three clusters can now form two distinct arrangements: a triangular configuration or a linear-chain configuration. These distinct configurations have been predicted by AMD models [105,112] for ^{14}C and more recently in ^{14}O [113]. What these models show is that it may be possible to have both configurations realized in nuclei. The linear chain state is particularly interesting as it would represent a very unique structure that has a very large degree of deformation. Finding evidence for such a structure in nuclei would be important for understanding the possible extent of deformations and more generally, what extent of shapes nuclei can exhibit [92,103]. This would have many implications for the current nuclear theoretical understanding [90].

A number of experiments were aimed at probing the resonances above the α threshold in ^{14}C to search for the linear α-chain states. These experiments used a radioactive beam of ^{10}Be and a ^{4}He gas target to measure cross sections for the ^{10}Be(α, α)^{10}Be and ^{10}Be(α, α')^{10}Be* reactions [114–116]. Two of the experiments used the thick target with inverse kinematics technique that has much overlap with the use of active-target time projection chambers [114,116]. These experiments used a gas target and an array of Si detectors to detect the outgoing reactants and infer the position of the reaction vertex in the extended gas target. A number of resonances were observed and candidates for resonances with relatively large α widths were identified. An experiment using an active-target time projection chamber, the pAT-TPC was also performed where the scattering reaction was captured as a track image. The reaction vertex location and outgoing particles were identified and cross sections were measured for a number of resonances. The advantages of the active target method are the increased luminosity for a given initial beam energy and the ability to directly measure the particle tracks of the scattering event. This tracking allows for a clear discrimination between elastically scattered and inelastically scattered particles, which is predicted to be an important signature of one type of linear-chain state.

Similar to the AMD predictions for ^{10}Be, the linear-chain cluster structures predicted for ^{14}C also are of two types, a π configuration and a σ configuration. A schematic representation of these configurations is shown in Fig. 20. The π configurations are asymmetric in shape and are predicted at lower excitation energies while the σ configurations are symmetric in shape and are predicted to appear at higher excitation energies. The energies and partial α widths for these predicted states can be measured and compared to the theoretical predictions. The results from the three different resonant α scattering experiments agree for some resonances and disagree for others. The assigned spin and parity for resonances as well as the deduced α widths and the cross section contribution for the inelastic channel also differ, complicating the precise interpretation of the resonances as well as the direct comparison to theory. Active targets can provide higher statistics experiments and high angular resolution data, and are therefore well placed to contribute to investigating and resolving these differences in future experiments. The large solid angle coverage and track imaging will allow for detailed angular distribution measurements as well as precise identification of inelastic contributions.

AMD predictions for similar linear-chain cluster structures have been made for the isospin mirror nucleus ^{14}O [113]. If cluster structure is preserved for isobaric analog states in α non-conjugate nuclei, a similar structure in resonances should be observed in resonant α scattering measurements. The energies of these resonances have been predicted where, due to the extra protons that accompany the α clusters, Coulomb shifts can play an appreciable role. These Coulomb shifts can be a signature for these predicted linear-chain structures.

In addition to elastic and inelastic resonant α scattering, one can look at the tendency for a clustered nucleus to break up into its constituent clusters. The probability for multi-particle decay modes is an important observable that can also give insight into the underlying cluster structure of states in a nucleus. The three-body decay of a resonance in ^{14}C would result in three α particles and two neutrons. In an active-target detector, only the charged α particles would be detected but the resulting image would be a unique signature of the three α decay. An advantage of this tracking is

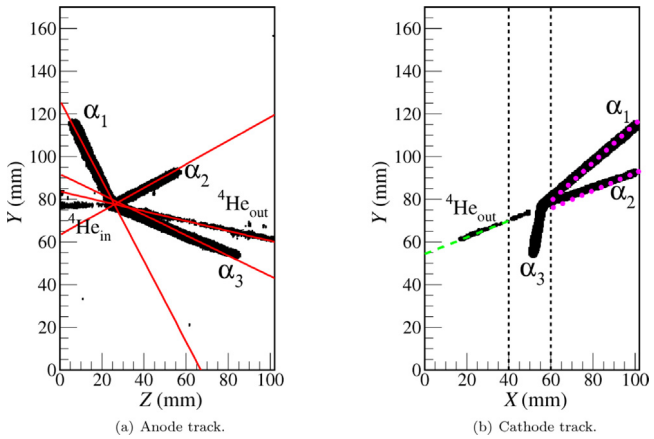

(a) Anode track. (b) Cathode track.

Fig. 21. The three-body breakup of ^{12}C after scattering with an α particle is shown. The measured track projections on the *YZ* and *XY* plane are shown in the left and right plot, respectively. The thin solid and dotted lines show the lines for the reconstructed tracks.
Source: Figure from Ref. [9].

the nearly 100% detection efficiency of these type of events given a proper trigger is used. This would allow for a precise determination of the probability of three-α decay events occurring for a given resonance. The observation of three-body decay of resonances in ^{14}C has been achieved with the pAT-TPC using a radioactive ^{10}Be beam. After analysis it was found that the three-body democratic decay increases compared to sequential decay for higher reaction energies [117]. For possible cluster structures in other $A = 14$ isobars such as ^{14}O, an even more interesting prospect occurs as the extra particles outside the α particles are protons and thus can be detected simultaneously with the three α particles. For ^{14}O, one would detect five simultaneous particles in a breakup event: three α particles and two protons. The angular distribution of these particles with respect to one another, for example the protons with respect to each other, can also give insight into the underlying structure of the resonance from which the breakup proceeded. The analysis techniques such as robust track identification and trigger generation for multi-track images is still being refined and developed, but the high efficiency and low detection thresholds of such multi-particle tracking is an advantage for active-target time projection chambers compared to Si detector arrays. An example of multi-particle tracking is the study of the three-body breakup of the Hoyle state in ^{12}C [9]. Fig. 21 shows an example of a multi-body breakup of ^{12}C after scattering with an α particle. The projection of the tracks onto the *YZ* and *XY* planes is shown as well as the lines for the reconstructed tracks. The incoming and outgoing ^{4}He track is clearly distinguished from the three breakup α particles via its smaller energy loss. Although using a high-efficiency Si may give better energy resolution, the high geometrical efficiency and angular resolution with low-energy thresholds are advantages of the active target method.

5.3.4. Clusters in heavier nuclei and their impact in astrophysics

With higher mass nuclei, there are additional integer numbers of α clusters, but also larger clusters such as ^{12}C. ^{12}C + α cluster structure has long been a topic of interest due to the possibility that low-energy resonance with such structures can dramatically enhance the ^{12}C(α, γ)^{16}O reaction, which is considered one of the most important reactions of nuclear astrophysics as it determines the carbon-to-oxygen ratio of the universe [118].

In the α-conjugate nucleus ^{20}Ne, one may expect five prominent α clusters to appear, but the situation seems to be more complicated as more nucleons start to enable many more degrees of freedom [119,120]. A relativistic mean-field theory calculation shows that clustering is prominent in the ground state of ^{20}Ne but the density distribution seems to correspond to four unequal clusters rather than five equal clusters that may be identified with α clusters [121]. Nevertheless, interest in cluster structure in ^{20}Ne and its neighboring isotopes remains high due to the lack of cluster information on heavier nuclei and the implications cluster structure has on astrophysical reaction rates, for the formation of the elements and their evolution in the universe [108].

Finding clear evidence for cluster structures in Ne isotopes has been an ongoing quest. Symplectic shell model calculations have predicted prominent cluster structures in the Ne isotopes [120]. Studies have been performed to measure resonances in α-induced reactions in ^{22}Ne and its isospin mirror ^{22}Mg, using a stable ^{18}O and a radioactive ^{18}Ne beam, respectively [122,123]. Strong α resonances were seen in ^{22}Ne but were absent in the ^{22}Mg measurement. The results of the ^{22}Mg experiment remain inconclusive as the possibility of strong α resonances exists, but is ruled out in the energy range measured. A detailed study of resonances in ^{22}Mg for a larger energy range would help in confirming whether or not the isobaric analogs to the strong resonances observed in ^{22}Ne exist in ^{22}Mg. The question of whether prominent clusters exist in proton-rich nuclei in this mass region therefore remains an open question.

Cluster states in this mass region can play an important role in nucleosynthesis. (More examples of using active targets for nuclear astrophysics experiments are found in Section 8.) More specifically, the ^{22}Ne(α, n)^{25}Mg reaction is important

for understanding the generation of the neutron source for the slow-neutron capture or *s*-process. For this reaction, low-energy α resonances can play a key role in enhancing the reaction rate for this process in giant stars in their late stage of evolution [124]. Although this reaction has not been studied with active targets, one may consider the advantages of using a gas target with a ^{4}He or ^{22}Ne beam to study the reaction directly. Towards heavier nuclei, the level density of the compound nucleus increases therefore the details of the required energy resolution will be important.

5.4. Summary and outlook

Clustering in nuclei continues to be an important part of understanding fundamental nuclear structure as well as having implications in nucleosynthesis. Active targets have allowed for a greater accessibility to search specifically for α-cluster states in α non-conjugate nuclei requiring the use of radioactive beams. The advantages of obtaining full kinematic information as well as greater luminosity make them well suited for current and future studies of searching for α-cluster states in the light mass region. Advances that push the limits for energy resolution and rate capabilities, as well as the ability to fully analyze multi-body decay channels are important for future experiments, and to obtain the highest quality data from active targets.

6. Decay processes

How a radioactive nuclei gets rid of the excess of neutrons or protons on its way towards stability depends very much on its location in the nuclear landscape. Usually, the β-decay process dominates how a nucleus is transformed into another. In the β^{-}-decay process, which usually happens in neutron-rich nuclei, a neutron is converted into a proton, with the emission of an electron and electron anti-neutrino. On the other side, proton-rich nuclei may undergo β^{+}-decay converting a proton into a neutron, and emitting a positron and an electron neutrino. Towards the drip lines, many other decay channels become open due to the decreasing separation energies, the increasing Q-values and isobaric mass differences, and the partial half-lives for particle emission. The β-decay process can populate unbound states in the daughter via different emission channels such as $\beta\gamma$, $\beta\alpha$, βp or βn (including multi-particle emission). Beyond the proton drip line, the separation energy becomes negative enabling one- and two-proton radioactivity from unbound nuclei due to the Coulomb barrier and pairing interaction. Whether the direct emission of protons can compete with β-decay depends very much on the partial half-life of that channel. The emission of two protons is particularly challenging to investigate because several scenarios are possible: sequential emission via a proton-unbound state in the daughter nucleus; or simultaneous emission of two protons ($\beta 2p$) or two-proton radioactivity from the ground state. In these multi-particle emission cases, the decay may proceed through resonances or a break-up process ruled by phase space. Fig. 22 shows the possible decay modes for β-delayed particle emission. Comprehensive and detailed reviews on these topics can be found in [125] (Nuclear structure at the proton drip line), [126] (β-delayed particle emission), [127] (Particle radioactivity of exotic nuclei), [128] (Two-proton radioactivity), and [129] (Radioactive decay at the limits of nuclear stability).

The close proximity of the proton drip line to the valley of stability has enabled a comprehensive exploration of the β-delayed and direct particle radioactivity phenomena [129]. β-delayed proton emission is open for nuclei close to the drip line, with most of the nuclei where this mode dominates having few precursors (the nucleus that undergoes decay). The intensity of the β-delayed emission is inferred from the branching ratio of the delayed emitter to the daughter, and the intensity of the β transition from the precursor to the emitter. The direct emission of protons can occur from isomeric states of nuclei not close to the drip line and from the ground-state when crossing the drip line. Since pairing plays a key role in proton radioactivity, the emitters are classified according to seniority s, which is equal to the number of unpaired protons and/or neutrons. This classification explains why protons can be emitted from isomeric states in nuclei far from the drip-line: emitters with $s > 2$ have an odd proton in addition to one or more broken pairs of nucleons, which corresponds to high excitation energy.

On the neutron-rich side the emission of charged particles proceeds differently. Delayed charged particle emission after β-decay is possible for loosely bound light nuclei. Several halo nuclei with open emission channels such as βp, βd and βt have been identified [130–132]. On the other hand, the direct emission of neutrons from neutron-rich nuclei is still an open and fascinating topic. Because neutrons are not sensitive to the Coulomb barrier, they are only bound by the centrifugal barrier. Therefore, the extremely short lifetime of the observed neutron emission sets the phenomena closer to resonances rather than delayed emission of neutrons. Although β-delayed neutron emission or spontaneous emission is of great interest to the community [126,133], the detection of neutrons is out of the scope of this publication.

This section of the review covers a detailed compilation of charged-particle radioactivity studies that have been performed with time projection chambers (TPC). Independently of the production method of the radioactive nuclei, TPCs were introduced to fulfill several deficiencies of the conventional setups used for these studies. They provide an extremely high detection efficiency by covering the full angular distribution of the process. In addition, the particle detection threshold is dramatically lowered, enabling the study of decay channels where the emitted particle has very low kinetic energy. In the case of multi-particle emission, TPCs provide a unique capability: the reconstruction of the tracks of the particles to enable the study of correlations with high precision. This section will cover four different topics: basic concepts on particle radioactivity, β-delayed proton emission, proton radioactivity and future prospects for TPCs.

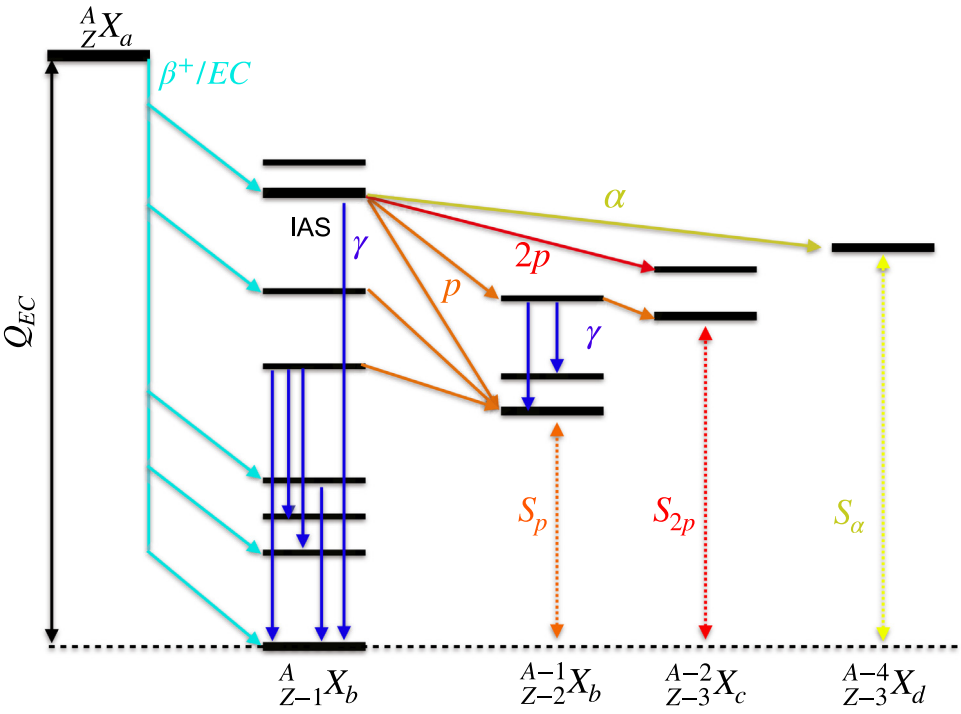

Fig. 22. Decay scheme for a $N < Z$ nucleus where different modes are shown.

6.1. Basic concepts on particle radioactivity and production methods

β-decay and β-delayed proton emission provide a rich field to investigate nuclear structure and astrophysics. The energy distribution of the emitted particles, half-life and decay rates depend on the β-decay strength. Transitions can be classified in terms of parity, spin and angular momentum change called Fermi or Gamow–Teller, the latter being the one without parity change and a maximum change of one unit of angular momentum. The intensity of the transition can be described by the ft value (f and t refer to phase-space factor and partial half-life, respectively):

$$ft = \frac{K}{g_v^2 B_F + g_A^2 B_{GT}} \tag{7}$$

where g_v and g_A are the free vector and axial-vector coupling constants, respectively. B_{GT} and B_F are the Gamow–Teller and Fermi strengths that are described by the transition between the initial and final states ruled by the isospin and spin operators. The constant K is:

$$K = \frac{2\pi^3 \hbar^7 ln2}{m_0^5 c^4} \tag{8}$$

The partial lifetime is described as the ratio between the total lifetime and the branching ratio for the decay of interest. The phase-space factor, which depends on the atomic number of the daughter and the kinetic energy of the β particle, can be calculated or inferred from tables. When the transition occurs between two isobars of the same multiplet, they are referred as Superallowed Fermi Transitions. In this case, the decay populates the Isobaric Analogue State (IAS) of the parent which is shifted by the Coulomb displacement energy (ΔE_c).

The energy of the emitted particle, E, depends on the excitation energies of the initial and final states (daughter and particle daughter, respectively) and on the separation energy of the emitted particle in the daughter. The intensity for a given channel can be expressed as:

$$I_x(E) = I_\beta(E_i)\frac{\Gamma_x}{\Gamma^i_{total}} \tag{9}$$

where $I_\beta(E_i)$ is the intensity of the β transition as a function of the energy of the daughter. Here x denotes the particle (p, n, d, t, α). Γ_x and Γ^i_{total} refer to partial width of a particular transition from the daughter and the total width of the initial state in the daughter. The spectrum of the emitted delayed particles depends on the mass region where the decay happens, or in other words, on the level density spanned in the Q_β-window ($Q_\beta - S_p$).

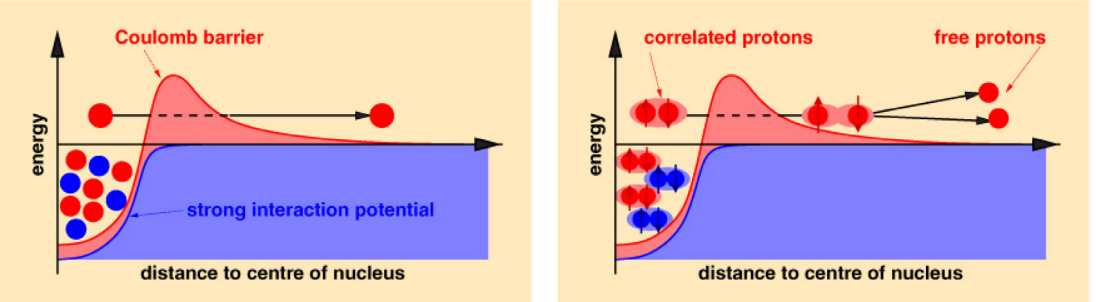

Fig. 23. Scheme depicting one- (left panel) and two-proton (right panel) emission. While the single proton emission mainly depends on the barrier height, the two-proton emission also depends on the correlation between the protons.
Source: From [128].

β-delayed proton emission is a powerful tool to investigate nuclear structure at large isospin imbalance and it is also of great interest for nuclear astrophysics (see Section 8). It can be used to investigate Gamow–Teller strengths, isospin mixing, nuclear masses, beta-neutrino correlations and the CNO cycle of astrophysical interest. The review about nuclear decay studies by Blank and Borge [125] contains a comprehensive description of these phenomena.

β-delayed proton emission competes with direct proton emission when approaching the proton drip line. The basic ingredient to describe direct nucleon radioactivity is the nuclear potential between the nucleus and the nucleon. The proton is stationary in this potential and has a very narrow decay width (Γ), or in other words, it decays through a very slow exponential process. Nucleons leave the nucleus through the tunneling process which depends on the available energy and the height or the barrier. In general, one can assume that the probability and thus the time of the process are proportional to the available energy. This tunneling process allows for the observation of proton radioactivity. Fig. 23 depicts the process of one and two proton emission from the core. The life time of this state (also called Gamow state) is:

$$T_{1/2} = \frac{\hbar ln2}{\Gamma} \tag{10}$$

Ref. [127] gives a simple prescription to calculate the decay width:

$$\Gamma = SN\frac{\hbar^2}{4\mu}exp\left[-2\int_{r_2}^{r_3} k(r)dr\right] \tag{11}$$

As explained in [127], in the case of proton radioactivity, S is the spectroscopic factor, $k(r) = \sqrt{2\mu|Q - V(r)|}/\hbar$ where Q is the decay energy and μ is the reduced mass of the system. $V(r)$ is the potential where the particle is confined, r_2 to r_3 being the classically forbidden region where the particle is below the barrier. The typical potential consists of a sum of terms describing nuclear and Coulomb interactions as well as centrifugal and spin–orbit terms. A comprehensive description of the proton and two-proton radioactivity theory can be found in [127,128]. It is however worth mentioning here the description of the proton radioactive process in terms of an intuitive model that models the interaction between the core and the protons in terms of Jacobi coordinate system. Such system is useful to represent the two main possibilities for two-proton radioactivity: diproton and sequential emission. One of the main reasons TPCs were introduced for the study of two-proton radioactivity is to enable the measurement of the correlations between emitted particles. In fact, such capability enables a powerful method to differentiate between a simultaneous and sequential emission of two protons from the core.

As mentioned before, the description of the three body system is usually done with the Jacobi coordinate system.

As shown in Fig. 24, the decay can be described with two equivalent coordinate systems (T (b) and Y (c) [127,134], in which two subsystems are defined. The decay energy E_T shared among three particles is:

$$E_T = E_x + E_y = \frac{k_x^2}{2M_x} + \frac{k_y^2}{2M_y} \tag{12}$$

where $M_x = \frac{m_1 m_2}{m_1+m_2}$ and $M_y = \frac{(m_1+m_2)m_3}{m_1+m_2+m_3}$. The relative momenta of the particles are $\vec{k}_x = \frac{m2\vec{k}_1 - m_1\vec{k}_2}{m_1+m_2}$ and $\vec{k}_y = -\vec{k}_3$. The vectors define the angle of emission between two particles and the core of mass M:

$$\begin{aligned} E_x &= \frac{k_x^2}{2\mu} \\ \vec{k}_x &= \vec{k}_1 + \frac{\mu}{M}\vec{k}_3 \\ k_y &= -k_3 \end{aligned} \tag{13}$$

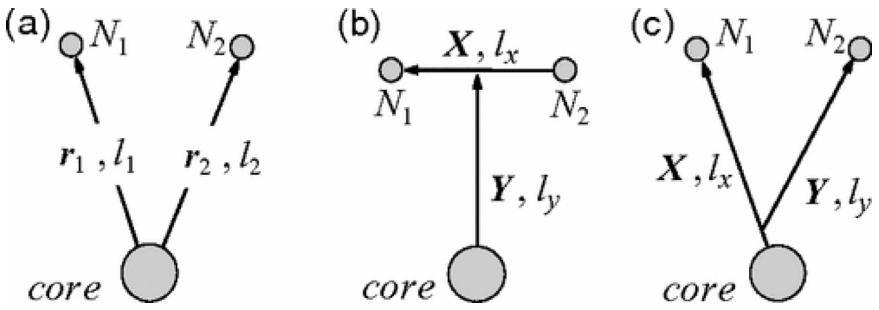

Fig. 24. Coordinate systems describing single-particle interactions: (a) Shell model system, (b) T Jacobi system. (c) Y Jacobi system. *Source:* From [134].

where μ is the proton-core reduced mass. These two Jacobian systems lead to two different coupling configurations. In both of them, the Hamiltonian is treated in a way where the Coulomb and nuclear potentials for the respective X and Y variables are separated. The decay amplitude is factorized into the product of two-body terms. The T model represents a diproton decay with one final state interaction (FSI). On the other hand, the Y Jacobi system is described by at least two FSI, in this case, between each proton and the core. For a convenient description of the system, the energy fraction (ϵ) and the relative angle between protons (θ_k) are chosen:

$$\begin{aligned} \epsilon &= \frac{E_x}{E_T} \\ cos(\theta_k) &= \frac{\vec{k_x} \cdot \vec{k_y}}{k_x k_y} \end{aligned} \tag{14}$$

This description has been very useful to infer the energy and angular correlations in two-proton emitters, as it will be shown later. For a more comprehensive description we refer the reader to the review article by Pfützner et al. that contains a detailed and complete explanation of the one- and two-proton radioactivity models [129].

6.2. β-Delayed proton emission studies with time projection chambers

The observation of the first β-delayed proton emission precursor (the nucleus that undergoes β decay) dates back to 1969 in an experiment performed using silicon detectors, which has been the preferred technology for this type of studies [135]. This finding spurred a plethora of experiments to observe other precursors, and to this day around 160 have been identified [128]. As mentioned earlier, most of the β-delayed proton emission studies, with the exception of those with astrophysical interest, are performed combining arrays of position-sensitive silicon detectors (double-sided silicon detectors), where the precursor is implanted to measure the proton. The β particle is usually detected in another silicon detector surrounding the one used for implantation. With this scheme, the background in the proton spectrum can be dramatically reduced. One of the main drawback of this system is the dead layer of the silicon detectors, which raises the lower limit of detection. Before time projection chambers were introduced to overcome this problem and improve detection efficiency at low energy, devices that combined silicon and gas detectors were developed for this type of studies [136,137]. These detectors leveraged some of the main capabilities of modern TPCs: drift time and energy loss measurements for particle identification. TPCs were introduced to overcome the major problems of the conventional setups, namely, individual detection of low energy protons and full geometrical acceptance. The TPC developed at CENBG (France) [10], based on gas electron multipliers (GEM), was devoted to the measurement of two-proton radioactivity but also enabled the unambiguous measurement of the β-delayed two proton emission from ^{43}Cr in an experiment performed at GANIL (France) [138,139].

Fig. 25 shows a β-delayed proton and two-proton emission of ^{43}Cr in the upper and lower panels, respectively. The left and right panels of the figure show the energy loss curve in both coordinates of the pad plane of the detector. Using the time signal of the arrival of the ionization electrons, a reconstruction of the three-dimensional tracks is enabled. With this information, the energy of the protons and their angular correlations can be inferred. As shown in the left panel of Fig. 26, a ratio of 34%–66% for the energy sharing between the protons (E/E_{2p}) was deduced for this type of decay, which supports the idea of sequential decay as the energy is not equally shared between the protons. In this context, the decay would proceed through an intermediate state in ^{42}Ti at 5.2 or 6.6 MeV, although the assignment was not possible. The sequential emission of the protons via intermediate states in the daughter nucleus is also supported by the isotropic angular correlation for the relative angle between them (right panel of Fig. 26). A few years later, the branching ratios for the β-delayed p, 2p and 3p emission of ^{43}Cr were measured in an experiment performed at the NSCL (USA) [140]. In this case, the optical TPC (OTPC) was used [11]. The tracking of the particles in this device is realized using the ultraviolet light (UV) produced during the electron amplification stage (see Fig. 27). The absolute branching ratios were determined to be

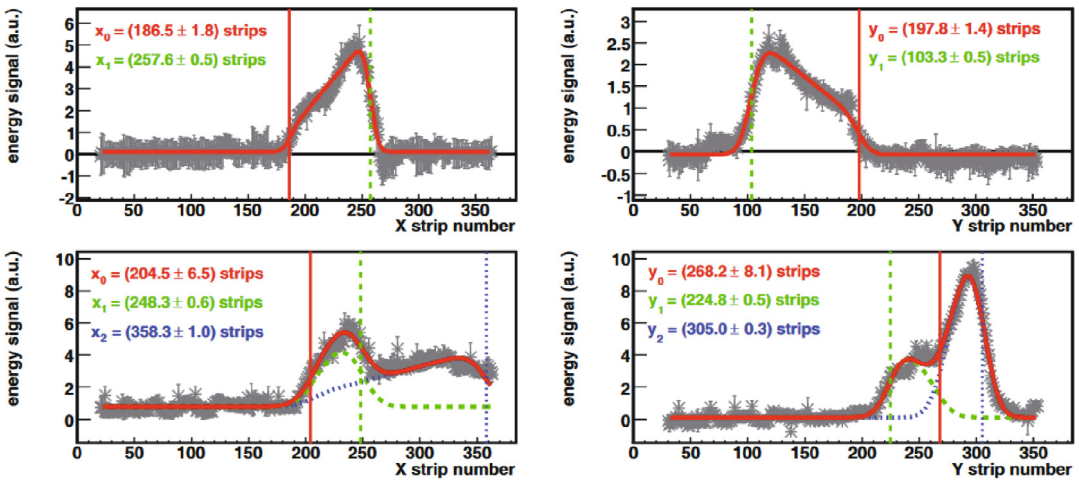

Fig. 25. Upper panel: Energy loss curves in x (left) and y (right) coordinates of a β-delayed proton event in ^{43}Cr. Lower panel: Same as upper panel but for β-delayed two-proton emission.
Source: From [139].

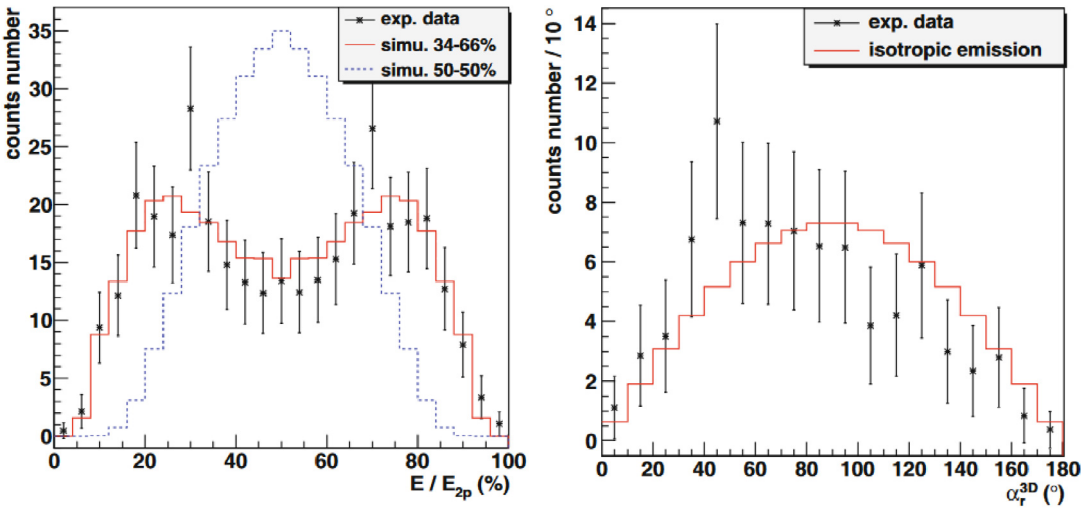

Fig. 26. Left panel: Energy sharing between two protons emitted in the β-delayed two-proton decay of ^{43}Cr. Right panel: Angular correlation between protons emitted in the β-delayed two-proton decay of ^{43}Cr.
Source: From [139].

81(4)%, 7.1(4)%, and 0.08(3)%, for the p, 2p and 3p channels, respectively. The branching ratio of the β-delayed 2p channel was attributed to a transition from the IAS of ^{43}Cr in ^{43}V to the ground state of ^{41}Sc, in good agreement with the results reported by [141]. This experiment also yielded a surprising result, a relatively large branching ratio 12(4)% for decays without emission of protons with several possible explanations: isospin asymmetry effects deduced when comparing the low branching in the mirror system (^{43}V to ^{43}Ca), an unknown proton separation energy in ^{43}V or decay to states with much larger γ width. The simultaneous high-resolution detection of γs and protons is obviously a compelling subject for future TPC devices.

In Refs. [139,140], the main goal was the measurement of two-proton radioactivity in ^{45}Fe. However, in the experiment presented in Ref. [11], the first observation of β-delayed three proton emission from ^{45}Fe was reported [142]. Several years later, the β-delayed 3p emission in ^{31}Ar was confirmed and the branching ratios for every channel determined [143]. With a branching ratio of 7%, the β-delayed 3p emission accounts for 30% of the total Gamow–Teller strength. The reason lies in the fact that delayed protons are coming from highly excited states above the IAS in the daughter nucleus. In addition, similarly to ^{43}Cr, the branching ratio to β-decay without proton emission is relatively large. Although the authors did not explain the reason in the manuscript, it might be caused by strong branching for γ decay.

Very often, the measurement of several exotic emitters is accomplished within a single experiment. Because of the rich amount of data these experiments produce, the establishment of this new technique motivated many experiments to hunt

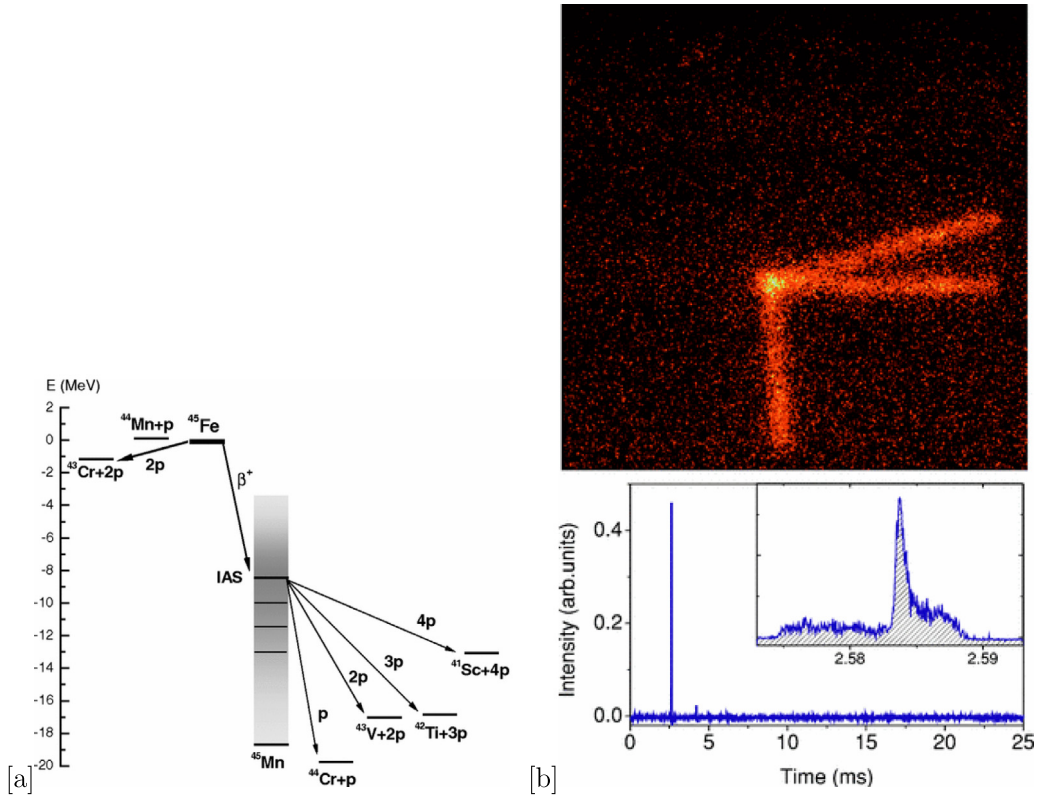

Fig. 27. (a) Decay scheme of ^{45}Fe showing different β-delayed particle emission channels. (b) Upper panel: An example of a β-delayed 3p emission of ^{45}Fe recorded with the OTPC. Lower panel: Energy loss (intensity) as a function of time. The pattern features a high spike that corresponds to the emission vertex.
Source: From [142].

down β-delayed proton emitters. For ^{44}Cr and ^{46}Fe, the branching ratios, half lifes and energy spectra were determined for the β-delayed proton emission channel [144]. For the ^{44}Cr a new single proton line was identified at 742 keV. For ^{46}Fe, the β-delayed two proton emission was identified for the first time. Despite the protons escaping the TPC volume, the authors were able to deduce that the decay proceeds through a state located 1.56 MeV above the IAS of the daughter ^{44}V with a branching ratio of 0.4(6)%. Although the statistics for the energy spectrum were poor, the background-free conditions that the TPC provides makes this technique unique when the detection of low energy particles is needed. This was again pointed out in a more recent experiment where the β-delayed proton and two-proton emission on ^{26}P and ^{27}S were measured [145]. The latter is an example on how the measurement with the TPC gave access to underlying physics. The upper panel of Fig. 28 shows the energy spectrum of β-delayed protons emitted after the decay of ^{27}S measured with the OTPC (top [145]) and with Si detectors (bottom [146]). It is clear that both methods span very different energy domains, and are complementary. The experiment with the OTPC observed a much stronger intensity below 2 MeV. Moreover, every event where two protons were observed was attributed to β-delayed two proton sequential emission, in contrast to the report of [146] that interpreted them as a ^{2}He emission from the IAS in ^{27}P to the ground state of the daughter ^{25}Al.

The two new lines observed in the β-delayed proton spectrum at 332 keV and 737 keV allowed for the reconfiguration of the decay scheme of ^{27}S originally presented in [146] (see Fig. 29). These lines correspond to transitions from the $3/2^{+}$ and $5/2^{+}$ states of ^{27}P to the ground state of ^{26}Si.

It is natural that the emission of protons after β-decay in neutron deficient nuclei is a common feature near the drip line where proton separation energies become smaller. On the other side of the chart of nuclides, the emission of charge particles after β-decay is allowed in nuclei with a small neutron separation energy, that can also be halo nuclei. To date, such an exotic decay mode has only been observed in very few neutron rich nuclei [130–132]. One of them is ^{6}He, for which the decay into α + d is allowed with a $Q_{\beta d} = 2.033$ MeV. This type of decay is interpreted as decoupled from the core, where one of the halo neutrons is transformed into a proton, forming a deuteron that it is emitted into the continuum. Several experiments found an unusually low branching ratio for this decay at around 10^{-6}, which was understood as an accidental cancellation in the Gamow–Teller matrix elements between the inner and the outer parts of the wave function. However, none of these experiments were able to determine the energy spectrum at low energy,

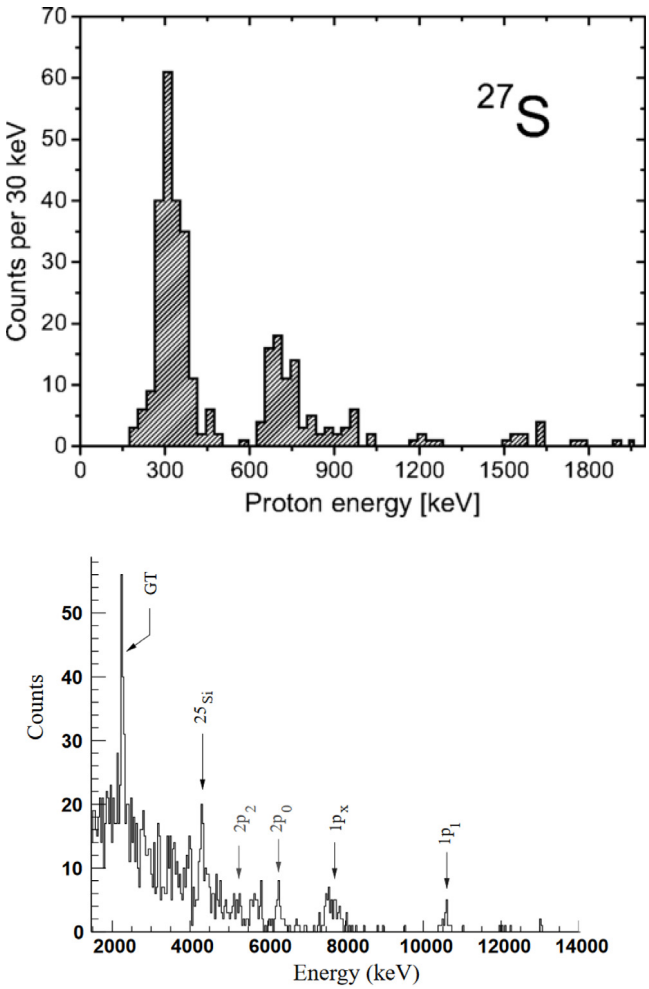

Fig. 28. ^{27}S β-delayed proton energy spectrum recorded with a TPC [145] (upper panel) and with Si detectors [146] (lower panel). The spectrum recorded with the TPC features an energy spectrum with a much lower proton energy threshold. This allowed to provide a more complete decay scheme from ^{27}S to ^{26}Si.

which is critical since a large part of the intensity lies in that range. Therefore, an experiment with a more sensitive device to low energy charged particles, such as a TPC, seems natural. The experiment was repeated using the OTPC [147] which enables the measurement of particles down to around 150 keV (in this case for both particles simultaneously), as shown in Fig. 30. This capability was crucial to determine a new branching ratio of 2.39×10^{-6} (with a transition probability of 2.39×10^{-6} s^{-1}), larger than the previous reported value of 1.65×10^{-6} for a deuteron energy above 350 keV [148]. The shape of the spectrum, which clearly points to a decay into the continuum, is in good agreement with theoretical calculations within an α+n+n model [149], although the absolute transition probability is not well reproduced (20% larger). This result demonstrates again the excellent performance of TPCs for background-free measurements of low energy charged particles.

When the neutron separation energy is $S_n < 782$ keV, the β-delayed proton emission from a neutron-rich halo nucleus is energetically allowed. One of the most favorable cases is ^{11}Be, which was recently proposed as a scenario where a halo neutron could undergo a decay into dark matter as an explanation for the neutron lifetime puzzle [150,151]. This topic has attracted great attention, and several works that rule out this scenario based on astrophysical and cosmological constraints have recently been published [152–154]. From the nuclear physics standpoint, the analysis of the neutron β^--decay symmetry limits the ratio for this channel to a point where the neutron lifetime discrepancy cannot be explained [155,156].

In fact, several decay channels are open in ^{11}Be but only $\beta\alpha$ ($Q_{\beta\alpha} = 2845.2$ keV) and more recently βp ($Q_{\beta p} = 280.7$ keV) have been observed. The branching ratio for the latter was indirectly measured via Accelerator Mass Spectroscopy (AMS) by determining the amount of remaining ^{10}Be, yielding a surprising value of $8.3(9)\times10^{-6}$ [157], much larger than predicted by theoretical calculations. Since this experiment measured the total branching ratio for the

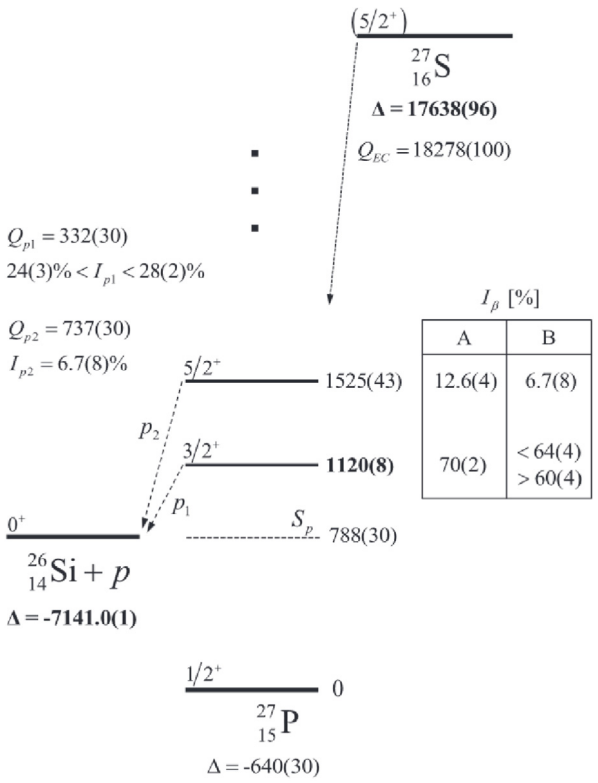

Fig. 29. Decay scheme of ^{27}S.
Source: From [145].

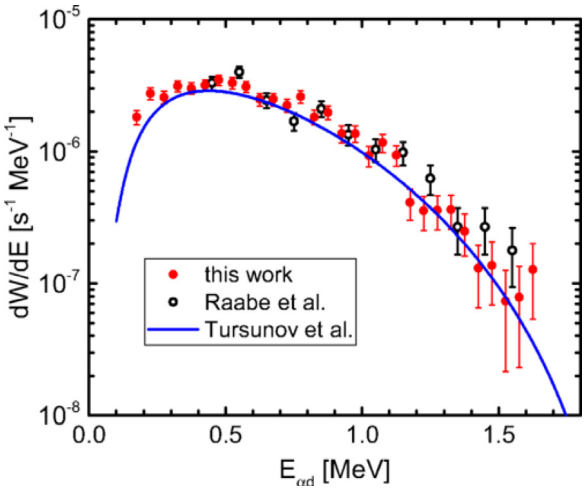

Fig. 30. Energy spectrum of the α-deuteron decay in ^{6}He.
Source: From [147].

decay of ^{11}Be into ^{10}Be, nothing could be inferred about possible unaccounted exotic decay channels beyond the standard model. Another explanation for this discrepancy is that the β-delayed proton emission from ^{11}Be proceeds through an unobserved resonance in ^{11}B.

In order to solve this conundrum, an experiment to directly measure protons emitted in the β-decay of ^{11}Be was performed [158] using the prototype Active Target Time Projection Chamber (pAT-TPC) [3]. Due to the very small $Q_{\beta p}$,

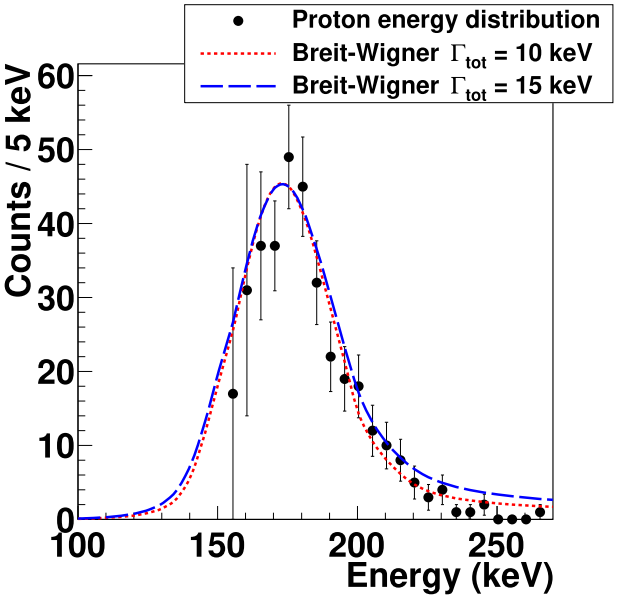

Fig. 31. β-delayed proton energy spectrum of ^{11}Be.
Source: From [132].

protons are emitted with an energy below 280 keV, which makes TPCs the ideal device for such measurement. In particular, and as pointed out before, it enables the measurement of this channel with a dramatically reduced background from β particles. From the experiment, a branching ratio of $1.3(3)\times10^{-5}$ was inferred, in agreement with the previous indirect experiment. This result, within error bars, does not leave room for significant dark neutron decay. Moreover, the energy distribution of the protons was also obtained (see Fig. 31). The narrow shape of the distribution suggests that the decay proceeds through a resonance in ^{11}B with a width of around $\Gamma = 12(5)$ keV and an energy of $E = 11.425(20)$ MeV, right above the proton emission threshold. The theoretical calculations presented in [132] also support the idea of a sequential process rather than a phase-space decay. The idea of resonances located right above the particle emission threshold is widely accepted. One of the better known cases is the emission of α clusters around the energy threshold, the ^{12}C Hoyle state being the most famous (see also Section 5). Theoretical calculations based on the shell model embedded in the continuum (SMEC) favors the existence of a $J^\pi = 1/2^+$ resonant state in ^{11}B that can be understood as a core-coupled proton state in the ^{10}Be+p system, completely orthogonal to ^{7}Li+α [159]. The result of other similar experiments performed with GADGET [15] and with the OTPC [160] will be key to shed light on the nature of this exotic decay.

6.3. Two-proton radioactivity

When the separation energy of two protons becomes negative, they can be emitted spontaneously from the ground state. The discovery of two-proton radioactivity is rather recent, and dates back to 2000. Two experiments performed almost simultaneously at GANIL [161] and GSI [162] reported the first observation of two-proton radioactivity from the ground state of ^{45}Fe. The very few counts measured in both experiments still allowed for the extraction of an energy spectrum that featured a prominent peak at around 1.1 MeV. The results were later confirmed by another experiment performed at GANIL [163].

As discussed in the introduction of this section, one of the most fundamental questions in two-proton radioactivity is whether the emitted protons are correlated or they follow a pure phase space decay. Such correlations can be inferred from the opening angle distribution of both protons [164]. Phase-space decay features an isotropic angular distribution with energies from zero to the total decay energy. When assuming three-body models [165–167], the angular distribution is characterized by a double humped distribution that depends on the initial wave function. The ^{2}He case, if it exists, would be characterized by a sharp distribution centered around 30°. TPCs were introduced to shed light on the radioactivity mechanism and on possible correlations. One of the pioneering proton radioactivity experiments with TPCs [168] was performed with the CENBG device [10]. Due to the large production rates and previous results, ^{45}Fe was selected for the study of two-proton radioactivity with TPCs. This experiment allowed for the first direct observation of both proton tracks simultaneously yielding an energy spectrum in very good agreement with the previous experiments. Seven events were unambiguously identified as two-proton radioactivity and the deduced branching ratio and half life of 0.78 and 3.6 ms, respectively, were found to be in good agreement with previous experiments [139]. The tracking capabilities of the TPC also enabled the reconstruction of the emission angles. As shown in the panel *a* of Fig. 32 where the energy correlation

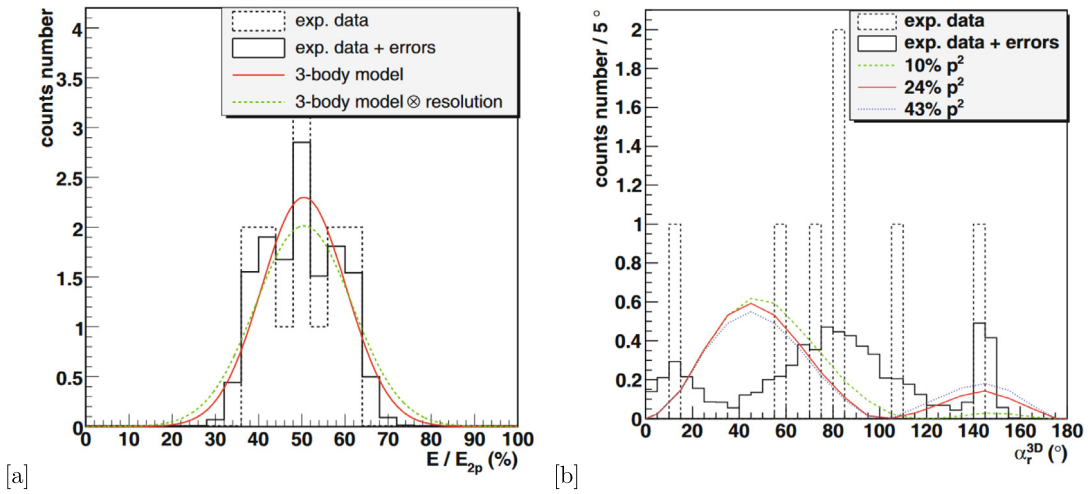

Fig. 32. Energy (panel a) and angular (panel b) correlations between both proton emitted from ^{45}Fe.
Source: From [139].

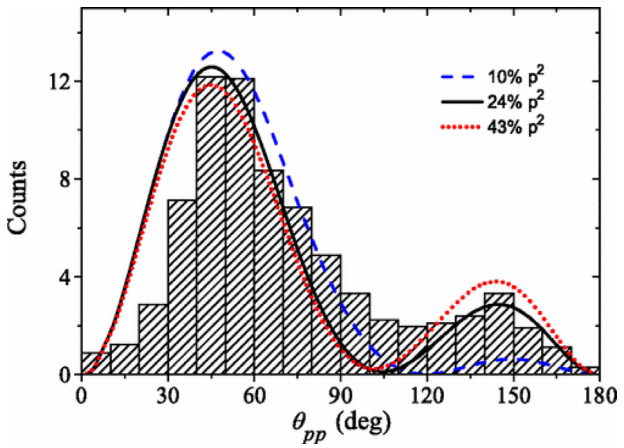

Fig. 33. Angular correlation between both proton emitted from ^{45}Fe.
Source: From [169].

between two protons is shown, the energy is equally shared between them to favor the penetration through the barrier. Moreover, only three-body theoretical models (SI^2M model) describing the emission as a dynamic interplay between core-proton and proton–proton, as explained in the introduction of this section are suitable. The low statistics obtained in this experiment only allowed to extract a very preliminary conclusion about the configuration within the $f-p$ shell model proposed by Grigorenko et al. [165–167]. However, another experiment performed with the OTPC, where larger statistics were obtained [169], unveiled that the ^{45}Fe ground state is characterized by strong p^2 and f^2 configurations by comparing the angular correlation between both emitted protons with the $f-p$ shell model (see Fig. 33). Also, the possibility of ^{2}He emission was ruled out.

Similar results were obtained in the study of the two-proton radioactivity of ^{54}Zn using the CENGB TPC [170] where a p^2 contribution of around 30% was found, with a probability of 0.99. The most recent study of two-proton radioactivity with a TPC dates from 2014 with the observation of this decay in ^{48}Ni using the OTPC [144]. With only six events detected, the half-life and the branching ratio were determined ($2.1^{+1.4}_{-0.6}$ ms and 0.7 ± 0.2, respectively). Also, the authors used the Jacobi coordinate system two infer energy and angular correlations. The energy fraction (ϵ) and the cosine of the angle between Jacobi momenta were compared to a model assuming both valence protons to be in a configuration with a mixture of p^2 and f^2, as done for the ^{45}Fe case. An f^2 configuration in the initial wave function was deduced for the few events studied in this work. The low statistics collected in this experiment leave the door open to future experiments when a more intense radioactive ^{48}Ni beam becomes available.

The quest for two-proton emitters is very active, ^{67}Kr being the most recent discovery [171], although no TPCs were used and therefore, angular and energy correlations could not be determined. Clearly, the compelling capabilities that TPCs provide makes them instrumental in the study of the two-proton radioactivity phenomena.

6.4. Summary and outlook

Time Projection Chambers were introduced for the study of two-proton radioactivity and rapidly became a powerful tool to perform experiments where radioactive nuclei emit one of more charged particles after undergoing decay. The use of TPCs for β-delayed charged particle emission studies enabled the detection of very low kinetic energy particles which allowed to complete and improve previous studies. Similarly, in the two-proton radioactivity domain, the study of energy and angle correlations, which yield relevant information about the mechanism and nature of the process, are possible due to the tracking capabilities of TPCs.

Such studies will benefit from the current improvements being implemented in some of the TPCs devoted to low-energy nuclear physics. TPCs such as the AT-TPC [4] or SpecMAT [5] are placed inside a magnetic field that enable the measurement of the particle rigidity and vastly extend the energy dynamic range. These two features facilitate particle identification and enable the measurement of several decay channels with very different energy at the same time. Other systems like GADGET [15] or TexAT [8] are combined with gamma detectors that are needed to study the competition between gamma and charged particle emission.

All the studies presented in this section were performed by producing the ion of interest by fragmentation or ISOL techniques, which, in most of the cases, limited the study to the ground state of the decaying system or in lower decaying states. TPCs in active target mode offer an alternative method capable of providing new observables. The nucleus of interest can be produced by resonant scattering with excitation energies well above the resonance. In this scenario, an enhancement of emission probability due to clustering can be expected. This technique would allow to study the competition between sequential and simultaneous two-proton emission within the full excitation function covered inside the detector.

7. Fission and fusion reactions

7.1. Fission

Nuclear fission, discovered in 1938 [172], provides a tool to study the nuclear potential energy and its evolution. Fission is a field that involves a unique combination of macroscopic and microscopic effects. The macroscopic effects are illustrated by the liquid drop model that predicts the onset of fission where the Coulomb forces lead first to strong deformation and then to fission. However, by adding microscopic corrections one is able to reproduce properties such as fission isomers [173]. The detailed study of the fission process has provided evidence of the influence of properties like nuclear elongation, mass asymmetry, spin and excitation energy [174]. Fission is a type of nuclear decay in which the nucleus splits into fragments releasing energy. In such transition the nucleus forms a single compound nucleus that overcomes a fission barrier and reaches the scission point generating the fission fragments. In this transition an interplay of macroscopic and microscopic effects in the initial and final states has to be considered. Also dynamical effects should play an important role to explain various aspects of fission.

The study of fission cross sections, especially in short lived nuclei, gives a fundamental input information for modeling stellar element nucleosynthesis via the r and s processes, as well as in the design of advanced nuclear reactors, transmutation of nuclear waste or innovative fuel cycles like the Th/U cycle [175]. In the past decades, the advances in rare-isotope production, detection techniques as well as theoretical advances together with computing power have driven large improvements in the knowledge of nuclear fission. When induced and spontaneous fission were first discovered, the only way to study them experimentally was in direct kinematics, where a stable or very long lived light projectile impinges a heavy target to induce fission. With the new rare isotope accelerators available nowadays, inverse kinematics becomes a new possibility that revolutionizes the field, increasing substantially the extension of fission knowledge over the nuclear chart [176].

One of the main observables needed to clarify the topic are the fission fragment mass distributions. Capture reactions of charged particles or neutrons can be used to populate low excited compound nuclei for fission studies. The lowest possible energy corresponds to spontaneous fission starting from a ground state such as in ^{252}Cf for instance.

However, even with the new data obtained with rare isotopes, accurate fission models are still mostly phenomenological, lacking a strong prediction power. For this reason, one of the present main goals of this field is to improve the predictive power of fission models. Unfortunately, many of the nuclei of interest are short-lived and difficult to study in the laboratory. Fig. 34 shows a sample of nuclei of interest from Z=85 to Z=92 and neutron number ranging 118 to 142. For example within the isotopic chain Z=90 with neutron numbers ranging from N=127 to N=139, only N=139 has a half life longer than 2 years. Neutron induced fission cross sections [178] are needed for reliable evaluation of the r-process path. A possibility to study these cross sections when direct measurements are not available is provided by surrogate-reaction studies [179] like nucleon-transfer reactions.

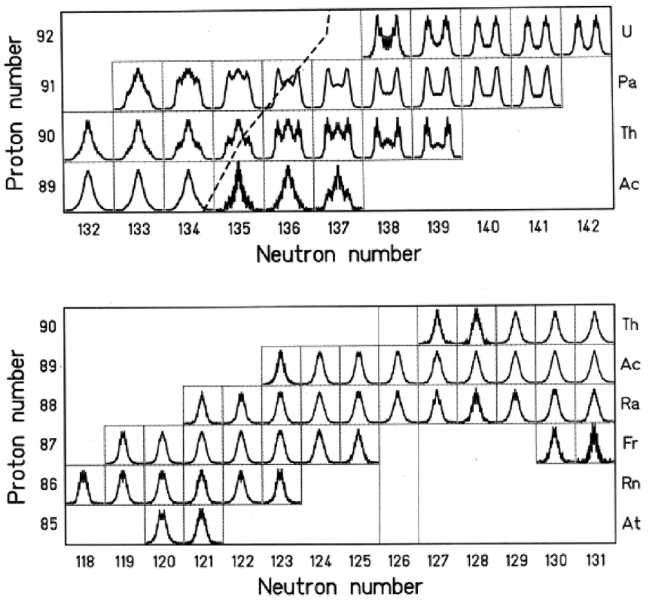

Fig. 34. Measured fission-fragment nuclear-charge distributions in the range $Z = 24$ to $Z = 65$ from Ac to U (upper part) and from At to Th (lower part) in electromagnetic-induced fission are shown on a chart of the nuclides. The dashed line in the upper part indicates the transition from symmetric to asymmetric fission. Nuclei on the right-hand side of this line were expected to predominantly show asymmetric fission, while nuclei on the left-hand side were expected to show symmetric fission with higher probability.
Source: From [177].

GSI (Germany) pioneered these studies in the 2000s with the fission of relativistic radioactive beams in inverse kinematics induced by Coulomb excitation. In those experiments systematic fission studies of several dozens of nuclei in the neutron-deficient Actinide-U region were performed, including recent campaigns with SOFIA [177]. An example can be seen in Fig. 34 where fission fragments with charges from Z=24 to Z=65 were measured. The SOFIA experiment [12] took place at GSI where the heavy-ion accelerator can provide and unambiguously identify secondary actinide beams at relativistic energies up to neptunium isotopes. Actinides are identified event-by-event thanks to a Triple-MUSIC (MUltiple Sample Ionization Chamber) to get not only the ΔE measurement from the energy loss collected on the anode plane, but also the horizontal angle from the electron drift times in a time-projection-chamber manner. Depending on the nuclear charge of the target and on the impact parameter, different reaction channels are opened: nuclear reactions (for small impact parameters) and Coulomb excitation (for high-Z targets and large impact parameters). Coulomb excitation populates the giant dipole resonance (GDR) with an excitation energy around 12 MeV. The excited compound nucleus may decay via fission. To maximize this low-energy fission induced by Coulomb excitation, high-Z targets are used. Two uranium targets and one lead target are mounted in an active target as cathode.

It is also possible to produce neutron-rich heavy fissionable nuclei with multi-nucleon transfer reactions [180]. These nuclei cannot be accessed via particle capture or heavy-ion fusion because these reactions induce fission. In addition, excited states of the compound nucleus populated in multi-nucleon transfer range widely from below the fission barrier to higher energies, providing a perfect tool to measure the excitation energy dependence of the fission fragment yields. Multi-nucleon transfer reactions can also be used as a surrogate reaction technique to determine neutron-induced fission cross sections [181].

The Neutron Induced Fission Fragment Tracking Experiment (NIFFTE) collaboration designed a TPC (fissionTPC) based on micromegas technology to study fission [13]. The main goal is to study uncertainties of previous measurements, in particular the implications of α and fission fragment identification, target and beam non-uniformity and the cross section uncertainty of the reference in ratio measurements [182]. The use of this detector is limited to isotopes where macroscopic quantities are available. For much lower quantities only reactions in inverse kinematics can provide access to quantitative information.

In most transfer-induced fission experiments very light projectiles have been traditionally used [183], restricting the transfer to a few nucleons. The lack of available targets is a second limitation to the systems that can be studied. Because of that, inverse kinematics can be used, broadening the variety of systems by turning the target into a projectile. A big advantage of the use of inverse kinematics, besides the fact that a very short-lived nucleus can be used, is the high kinetic energy in the laboratory system of the fission fragments, giving access to much higher resolution for fragment identification, which is impossible in normal kinematics. One of the first fission reactions measured in inverse kinematics is the study of a ^{238}U beam on a ^{12}C target with the active target MAYA in GANIL [184]. This experiment produced a wide

variety of neutron-rich fissioning systems bringing new observables as compared to the surrogate reaction study, due to the kinematic boost of the fission fragments. In order to apply the data obtained via transfer reactions to neutron-induced fission, a full understanding of the properties of the compound nucleus is needed.

In general the excitation energy distributions and the fission probabilities of the fission products from the transfer reaction are measured, but in order to fully understand the reaction mechanism, the evolution with incident energy needs to be investigated. In a solid target experiment, this requires different beam energies. This is not a problem with stable beams, but it becomes a major challenge for radioactive beam experiments.

Active targets allow not only for an increase in the target thickness by one order of magnitude, with respect to solid target experiments, but also to explore the evolution of the transfer mechanism with incident energy, without the need to modify the energy of the incident beam. With these detectors, the two fission fragments can be simultaneously detected, and a three-dimensional view of the process can be obtained on an event-by-event basis.

Typical active targets like the AT-TPC [4] and ACTAR [184] can reconstruct the reaction vertex with a resolution of several millimeters, and provide either high sensitivity or a large number of measurements of the cross section from a single beam energy. For instance, even with radioactive beam intensities as low as 100 particles per second, a particular target-beam combination that may reduce the fission barrier by about 20% would increase the fission cross section by 2 orders of magnitude and could still be measured. A numerical example can be found in Ref. [185]. The use of active targets provides the needed sensitivity, allowing to resolve the long-standing question concerning the observed fission barriers of proton-rich nuclei by way of their direct measurement. The fission rates will determine how detailed the investigations of low energy fission can be. Understandably, lower values of observed fission barrier heights will be favorable, which appears quite likely for neutron-deficient nuclei in the region around shell closures $Z = 82$ and $N = 126$.

7.2. Fusion

The study of fusion reactions with radioactive ion beams at energies near the Coulomb barrier has resulted in the discovery of a variety of interesting effects. Fusion reactions are strongly influenced by coupled channel effects in the entrance channel. For example, the total fusion cross sections for exotic "neutron halo" nuclei such as ^{6}He typically show a suppression at energies above the Coulomb barrier, with a slight enhancement at sub-barrier energies, when compared with no-coupling one-dimensional barrier penetration models. It appears that these effects result from couplings to the neutron-transfer and breakup channels [186]. Coupled channel effects may have a strong influence on sub-barrier fusion, often related to neutron transfer channels with positive Q values [187,188]. Incomplete fusion is a heavy-ion induced reaction at low incident energies in which only a part of the projectile fuses with the target nucleus and forms an incompletely-fused composite system. At energies near and above the Coulomb barrier, in general, the interactions between two heavy ions are mainly dominated by fusion of the entire projectile with the target nucleus, termed as complete fusion (CF). However, a substantial fraction of incomplete fusion (ICF) has also been observed at low incident projectile energies [189,190].

To date, however, these studies have concentrated on relatively light nuclei such as ^{6}He, ^{8}He [191], and ^{11}Li [192] due to the limited availability of heavier projectiles near the neutron or proton drip-lines at Coulomb-barrier energies. The new generation of radioactive ion beam facilities, such as FAIR/GSI (Germany), GANIL (France), RIBF (Japan) and FRIB (USA), will provide a much wider spectrum of projectiles to choose from. Nevertheless, since the most proton and neutron-rich nuclei will often be produced at low intensities, and beam-time allocations at these facilities will be very competitive, it is imperative to develop highly efficient methods to study nuclear reaction mechanisms using these exotic beams. The use of active targets in this domain has a number of important advantages for working with low-intensity beams, including very high efficiency for detecting reaction products and measuring their angular distributions with virtually 4π solid-angle coverage, much larger available target thickness (since the reaction vertex can be directly imaged), and the ability to measure an excitation function as the projectile slows down in the target gas. Solid targets may also be used by mounting them within the gas volume. A pioneering experiment has been successfully run using the pAT-TPC with a ^{10}Be beam [193]. Although it is radioactive, ^{10}Be is strongly bound therefore its fusion excitation function closely follows expectations for stable nuclei. The excitation function for the fusion of ^{10}Be with ^{40}Ar was measured in this experiment [193]. The results are shown in Fig. 35. In following developments, THGEM technology [194] was introduced as electron pre-amplifier in order to avoid working with a quencher gas, that introduces undesired target contamination.

7.3. Summary and outlook

Although much work has been done in the past two decades to advance the understanding of fusion and fission processes, the field is actively growing, with many research groups still focusing on this topic. Although stable isotopes are still a main source of information to fully comprehend the big picture, radioactive beams combined with inverse kinematics can also play a major role, providing a bigger landscape of nuclei to study. With radioactive beams, a very effective way to measure in inverse kinematics and at the same time obtain the energy dependence of the excitation energy is to use active targets. Several experiments have pioneered the field using MAYA and the AT-TPC, and more are proposed with these and other detectors such as ACTAR. The pilot experiments show very promising results, opening the door for active targets to become a key ingredient in studying specific properties of fusion and fission at the borders of nuclear stability.

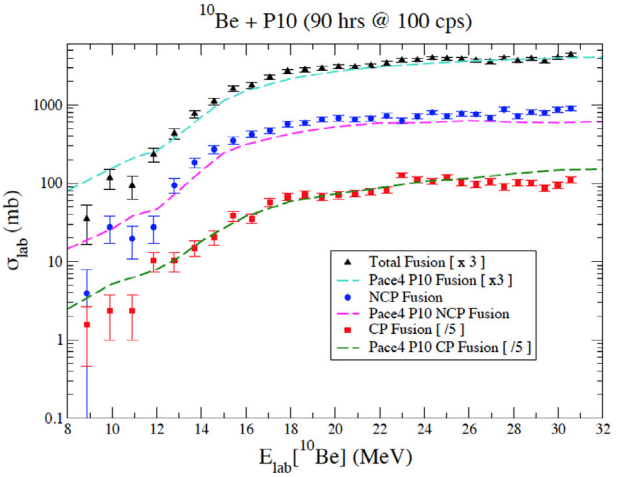

Fig. 35. Experimental total fusion cross section (triangles), fusion with neutron emission (dots), and fusion with emission of charged particles(squares). The curves are calculations using the PACE4 code. The total fusion cross section and prediction have been multiplied by a factor of three, and the charged-particle associated cross section and prediction have been divided by a factor of five, in order to sufficiently separate the data sets on this plot.
Source: From [193].

8. Nuclear astrophysics

Dependable prediction of nucleosynthesis yields and other astrophysical observables require stringently constrained nuclear input data. Out of various nuclear physics inputs, nuclear reactions play a vital role, especially capture reactions, for example (n, γ) and (p, γ) in *r*-process and in *rp*-process, respectively, and also in quiescent burning. In many astrophysical environments, the α-particle induced reactions, which includes (α, γ), (α,p) and (α,n) type reactions, play a pivotal role. Out of these α-particle induced reactions, (α, γ) reactions drive the nucleosynthesis and energy generation in quiescent burning, e.g. ^{12}C(α, γ)^{16}O. Due to the lower temperatures in the quiescent burning environments, precise measurements of these reactions are required at very small center-of-mass energies. Many important reaction rates remain uncertain in the Gamow window of relevant energies, even after decades of experimental efforts. On the explosive nucleosynthesis side, the αp-process is thought to occur in type-I X-ray bursts (XRBs). This reaction sequence has been shown to directly impact the XRB light curves, a direct observable [195,196]. Two main (α,n) reactions, i.e. ^{13}C(α,n)^{16}O and ^{22}Ne(α,n)^{25}Mg, are the main sources of neutrons in the slow neutron-capture process called *s*-process. Many (α,n) reactions have been found to be relevant for nucleosynthesis of light nuclei in the *r*-process in neutrino driven winds [197]. Both (α,p) reactions in XRBs and (α,n) reactions in neutrino-driven winds proceed through a region of β-unstable nuclei located on the proton-rich and neutron-rich sides of the valley of stability. These reactions therefore require experiments with radioactive ion beams performed in inverse kinematics. Rates for the types of reactions discussed here remained uncertain till now due to limited luminosities that are achievable at low center-of-mass energies, or due to the challenging production of high intensity radioactive ion beams. Use of active targets provides a much-needed increase in luminosity which enables direct and/or time-reverse measurement of capture reactions with stable beams and direct measurement of (α,p), (α,n) reactions. Thanks to the versatile possible use of time projection chambers from transfer reactions to decay experiments, they also create opportunities to constrain the reaction rates via indirect measurements. In this section, we discuss the current and future prospects of different types of measurements with active-target time projection chambers. The goals of the main methods discussed here are to constrain the nuclear physics inputs, including direct measurements, time-reversed (e.g. photo-dissociation) measurements for capture reactions on stable isotopes, and indirect measurements including transfer reactions as well as β-delayed particle emission experiments.

8.1. Time-reverse measurement of capture reactions with high intensity γ-ray beams

The radiative capture of hydrogen or helium (i.e. (p, γ) or (α, γ)reactions) on light nuclei such as carbon, nitrogen, and oxygen are some of the most important processes in stellar nucleosynthesis, especially in the quiescent stellar burning process [198]. These capture reactions have been studied for years in both normal and inverse kinematics. Due to extremely small cross-sections (in the picobarn region), these reaction rates remain uncertain in the Gamow window. It was discussed in recent works that if the reaction products in capture reactions are stable, a considerable improvement in the luminosity can be achieved by measuring the time-reversed reactions, i.e. (γ,p) or (γ, α) [199]. The expected

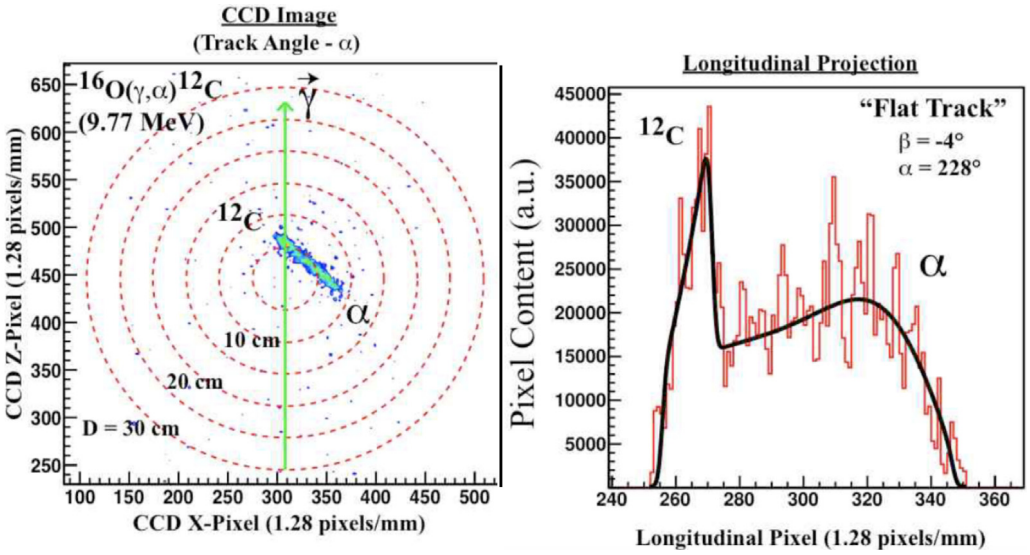

Fig. 36. An α + ^{12}C track recorded by the CCD camera from the dissociation of ^{16}O by 9.77 MeV gamma-rays (left panel). Right panel shows the longitudinal projection of the same track. This figure demonstrates that the ^{12}C track (along with the α-particle track) is visible even though the ^{12}C recoil energy is very small.
Source: Adapted from [201].

improvement in count rate comes from the reciprocity theorem for nuclear reactions [200]. The two cross sections are related to each other by the following expression (DiGiovine et al. [199])

$$\frac{\sigma(\gamma,\alpha)}{\sigma(\alpha,\gamma)} = \frac{\omega_{\alpha,\gamma}\kappa^2_{\alpha,\gamma}}{\omega_{\gamma,\alpha}k^2_{\gamma,\alpha}} \tag{15}$$

where $k_{\alpha,\gamma}$ and $k_{\gamma,\alpha}$ are the wave-numbers for capture and photo-disintegration channels, respectively, and $\omega_{(\alpha,\gamma)}$ and $\omega_{(\gamma,\alpha)}$ are the associated spin multiplicity factors. This ratio can provide up to two orders of magnitude enhancement. Moreover, active targets provide thick gas targets which can further enhance the luminosity by a factor of 10 to 100. Therefore, active targets and high intensity γ-ray beams can help constrain the capture cross-sections at very small center-of-mass energies. These small center-of-mass energies are typical for quiescent burning where temperatures are lower compared to explosive nucleosynthesis sites.

^{12}C(α, γ)^{16}O during the helium-burning phase is a key reaction in deciding the ratio of carbon-to-oxygen in stars [198]. It has been shown that the measurement of this reaction rate with an accuracy of better than 10% is required in the Gamow window (∼300 keV) [198]. In this context, the optical readout time projection chamber (O-TPC) has been commissioned with intense ∼9.5 MeV γ-ray beams from the HIγS facility at Duke University [201]. For the test run, experimenters used an O-TPC detector operating with a CO_2(80%) + N_2(20%) gas mixture at 100 Torr. The in-beam tests were performed with linearly polarized gamma-ray beams (4.5×10^7 γ/s) and circularly polarized γ-rays beam (1.3×10^8 γ/s) on the target. Fig. 36 illustrates an example event that shows the two-dimensional projection of ^{12}C and alpha tracks from the photo-dissociation of ^{16}O recorded with a CCD camera and signals from photo-multiplier tubes (PMTs). The measured dE/dx along the track (together with the track length) and the line shape of the light signal allowed for the separation of ^{12}C and α. This test measurement opened up possibilities to perform photo-dissociation studies on stable targets in order to constrain the astrophysical reaction rates at very low center-of-mass energies with the O-TPC and other TPCs being run in active mode. Moreover, the choice of gas as a target can be significantly improved in order to reduce background reactions. For example, the systematic study of M-THGEM in pure CO_2 showed a workable avalanche gain can be achieved up to 150 Torr [202].

8.2. Direct measurement of (α,p), (p, α) and (α,n) reactions for explosive nucleosynthesis

Type-I X-ray bursts are powered by nuclear reaction sequences that include the triple-α process, the αp process and *rp* process [195,203,204]. Once the temperature reaches $\sim 5 \times 10^8$ K, a breakout from the hot CNO cycles via ^{15}O(p, γ) and via ^{18}Ne(α,p) becomes efficient, which opens the door for two long reaction chains. One of these chains is the αp process. Rates in the αp process become particularly important when destruction via (α,p) reactions are competitive with the (p, γ) reactions. Such points in the nuclear flow are called branching points. It has been shown in various sensitivity studies that X-ray burst light curves, a main focus of astronomical observations of XRBs, are sensitive to various (α,p) reactions e.g. ^{22}Mg(α,p)^{25}Al [196,205,206].

On the other hand, (p, α) reactions become important when the α emission threshold is lower than the proton emission threshold, which leads to competition between (p, γ) and (p, α) reactions [207]. These situations lead to NiCu and ZnGa cycles in type-I X-ray bursts. The majority of (α,p) and (p, α) reactions relevant for X-ray bursts lack experimental constraints beyond some nuclear structure details. Therefore, direct measurement of these reaction rates will provide the required nuclear input in order to constrain X-ray burst light curves as well as the composition of burst ashes.

Active targets and time projection chambers are an ideal tool to perform such measurements. The use of pure gases, such as H_2 and He, as target provides relatively background free spectra for (p, α) and (α,p) reactions. The emission of charged particles in the outgoing channel helps to track all the reaction products or/and get energy loss information for particle identification. The beam tracking along with tracks of reaction products provide a complete reconstruction of kinematic variables and full excitation function with single beam energy. Here we discuss the example measurement of (α,p) and (α,n) reactions with various active targets in the recent years.

8.2.1. Direct measurement of (α,n) and (α,p) reactions with Multi-Sampling Ionization Chamber

The Multi-Sampling Ionization Chamber (MUSIC) at the Argonne National Laboratory (ANL) is an active target system with 18 anode strips allowing the measurement of an excitation function covering a large energy range. The MUSIC distinguishes heavier reaction products as well as beam particles using energy loss information. For details about the MUSIC detector and analysis techniques, refer to [14]. In order to demonstrate the working operation, quality direct measurements of the previously measured reaction ^{17}O(α,n)^{20}Ne were performed with the MUSIC detector at Argonne National Laboratory. The main advantage of the MUSIC detector is that it provides nearly 100% detection efficiency of the reaction products. MUSIC successfully identifies reaction products differing by one atomic number, i.e. ΔZ=1. Energy loss signals measured in the strips of the MUSIC detector for different channels in the ^{17}O+α reaction are displayed in Fig. 37 which shows a clear identification of various reaction products from the beam signal. Recent (α,p) and (α,n) measurements with the MUSIC detector were aimed at constraining the nuclear physics input for reliable predictions of ^{26}Al production in the Galaxy. ^{26}Al serves as a trace for ongoing nucleosynthesis in our Galaxy as it emits a 1.809 MeV γ-ray line associated with its radioactive decay. A reaction-rate sensitivity study identified ^{23}Na(α,p)^{26}Mg and ^{26}Al(n, α)^{23}Na as important reactions in massive stars (M > 8M$_\odot$), the most likely production sites of ^{26}Al. ^{23}Na(α,p)^{26}Mg and ^{23}Na(α,n)^{26}Al (time-reversed ^{26}Al(n, α)^{32}Na) were simultaneously measured with the MUSIC detector using a ^{23}Na beam and a detector filled with helium gas [208]. This recent measurement by Avila et al. [208] using the MUSIC detector confirmed the previous results of reference [209] and helped to resolve the discrepancy at higher energies. These measurements open up a window for future measurements of (α,n) and (α,p) measurements with radioactive ion beams which are currently being planned.

8.2.2. Direct measurement of (α,p) reactions with AT-TPC

In recent years, advances in XRB observations and modeling opened a new window to constrain the mass–radius relation of the neutron star through model-observation comparisons [210]. As described earlier, XRB light curves are powered by nuclear reactions and XRB models are sensitive to the various nuclear physics inputs (e.g. nuclear reaction rates). Therefore, reliable nuclear physics data is needed to validate the assumptions of the astrophysical models through model-observation comparison and extract the neutron star compactness.

^{22}Mg(α,p)^{25}Al is one of the most important reactions for XRBs which directly impacts the XRB light curves and hence hinders extraction of the neutron star compactness through model-observation comparison. Current experimental information on this reaction rate comes from the indirect measurement ^{28}Si(p,t)^{26}Si through which resonances in the compound nucleus ^{26}Si were explored [211]. This experimentally constrained reaction rate is more than a factor of 100 lower than the Hauser–Feshbach (HF) based model predictions in the relevant XRB temperature range above 0.7 GK. These two rates lead to very different results when used in XRB model calculations. Therefore it is important to directly measure this reaction cross section to reduce this very large uncertainty. Recently, this reaction has been measured with the AT-TPC at the ReA3 facility, NSCL [212]. A re-accelerated ^{22}Mg beam at 5 MeV/u was delivered to the AT-TPC which was filled with 600 Torr of He:CO_2(95:5). At this pressure, the beam completely stops inside the active volume and hence allows measurement of the complete excitation function with a single incoming beam energy. Fig. 38 shows an example beam event, where the charge deposition along the beam axis in the AT-TPC is shown. Fig. 39 shows an example event where a two-dimensional projection of the proton track on the pad-plane is shown. This new measurement by Randhawa et al. [212] reports factor of 8 lower reaction rate compared to HF based model predictions and more than a factor of 100 higher reaction rate compared to previous lower limit based on Matic et al. [211]. With the current measurement the reaction rate in the Gamow window for XRBs is determined experimentally for the first time, and its uncertainty is dramatically reduced.

Another important reaction for type-I X-ray bursts is ^{17}F(α,p)^{20}Ne which directly impacts the light curve in XRB models [196]. This reaction affects nuclear burning in between the bursts and in the shallower depths of accreting neutron stars. This reaction has been recently measured with the MUSIC detector at Argonne National Laboratory [213]. Direct measurement of this reaction is particularly difficult due to a combination of positive Q-value (4.12 MeV) and low alpha-emission threshold in ^{20}Ne (E$_x$=4.73 MeV) [214]. In order to measure the branching ratio of ^{17}F(α,pγ)^{20}Ne or ^{20}Ne(g.s.) to ^{17}F(α,p)^{20}Ne$^* \rightarrow ^{16}$O+α, one needs to observe the decay of the ^{20}Ne along with the emitted proton, i.e. three-particle from same reaction vertex. The tracking ability of TPCs provide the required capabilities to study this reaction. ^{17}F(α,p)^{20}Ne

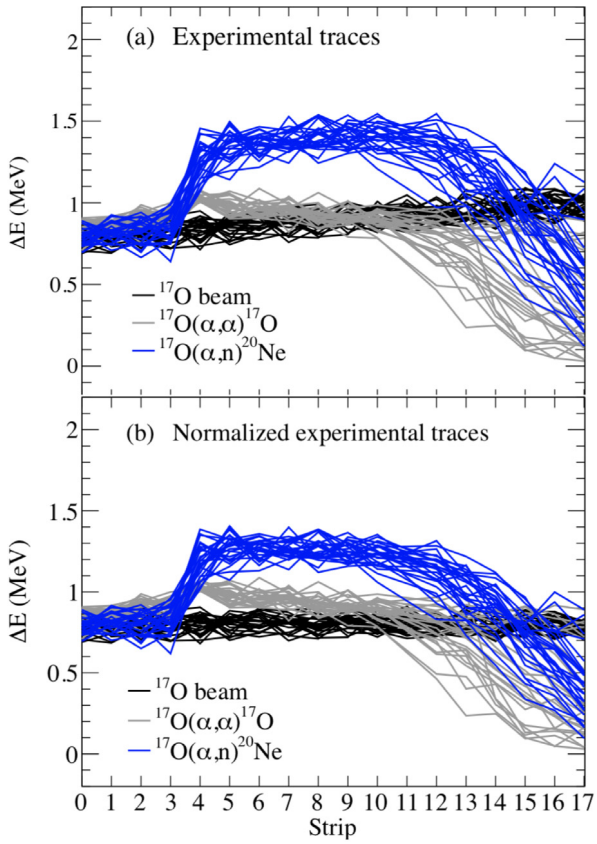

Fig. 37. Energy-loss signals measured in the MUSIC detector [14]. Distinction between the beam particle (^{17}O), scattered ^{17}O and reaction product ^{20}Ne can be clearly seen.

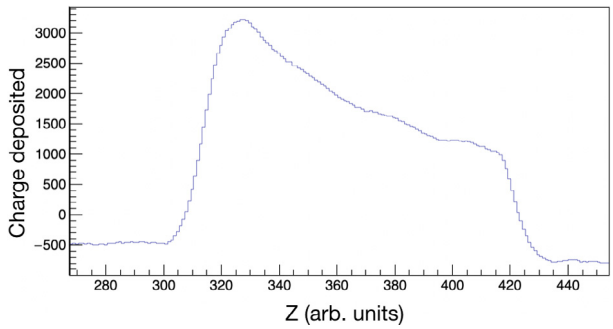

Fig. 38. An example event showing the charge deposition of beam along the beam axis of the AT-TPC.

has been recently measured with the pAT-TPC at the Twinsol facility, University of Notre Dame. For more information on Twinsol see [215]. The main progress in this experiment was the use of pure helium gas as a target and tracking medium. The use of pure helium was facilitated by the use of Multi-layer Thick Gas Electron Multipliers (M-THGEMs), which performs electron pre-amplification before the final stage avalanche in the micromegas and hence provides higher gain [216].

8.3. Beta-delayed proton emission to constrain reaction rates

Beta-delayed proton emission occurs when an unstable nucleus undergoes β-decay to a proton-unbound state, which promptly emits a proton. This phenomenon has been used to constrain astrophysical reaction rates. In these studies, the β-delayed proton emission feeds resonant states for which γ-decay and particle-decay branching is studied. The

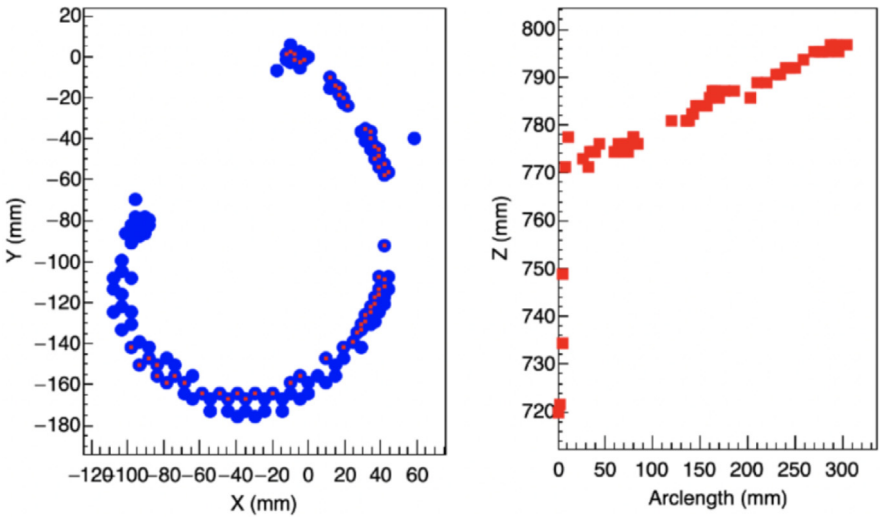

Fig. 39. The left panel shows the projection of a proton track on the pad plane where blue dots are data points and red indicates the data points chosen for RANSAC analysis. The right panel shows the arc length of each hit pattern point as a function of the z-coordinate.

observations provide the information on resonance strengths as well as resonance energies and help to constrain capture reaction rates e.g. (p, γ) or (α, γ). A classic example is the population of the 4.03 MeV state in ^{19}Ne via β-delayed proton emission of ^{20}Mg. This is the single most important resonance which dictates the ^{15}O(α, γ)^{19}Ne reaction rate [217]. In the absence of a direct measurement, indirect measurements focus on constraining the resonance strength which can be written as:

$$\omega\gamma = \frac{2\hbar}{\tau}\frac{\Gamma_\alpha}{\Gamma}(1-\frac{\Gamma_\alpha}{\Gamma}) \tag{16}$$

where τ is the level lifetime and Γ_α/Γ is the small α-particle branching ratio. The resonance strength remains uncertain as there is only an upper limit of 6×10^{-4} [218]. Recently, a first experimental evidence for the population of the 4.03 MeV state of ^{19}Ne via ^{20}Mg β-delayed proton emission was found [219]. In a relatively similar, but quite exotic phenomenon, β-delayed proton emission in ^{11}Be (a neutron-rich nucleus) has been observed using pAT-TPC [132]. Very low energy protons $\sim$ 200 keV were detected with a low branching ratio $\sim 10^{-5}$ (see Section 6.2 and Fig. 31). This recent experiment demonstrates the effectiveness of TPCs to measure β-delayed proton emission and will open up the possibilities to indirectly constrain the reaction rates using such measurements.

The GAseous Detector with GErmanium Tagging (GADGET), a detector dedicated to such studies, has been commissioned at NSCL [15]. Using GADGET, β-delayed proton emission from ^{23}Al has been recently measured to constrain the ^{22}Na(p, γ)^{23}Mg reaction rate [220]. ^{22}Na, predicted to be produced in classical novae, is a major gamma emitter and hence a target for astronomy searches. The yield of ^{22}Na is sensitive to it is destruction through ^{22}Na(p, γ)^{23}Mg and this reaction rate is dominated by a single resonance at the center-of-mass energy of 204 keV [221]. Two direct measurements of resonance strength for this resonance differs by more than a factor of 3, leading to factor of 2 variation in ^{22}Na yield in Novae [221,222]. The combination of measurements of the proton branching ratio of the resonance with its lifetime and spin also provides the resonance strength. Therefore, β-delayed proton decay in ^{23}Al has been previously studied using solid implantation detectors to constrain the resonance strength [223]. A new measurement with GADGET indicates that the resonance strength is a factor of 7 to 22 lower than the previous measurements. This large change was attributed to an overwhelming β-background in previous measurement(s) where the final spectrum relies heavily on the background model. GADGET provides substantial β-background suppression compared to solid implantation detectors as shown in Fig. 40. This new measurement will have serious implications for the destruction of ^{22}Na and hence the prospects for γ-ray detection from novae with space telescopes will be different.

8.4. Summary and outlook

Capture reactions are among the most dominant in a variety of astrophysical environments, from quiescent burning to explosive burning. Time-reverse measurements of capture reactions provide an advantage as the factor obtained from the reciprocity theorem provides a considerable improvement in the luminosity. These types of measurements need high intensity γ-ray beams impinging on stable targets. The major challenge is that reaction products in photo-induced reactions can have very low energy. The tracking capabilities of time projection chambers provide the required sensitivity to detect very low energy reaction products and hence make these detectors suitable for such measurements. In novae

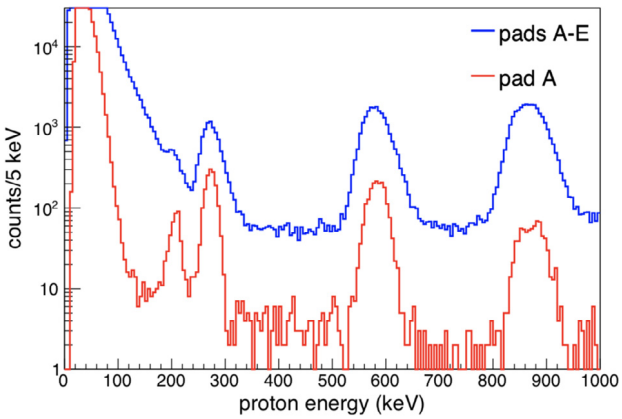

Fig. 40. An example proton spectrum using GADGET. The 204 keV proton peak is visible above background in both spectra. [220].

and X-ray bursts, (p, α) and (α,p) reactions are crucial for both energy generation and nucleosynthesis. Since the beam slows down as it goes through the target, active-target time projection chambers provide a full excitation function from a single beam energy. The use of pure gases (e.g. hydrogen and helium) helps in obtaining relatively background-free spectrum. Beta-delayed particle emission experiments using time projection chambers are pushing the sensitivity limits to very low branching ratios and low energies.

9. Direct reactions at higher energy

This last section departs from the preceding ones that regroup applications of active targets by physics theme. Here we cover various experimental ideas that could not fit in the previous sections, but are nonetheless worthy of being mentioned here, particularly because they make use of radioactive beams that are produced at high energy from projectile fragmentation. Although most applications of active-target time projection chambers in nuclear physics are concentrated on processes that involve beam energies close or slightly above the Coulomb barrier, some reactions conducted at much higher energies can in some cases take advantage of the benefits they offer. Some examples of such inverse kinematics reactions are given below, where the detection of the low energy recoil particle is paramount to the objectives of the experiment. In these examples, it is assumed that the high energy residue is able to escape the active volume, and can be subsequently collected and characterized by an additional detector such as a silicon telescope or magnetic spectrometer.

9.1. Charge-exchange reaction (d, ^{2}He)

Charge-exchange reactions have been used extensively to probe the Gamow–Teller strength in nuclei. Unlike β-decay, they offer the advantage of not being limited by the Q-value, and allow the exploration of GT strength at much higher energies. The relationship between the charge-exchange cross section at low momentum transfer and the GT strength has been well established [224], and is used in numerous nuclear structure and nuclear astrophysics applications. However, performing this type of reaction on radioactive beams in inverse kinematics is still a major experimental challenge. Although it has been performed in the β^- (or pn) direction using for instance cryogenic proton targets with some success (see for instance [225], it remains very difficult in the opposite β^+ (or np) direction due to the lack of neutron targets. Some attempts using complex nuclei such as in the (^{7}Li, ^{7}Be) reaction have had some success [226,227], but are limited to high intensity beams due to the required small target thickness and the need for γ-ray detection. The closest to a neutron target is deuterium, however the recoil from the charge-exchange reaction is ^{2}He, which is unbound and quickly decays into 2 protons. Nevertheless, the (d, ^{2}He) reaction is well established as a tool to extract GT strength in direct kinematics [228,229].

Because this reaction has to be performed at low momentum transfer, the energy of the emerging ^{2}He is very low (below a few MeV), before it breaks up into the 2 protons. For this reason, the use of an active target is a promising prospect since the two low energy protons can emerge from the beam region and be efficiently detected within the deuterium gas volume. The difficulty remains to extract the small charge-exchange cross section from other larger channels such as (d,d') or (d,p) for instance. For this particular reaction, the back-to-back emission of two protons in the rest frame of the ^{2}He particle, combined with the detection of the heavy residue of the projectile should provide a good criteria to select the charge-exchange events. Finally, the measurement of small cross sections such as the charge-exchange (on the order of a few mb/sr) requires higher beam intensities that will induce large amount of pile-up and saturation in the beam region of the active target. Several methods are available to avoid possible distortion of the electron drift field, including suppressing or even removing the electron amplification device part corresponding to the beam region. In an axial device such as the AT-TPC for instance, this can be realized by manufacturing a pad plane with a hole in its center that lets the high energy beam residues escape the active volume to be collected by another detector or a spectrometer.

9.2. Proton scattering

Nuclear matter radii can be efficiently probed via proton scattering at energies well above the Fermi level [230]. These reactions can probe the one-particle density and nucleon–nucleon potential inside nuclei via the analysis of differential cross sections as a function of momentum transfer. These parameters are directly related to the matter distributions in the nucleus, from which new phenomena such as the formation of haloes or neutron skins can be inferred. This type of reaction has seen a revival since the discovery of the halo phenomenon, but like other reactions covered in this review they have to be performed in inverse kinematics, which requires novel experimental techniques.

Many high energy proton scattering experiments performed in inverse kinematics take advantage of the large momentum of the incoming beam to boost the luminosity by using thick targets. The most recent results employ a liquid hydrogen target placed inside a γ-ray tracking detector array (see for instance [231] and references therein). However, this technique relies on the detection of γ-rays with their associated low efficiency, since the low energy recoil proton does not have enough energy to escape the target material.

The IKAR active-target detector [16] was specially developed to detect these low energy recoil protons while providing a thick proton target to keep the large luminosity. Filled with 10 bar of hydrogen gas, this original design is able to produce results with beam intensities as low as 6 kHz. Recent results obtained with a ^{12}Be beam [232] illustrate the use of this active target with quasi-free scattering reactions such as ^{12}Be(p,pn) as well.

An alternate method to perform this type of measurement was conducted via the use of a gas target inside a ring [233]. By taking advantage of recirculating the radioactive beam, the luminosity can be boosted by several orders of magnitudes. The experimental challenges associated with this method include the handling of a gas target in a high vacuum environment, the preservation of the beam emittance and the beam intensities necessary to achieve sufficient statistics. For instance, the pioneering experiment on ^{56}Ni(p,p) [233] used 3×10^6 particles per second, about 3 orders of magnitude larger than required for an active target. A large portion of the luminosity loss compared to active targets is due to the limited solid angle coverage that can be achieved.

9.3. Giant resonances

Giant resonances are highly collective excitations of nuclei where a large number of nucleons contribute coherently to an oscillatory motion. They are manifested as large maximums in the cross sections at excitation energies that are typically high above particle-emission thresholds and can be excited by collision with fast charged particles from 50 MeV/u to hundreds of MeV/u or even GeV/u. The giant resonances are typically decomposed using a multipole expansion and each multipole can give unique information on nuclear structure. The lowest and most prominent multipoles are the giant monopole (or compression mode) resonance, the giant isovector dipole resonance, and giant quadrupole resonance. For the study of each of these excitations, inelastic scattering is a useful tool and the precision measurement of cross sections in a particular angular range of scattered particles is needed. The importance of precise angle measurements can be seen in the multipole decomposition analysis that is shown in Fig. 41 for the three Pb isotopes, ^{204}Pb, ^{206}Pb, and ^{208}Pb, where the contributions of the $L = 0, 1, 2, 3$ components are fitted.

For the giant monopole resonance, the angular momentum transferred by the scattering particle is $L = 0$, which has a maximum cross section at 0°. The minimum for the monopole contribution is in the range of 1–2 degrees where the other multipoles have a maximum and are relatively slowly varying. Therefore, measuring the cross section around 0° is crucial for the multipole decomposition analysis. This presents a problem for studies of the giant monopole resonance in radioactive nuclei. For these nuclei, experiments require the use of inverse kinematics where in the laboratory frame, small angle scattering translates to scattering of the recoil particle near 90° with an energy approaching zero. Such particles are difficult to detect due to their low energies and very thin targets and low energy thresholds are required. Active targets allow for such a low-energy threshold as well as high geometric efficiency and for TPCs, the ability to precisely measure angles. An example is the CAT active-target detector [17] that has been developed specifically for detecting low-energy scattered particles from inelastic scattering using inverse kinematics.

9.4. Giant monopole resonance

The giant monopole resonance is also called breathing mode where is it interpreted as when the nucleus undergoes a uniform and oscillatory compression and expansion. The frequency (or energy) of this excitation is directly related to the compressibility of nuclear matter [234]. This has important implications for understanding the nuclear equation of state and dense matter in astrophysical systems. Answering questions related to the neutron star size and understanding the dynamics of neutron star mergers can be constrained by our understanding of nuclear matter [235]. One of the ways that the compressibility term in the nuclear equation of state can be determined is to measure the change in energy of the giant monopole resonance in a large isotopic chain. This inevitably requires the use of radioactive beams as one would like to measure the evolution of the giant resonance from the most proton-rich to the most neutron-rich nucleus.

One opportunity to do this is to study the Ni isotopic chain by using proton-rich and neutron-rich Ni beams at high energy with gas targets for proton, deuteron, and α scattering. Inelastic excitations using scattering require the use of a gas target at a pressure that will allow a sufficient track length and an amplification that is high enough to detect the primary

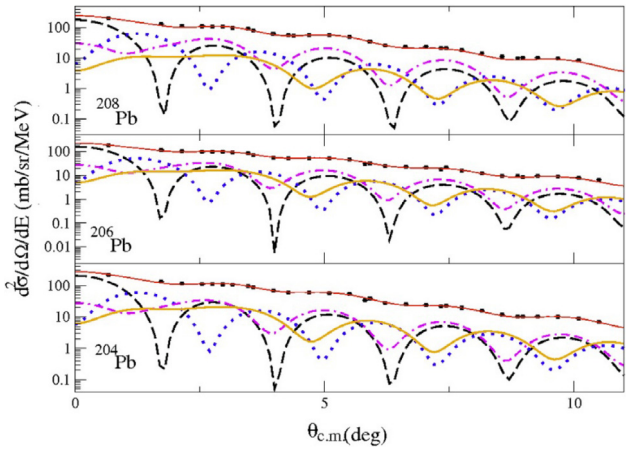

Fig. 41. Measured angular distributions for ^{204}Pb, ^{206}Pb, and ^{208}Pb are shown as well as the fit showing the multipole decomposition analysis for the $L = 0, 1, 2, 3$ contributions.
Source: Figure from Ref. [234].

ionization. By tuning the gas pressure, one can achieve a relatively low energy threshold for detection. For active target TPCs, the use of MPGDs such as Micromegas and GEMs can provide gains high enough to detect a robust signal. Pioneering measurements for Ni isotopes have been done using the MAYA active-target detector for ^{56}Ni [236] and ^{68}Ni [237] and measured elastically scattered deuterons and α particles, respectively. In both experiments, low-energy alpha particles were measured and angular distributions as a function of energy were deduced. The excitation function for all angles and for α particles scattered at 5.5° in the center-of-mass frame are shown in Fig. 42. The fit to the data was performed using a sum of Lorentzian peaks and their decomposition can also be seen in the figure. As particle identification and tracking algorithms improve with modern detectors, data with less background and higher statistics will be possible for similar giant resonance studies with proton and neutron-rich radioactive beams.

9.5. Summary and outlook

Similar experimental techniques using fast beams of nuclei from different mass regions combined with active target TPCs can open a window to precise measurements of inelastic α (or other light charged particles such as p, d, ^{3}He) at low scattering angles in the center-of-mass frame. No experiment using this technique has been performed yet, and the use of an active target is only warranted if the detection of the slow recoil is necessary. Many fast beam reactions in inverse kinematics bypass the detection of the slow recoil and rely instead on in-flight γ-ray detection from the escaping heavy residue to characterize the reaction. However, the possibility to detect the slow recoil without a significant loss in luminosity will enable more exclusive measurements and surely open new possibilities.

10. Conclusion

In this review we have presented the potential uses of time projection chambers in general and active-target time projection chambers in particular for low energy nuclear physics experiments. Although it does not attempt to be exhaustive, the variety of themes covered illustrates the versatility of active-target time projection chambers and the vast amount of physics applications that can take advantage of their potential 4π solid angle detection coverage and excellent resolution and separation of charged particle tracks. Thanks to this increased luminosity, this type of detector can be used to perform experiments with weak beam intensities, down to a few hundreds particles per second, therefore extending the reach of nuclear studies to more than a thousand exotic and rare isotopes that can only be produced at such low intensities. Their rapid development in low energy nuclear physics laboratories and facilities around the world is a testimony of their potential to drive new discoveries and push forward the limits of our knowledge of the nucleus.

Acknowledgments

This material is based upon work supported by the U.S. National Science Foundation under grant No. PHY-1565546 (NSCL) and PHY-1713857 (ND), and the U.S. Department of Energy, Office of Science, Office of Nuclear Physics under Contract No. DE-AC02-05CH11231 (LBNL).

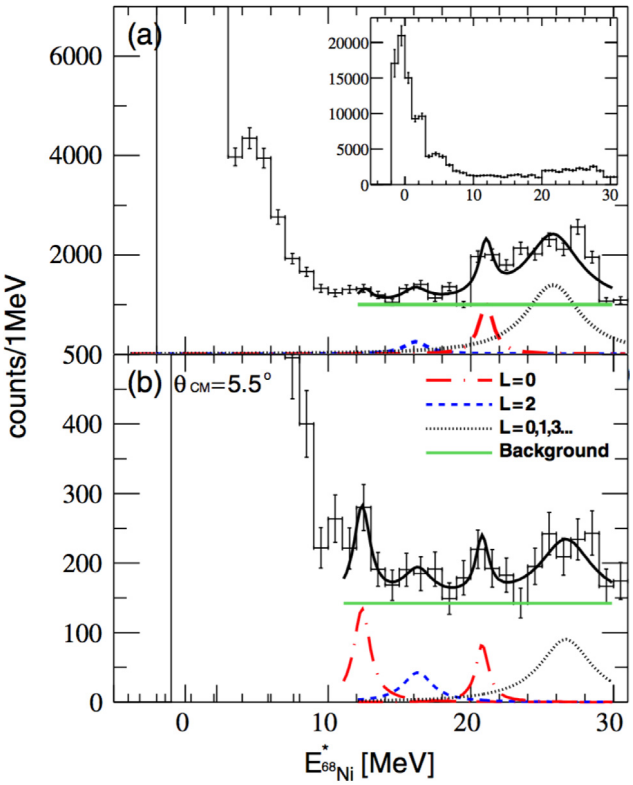

Fig. 42. The excitation function for α inelastic scattering in ^{68}Ni measured with the active-target detector MAYA is shown in the top figure (a). The angular data for scattering at 5.5° in the center-of-mass is shown in the bottom figure (b). Fits using a sum of Lorentzian peaks and a constant background are also shown.
Source: Figure from Ref. [237].

References

[1] S. Beceiro-Novo, T. Ahn, D. Bazin, W. Mittig, Prog. Part. Nucl. Phys. 84 (2015) 124–165.
[2] Y. Ayyad, D. Bazin, S. Beceiro-Novo, M. Cortesi, W. Mittig, The European Physical Journal A 54 (10) (2018) 181.
[3] D. Suzuki, M. Ford, D. Bazin, W. Mittig, W. Lynch, T. Ahn, S. Aune, E. Galyaev, A. Fritsch, J. Gilbert, F. Montes, A. Shore, J. Yurkon, J. Kolata, J. Browne, A. Howard, A. Roberts, X. Tang, Nucl. Instrum. Methods Phys. Res. A 691 (2012) 39–54.
[4] J. Bradt, D. Bazin, F. Abu-Nimeh, T. Ahn, Y. Ayyad, S. BeceiroNovo, L. Carpenter, M. Cortesi, M. Kuchera, W. Lynch, W. Mittig, S. Rost, N. Watwood, J. Yurkon, Nucl. Instrum. Methods Phys. Res. A 875 (2017) 65–79.
[5] R. Raabe, The SpecMAT active target, 2018, http://cds.cern.ch/record/2644039/files/INTC-M-020.pdf.
[6] C. Demonchy, W. Mittig, H. Savajols, P. Roussel-Chomaz, M. Chartier, B. Jurado, L. Giot, D. Cortina-Gil, M. Caamao, G. Ter-Arkopian, A. Fomichev, A. Rodin, M. Golovkov, S. Stepantsov, A. Gillibert, E. Pollacco, A. Obertelli, H. Wang, Nucl. Instrum. Methods Phys. Res. A 573 (1) (2007) 145–148, Proceedings of the 7th International Conference on Position-Sensitive Detectors.
[7] B. Mauss, P. Morfouace, T. Roger, J. Pancin, G. Grinyer, J. Giovinazzo, V. Alcindor, H. Álvarez-Pol, A. Arokiaraj, M. Babo, B. Bastin, C. Borcea, M.C. no, S. Ceruti, B. Fernández-Domínguez, E. Foulon-Moret, P. Gangnant, S. Giraud, A. Laffoley, G. Mantovani, T. Marchi, B. Monteagudo, J. Pibernat, O. Poleshchuk, R. Raabe, J. Refsgaard, A. Revel, F. Saillant, M. Stanoiu, G. Wittwer, J. Yang, Nucl. Instrum. Methods Phys. Res. A 940 (2019) 498–504.
[8] J. Bishop, G.V. Rogachev, E. Aboud, S. Ahn, M. Assunção, M. Barbui, A. Bosh, V. Guimarães, J. Hooker, C. Hunt, D. Jayatissa, E. Koshchiy, S. Lukyanov, R. O'Dwyer, Y. Penionzhkevich, E. Pollacco, C. Pruitt, B.T. Roeder, A. Saastamoinen, L. Sobotka, E. Uberseder, S. Upadhyayula, J. Zamora, J. Phys. Conf. Ser. 1308 (2019) 012006.
[9] T. Furuno, T. Kawabata, H. Ong, S. Adachi, Y. Ayyad, T. Baba, Y. Fujikawa, T. Hashimoto, K. Inaba, Y. Ishii, S. Kabuki, H. Kubo, Y. Matsuda, Y. Matsuoka, T. Mizumoto, T. Morimoto, M. Murata, T. Sawano, T. Suzuki, A. Takada, J. Tanaka, I. Tanihata, T. Tanimori, D. Tran, M. Tsumura, H. Watanabe, Nucl. Instrum. Methods Phys. Res. A 908 (2018) 215–224.
[10] B. Blank, L. Audirac, G. Canchel, F. Delalee, C. Demonchy, J. Giovinazzo, L. Hay, P. Hellmuth, J. Huikari, S. Leblanc, S. List, C. Marchand, I. Matea, J.-L. Pedroza, J. Pibernat, A. Rebii, L. Serani, F. de Oliveira Santos, S. Grévy, L. Perrot, C. Stodel, J. Thomas, C. Borcea, C. Dossat, R. de Oliveira, Nucl. Instrum. Methods Phys. Res. B 266 (19) (2008) 4606–4611, Proceedings of the XVth International Conference on Electromagnetic Isotope Separators and Techniques Related to their Applications.
[11] K. Miernik, W. Dominik, H. Czyrkowski, R. Dabrowski, A. Fomitchev, M. Golovkov, Z. Janas, W. Kuśmierz, M. Pftzner, A. Rodin, S. Stepantsov, R. Slepniev, G. Ter-Akopian, R. Wolski, Nucl. Instrum. Methods Phys. Res. A 581 (1) (2007) 194–197, VCI 2007.
[12] A. Chatillon, J. Taïeb, J.-F. Martin, E. Pellereau, G. Boutoux, T. Gorbinet, L. Grente, G. Bélier, B. Laurent, H. Alvarez-Pol, Y. Ayyad, J. Benlliure, M. Caamaño, L. Audouin, E. Casarejos, D. Cortina-Gil, F. Farget, B. Fernández-Domínguez, A. Heinz, B. Jurado, A. Keli´c-Heil, N. Kurz, S. Lindberg, B. Löher, C. Nociforo, C. Paradela, S. Pietri, D. Ramos, J.-L. Rodriguez-Sanchez, C. Rodrìguez-Tajes, D. Rossi, K.-H. Schmidt, H. Simon, L. Tassan-Got, H. Törnqvist, J. Vargas, B. Voss, H. Weick, Y. Yan, EPJ Web Conf. 111 (2016) 08001.

[13] M. Heffner, D. Asner, R. Baker, J. Baker, S. Barrett, C. Brune, J. Bundgaard, E. Burgett, D. Carter, M. Cunningham, J. Deaven, D. Duke, U. Greife, S. Grimes, U. Hager, N. Hertel, T. Hill, D. Isenhower, K. Jewell, J. King, J. Klay, V. Kleinrath, N. Kornilov, R. Kudo, A. Laptev, M. Leonard, W. Loveland, T. Massey, C. McGrath, R. Meharchand, L. Montoya, N. Pickle, H. Qu, V. Riot, J. Ruz, S. Sangiorgio, B. Seilhan, S. Sharma, L. Snyder, S. Stave, G. Tatishvili, R. Thornton, F. Tovesson, D. Towell, R. Towell, S. Watson, B. Wendt, L. Wood, L. Yao, Nucl. Instrum. Methods Phys. Res. A 759 (2014) 50–64.
[14] M. Avila, K. Rehm, S. Almaraz-Calderon, A. Ayangeakaa, C. Dickerson, C. Hoffman, C. Jiang, B. Kay, J. Lai, O. Nusair, R. Pardo, D. Santiago-Gonzalez, R. Talwar, C. Ugalde, Nucl. Instrum. Methods Phys. Res. A 859 (2017) 63–68.
[15] M. Friedman, D. Pérez-Loureiro, T. Budner, E. Pollacco, C. Wrede, M. Cortesi, C. Fry, B. Glassman, M. Harris, J. Heideman, M. Janasik, B. Roeder, M. Roosa, A. Saastamoinen, J. Stomps, J. Surbrook, P. Tiwari, J. Yurkon, Nucl. Instrum. Methods Phys. Res. A 940 (2019) 93–102.
[16] S. Neumaier, G. Alkhazov, M. Andronenko, A. Dobrovolsky, P. Egelhof, G. Gavrilov, H. Geissel, H. Irnich, A. Khanzadeev, G. Korolev, A. Lobodenko, G. Münzenberg, M. Mutterer, W. Schwab, D. Seliverstov, T. Suzuki, N. Timofeev, A. Vorobyov, Nuclear Phys. A 712 (3) (2002) 247–268.
[17] S. Ota, H. Tokieda, C.S. Lee, Y.N. Watanabe, J. Radioanal. Nucl. Chem. 305 (3) (2015) 907–911.
[18] D. Baye, P. Descouvemont, Scholarpedia 8 (1) (2013) 12360, revision #129959.
[19] A.M. Lane, R.G. Thomas, Rev. Modern Phys. 30 (1958) 257–353.
[20] R. Furnstahl, A. Schwenk, J. Phys. G: Nucl. Part. Phys. 37 (6) (2010) 064005.
[21] Y. Ayyad, W. Mittig, D. Bazin, S. Beceiro-Novo, M. Cortesi, Nucl. Instrum. Methods Phys. Res. A 880 (2018) 166–173.
[22] T. Roger, J. Pancin, G. Grinyer, B. Mauss, A. Laffoley, P. Rosier, H. Alvarez-Pol, M. Babo, B. Blank, M. Caamano, S. Ceruti, J. Daemen, S. Damoy, B. Duclos, B.F.-D. nguez, F. Flavigny, J. Giovinazzo, T. Goigoux, J. Henares, P. Konczykowski, T. Marchi, G. Lebertre, N. Lecesne, L. Legeard, C. Maugeais, G. Minier, B. Osmond, J. Pedroza, J. Pibernat, O. Poleshchuk, E. Pollacco, R. Raabe, B. Raine, F. Renzi, F. Saillant, P. Sénécal, P. Sizun, D. Suzuki, J. Swartz, C. Wouters, G. Wittwer, J. Yang, Nucl. Instrum. Methods Phys. Res. A 895 (2018) 126–134.
[23] M. Kuchera, R. Ramanujan, J. Taylor, R. Strauss, D. Bazin, J. Bradt, R. Chen, Nucl. Instrum. Methods Phys. Res. A 940 (2019) 156–167.
[24] O. Sorlin, M.-G. Porquet, Prog. Part. Nucl. Phys. 61 (2) (2008) 602–673.
[25] T. Otsuka, T. Suzuki, R. Fujimoto, H. Grawe, Y. Akaishi, Phys. Rev. Lett. 95 (2005) 232502.
[26] T. Otsuka, T. Suzuki, M. Honma, Y. Utsuno, N. Tsunoda, K. Tsukiyama, M. Hjorth-Jensen, Phys. Rev. Lett. 104 (2010) 012501.
[27] G. Hagen, M. Hjorth-Jensen, G.R. Jansen, R. Machleidt, T. Papenbrock, Phys. Rev. Lett. 108 (2012) 242501.
[28] O. Sorlin, M.-G. Porquet, Physica Scripta T152 (2013) 014003.
[29] D.J. Dean, M. Hjorth-Jensen, Computational Quantum Mechanics for Nuclear Physics, first ed., Chapman and Hall/CRC, 2017.
[30] W. Leidemann, G. Orlandini, Prog. Part. Nucl. Phys. 68 (2013) 158–214.
[31] A. Navin, D.W. Anthony, T. Aumann, T. Baumann, D. Bazin, Y. Blumenfeld, B.A. Brown, T. Glasmacher, P.G. Hansen, R.W. Ibbotson, P.A. Lofy, V. Maddalena, K. Miller, T. Nakamura, B.V. Pritychenko, B.M. Sherrill, E. Spears, M. Steiner, J.A. Tostevin, J. Yurkon, A. Wagner, Phys. Rev. Lett. 85 (2000) 266–269.
[32] A.O. Macchiavelli, H.L. Crawford, C.M. Campbell, R.M. Clark, M. Cromaz, P. Fallon, M.D. Jones, I.Y. Lee, A.L. Richard, M. Salathe, Phys. Rev. C 96 (2017) 054302.
[33] S.M. Lenzi, F. Nowacki, A. Poves, K. Sieja, Phys. Rev. C 82 (2010) 054301.
[34] F. Nowacki, A. Poves, E. Caurier, B. Bounthong, Phys. Rev. Lett. 117 (2016) 272501.
[35] R. Taniuchi, C. Santamaria, P. Doornenbal, A. Obertelli, K. Yoneda, G. Authelet, H. Baba, D. Calvet, F. Château, A. Corsi, A. Delbart, J.-M. Gheller, A. Gillibert, J.D. Holt, T. Isobe, V. Lapoux, M. Matsushita, J. Menéndez, S. Momiyama, T. Motobayashi, M. Niikura, F. Nowacki, K. Ogata, H. Otsu, T. Otsuka, C. Péron, S. Péru, A. Peyaud, E.C. Pollacco, A. Poves, J.-Y. Roussé, H. Sakurai, A. Schwenk, Y. Shiga, J. Simonis, S.R. Stroberg, S. Takeuchi, Y. Tsunoda, T. Uesaka, H. Wang, F. Browne, L.X. Chung, Z. Dombradi, S. Franchoo, F. Giacoppo, A. Gottardo, K. Hadynska-Klek, Z. Korkulu, S. Koyama, Y. Kubota, J. Lee, M. Lettmann, C. Louchart, R. Lozeva, K. Matsui, T. Miyazaki, S. Nishimura, L. Olivier, S. Ota, Z. Patel, E. Sahin, C. Shand, P.-A. Söderström, I. Stefan, D. Steppenbeck, T. Sumikama, D. Suzuki, Z. Vajta, V. Werner, J. Wu, Z.Y. Xu, Nature 569 (7754) (2019) 53–58.
[36] J.P. Schiffer, C.R. Hoffman, B.P. Kay, J.A. Clark, C.M. Deibel, S.J. Freeman, A.M. Howard, A.J. Mitchell, P.D. Parker, D.K. Sharp, J.S. Thomas, Phys. Rev. Lett. 108 (2012) 022501.
[37] B.P. Kay, J.P. Schiffer, S.J. Freeman, Phys. Rev. Lett. 111 (2013) 042502.
[38] J. Lighthall, B. Back, S. Baker, S. Freeman, H. Lee, B. Kay, S. Marley, K. Rehm, J. Rohrer, J. Schiffer, D. Shetty, A. Vann, J. Winkelbauer, A. Wuosmaa, Nucl. Instrum. Methods Phys. Res. A 622 (1) (2010) 97–106.
[39] A.H. Wuosmaa, B.B. Back, S. Baker, B.A. Brown, C.M. Deibel, P. Fallon, C.R. Hoffman, B.P. Kay, H.Y. Lee, J.C. Lighthall, A.O. Macchiavelli, S.T. Marley, R.C. Pardo, K.E. Rehm, J.P. Schiffer, D.V. Shetty, M. Wiedeking, Phys. Rev. Lett. 105 (2010) 132501.
[40] J. Chen, C.R. Hoffman, T. Ahn, K. Auranen, M.L. Avila, B.B. Back, D.W. Bardayan, D. Blankstein, P. Copp, D. Gorelov, B.P. Kay, S.A. Kuvin, J.P. Lai, D.G. McNeel, P.D. O'Malley, A.M. Rogers, D. Santiago-Gonzalez, J.P. Schiffer, J. Sethi, R. Talwar, J.R. Winkelbauer, Phys. Rev. C 98 (2018) 014325.
[41] D.Y. Pang, F.M. Nunes, A.M. Mukhamedzhanov, Phys. Rev. C 75 (2007) 024601.
[42] H.L. Scott, W. Galati, J.L. Weil, M.T. McEllistrem, Phys. Rev. 172 (1968) 1139–1148.
[43] S. Darmodjo, R.D. Alders, D.G. Martin, P. Dyer, S. Ali, S.A.A. Zaidi, Phys. Rev. C 4 (1971) 672–683.
[44] C.F. Moore, P. Richard, C.E. Watson, D. Robson, J.D. Fox, Phys. Rev. 141 (1966) 1166–1179.
[45] P. Richard, C.F. Moore, J.A. Becker, J.D. Fox, Phys. Rev. 145 (1966) 971–981.
[46] G. Vourvopoulos, J.D. Fox, Phys. Rev. 141 (1966) 1180–1184.
[47] J. Bradt, Y. Ayyad, D. Bazin, W. Mittig, T. Ahn, S.B. Novo, B. Brown, L. Carpenter, M. Cortesi, M. Kuchera, W. Lynch, S. Rost, N. Watwood, J. Yurkon, J. Barney, U. Datta, J. Estee, A. Gillibert, J. Manfredi, P. Morfouace, D. Pérez-Loureiro, E. Pollacco, J. Sammut, S. Sweany, Phys. Lett. B 778 (2018) 155–160.
[48] J. Hooker, G. Rogachev, V. Goldberg, E. Koshchiy, B. Roeder, H. Jayatissa, C. Hunt, C. Magana, S. Upadhyayula, E. Uberseder, A. Saastamoinen, Phys. Lett. B 769 (2017) 62–66.
[49] J. Hooker, G.V. Rogachev, E. Koshchiy, S. Ahn, M. Barbui, V.Z. Goldberg, C. Hunt, H. Jayatissa, E.C. Pollacco, B.T. Roeder, A. Saastamoinen, S. Upadhyayula, Phys. Rev. C 100 (2019) 054618.
[50] A. Bohr, B.R. Mottelson, D. Pines, Phys. Rev. 110 (1958) 936–938.
[51] S. Belyaev, Kgl. Danske Videnskab. Selskab. Mat.-Fys. Medd. 31 (1959).
[52] D. Brink, R. Broglia, Nuclear Superfluidity: Pairing in Finite Systems, in: Cambridge Monographs on Particle Physics, Nuclear Physics and Cosmology, Cambridge University Press, 2005.
[53] R. Broglia, V. Zelevinsky, Fifty Years of Nuclear BCS: Pairing in Finite Systems, World Scientific, 2013.
[54] D. Bes, R. Broglia, R. Perazzo, K. Kumar, Nuclear Phys. A 143 (1) (1970) 1–33.
[55] R.A. Broglia, O. Hansen, C. Riedel, in: M. Baranger, E. Vogt (Eds.), Advances in Nuclear Physics: Volume 6, Springer US, Boston, MA, 1973, pp. 287–457.
[56] A. Bohr, B. Mottelson, Nuclear Structure (In 2 Volumes), World Scientific Publishing Company, 1998.
[57] R.M. Clark, A.O. Macchiavelli, L. Fortunato, R. Krücken, Phys. Rev. Lett. 96 (2006) 032501.

[58] S. Yoshida, Nuclear Phys. 33 (1962) 685–692.
[59] J. Dobaczewski, N. Michel, W. Nazarewicz, M. Płoszajczak, J. Rotureau, Prog. Part. Nucl. Phys. 59 (1) (2007) 432–445, International Workshop on Nuclear Physics 28th Course.
[60] P. Hansen, A. Jensen, B. Jonson, Annu. Rev. Nucl. Part. Sci. 45 (1) (1995) 591–634.
[61] I. Tanihata, J. Phys. G: Nucl. Part. Phys. 22 (2) (1996) 157–198.
[62] H. Simon, D. Aleksandrov, T. Aumann, L. Axelsson, T. Baumann, M.J.G. Borge, L.V. Chulkov, R. Collatz, J. Cub, W. Dostal, B. Eberlein, T.W. Elze, H. Emling, H. Geissel, A. Grünschloss, M. Hellström, J. Holeczek, R. Holzmann, B. Jonson, J.V. Kratz, G. Kraus, R. Kulessa, Y. Leifels, A. Leistenschneider, T. Leth, I. Mukha, G. Münzenberg, F. Nickel, T. Nilsson, G. Nyman, B. Petersen, M. Pfützner, A. Richter, K. Riisager, C. Scheidenberger, G. Schrieder, W. Schwab, M.H. Smedberg, J. Stroth, A. Surowiec, O. Tengblad, M.V. Zhukov, Phys. Rev. Lett. 83 (1999) 496–499.
[63] F. Barranco, P. Bortignon, R. Broglia, G. Colò, E. Vigezzi, Eur. Phys. J. A 11 (4) (2001) 385–392.
[64] I. Tanihata, M. Alcorta, D. Bandyopadhyay, R. Bieri, L. Buchmann, B. Davids, N. Galinski, D. Howell, W. Mills, S. Mythili, R. Openshaw, E. Padilla-Rodal, G. Ruprecht, G. Sheffer, A.C. Shotter, M. Trinczek, P. Walden, H. Savajols, T. Roger, M. Caamano, W. Mittig, P. Roussel-Chomaz, R. Kanungo, A. Gallant, M. Notani, G. Savard, I.J. Thompson, Phys. Rev. Lett. 100 (2008) 192502.
[65] G. Potel, F. Barranco, E. Vigezzi, R.A. Broglia, Phys. Rev. Lett. 105 (2010) 172502.
[66] M. Matsuo, Phys. Rev. C 73 (2006) 044309.
[67] H. Shimoyama, M. Matsuo, Phys. Rev. C 84 (2011) 044317.
[68] G. Potel, F. Barranco, F. Marini, A. Idini, E. Vigezzi, R.A. Broglia, Phys. Rev. Lett. 107 (2011) 092501.
[69] S. Frauendorf, A.O. Macchiavelli, Prog. Part. Nucl. Phys. 78 (2014) 24–90.
[70] A.O. Macchiavelli, R.A. Broglia, V. Zelevinsky, Fifty Years of Nuclear BCS: Pairing in Finite Systems, World Scientific, 2013, p. 432.
[71] J. Engel, K. Langanke, P. Vogel, Phys. Lett. B 389 (2) (1996) 211–216.
[72] P.V. Isacker, D.D. Warner, A. Frank, Phys. Rev. Lett. 94 (2005) 162502.
[73] P. Frobrich, Phys. Lett. B 37 (4) (1971) 338–340.
[74] A. Macchiavelli, et al., ANL Physics Division 2002 Annual Report, ANL-03/23, page 21, and Report on the second EURISOL User Group Topical Meeting 1, Pag. 94, 2011.
[75] M. Assie, et al., Phys. Rev. Lett. (2019) submitted for publication.
[76] A. Gade, H. Iwasaki (Eds.), ReA Energy upgrade white paper, 2016, https://fribusers.org/documents/2016/ReAEnergyUpgradeWP.pdf.
[77] H. Barz, K. Hehl, C. Riedel, R. Broglia, Nuclear Phys. A 126 (3) (1969) 577–591.
[78] F. Donau, K. Hehl, C. Riedel, R. Broglia, P. Federman, Nuclear Phys. A 101 (3) (1967) 495–512.
[79] C. Thibault, R. Klapisch, C. Rigaud, A.M. Poskanzer, R. Prieels, L. Lessard, W. Reisdorf, Phys. Rev. C 12 (1975) 644–657.
[80] X. Campi, H. Flocard, A. Kerman, S. Koonin, Nuclear Phys. A 251 (2) (1975) 193–205.
[81] A. Poves, J. Retamosa, Phys. Lett. B 184 (4) (1987) 311–315.
[82] E.K. Warburton, J.A. Becker, B.A. Brown, Phys. Rev. C 41 (1990) 1147–1166.
[83] K. Wimmer, T. Kröll, R. Krücken, V. Bildstein, R. Gernhäuser, B. Bastin, N. Bree, J. Diriken, P. Van Duppen, M. Huyse, N. Patronis, P. Vermaelen, D. Voulot, J. Van de Walle, F. Wenander, L.M. Fraile, R. Chapman, B. Hadinia, R. Orlandi, J.F. Smith, R. Lutter, P.G. Thirolf, M. Labiche, A. Blazhev, M. Kalkühler, P. Reiter, M. Seidlitz, N. Warr, A.O. Macchiavelli, H.B. Jeppesen, E. Fiori, G. Georgiev, G. Schrieder, S. Das Gupta, G. Lo Bianco, S. Nardelli, J. Butterworth, J. Johansen, K. Riisager, Phys. Rev. Lett. 105 (2010) 252501.
[84] H.T. Fortune, Phys. Rev. C 84 (2011) 024327.
[85] J.A. Lay, L. Fortunato, A. Vitturi, Phys. Rev. C 89 (2014) 034618.
[86] A.O. Macchiavelli, H.L. Crawford, C.M. Campbell, R.M. Clark, M. Cromaz, P. Fallon, M.D. Jones, I.Y. Lee, M. Salathe, B.A. Brown, A. Poves, Phys. Rev. C 94 (2016) 051303.
[87] Y. Ayyad, N. Abgrall, T. Ahn, H. Álvarez-Pol, D. Bazin, S. Beceiro-Novo, L. Carpenter, R. Cooper, M. Cortesi, A. Macchiavelli, W. Mittig, B. Olaizola, J. Randhawa, C. Santamaria, N. Watwood, J. Zamora, R. Zegers, Nucl. Instrum. Methods Phys. Res. A 954 (2020) 161341, Symposium on Radiation Measurements and Applications XVII.
[88] H.L. Crawford, P. Fallon, A.O. Macchiavelli, P. Doornenbal, N. Aoi, F. Browne, C.M. Campbell, S. Chen, R.M. Clark, M.L. Cortés, M. Cromaz, E. Ideguchi, M.D. Jones, R. Kanungo, M. MacCormick, S. Momiyama, I. Murray, M. Niikura, S. Paschalis, M. Petri, H. Sakurai, M. Salathe, P. Schrock, D. Steppenbeck, S. Takeuchi, Y.K. Tanaka, R. Taniuchi, H. Wang, K. Wimmer, Phys. Rev. Lett. 122 (2019) 052501.
[89] W. von Oertzen, A. Vitturi, Rep. Progr. Phys. 64 (10) (2001) 1247–1337.
[90] M. Freer, H. Horiuchi, Y. Kanada-En'yo, D. Lee, U.-G. Meißner, Rev. Modern Phys. 90 (2018) 035004.
[91] W. Von Oertzen, M. Freer, Y. Kanada Enyo, Phys. Rep. 432 (2) (2006) 43–113.
[92] M. Freer, Rep. Progr. Phys. 70 (12) (2007) 2149–2210.
[93] H. Horiuchi, K. Ikeda, K. Kat, Progr. Theoret. Phys. Suppl. 192 (2012) 1–238.
[94] Y. Funaki, H. Horiuchi, A. Tohsaki, Prog. Part. Nucl. Phys. 82 (2015) 78–132.
[95] B. Schmookler, M. Duer, A. Schmidt, O. Hen, S. Gilad, E. Piasetzky, M. Strikman, L.B. Weinstein, S. Adhikari, M. Amaryan, A. Ashkenazi, H. Avakian, J. Ball, I. Balossino, L. Barion, M. Bashkanov, M. Battaglieri, A. Beck, I. Bedlinskiy, A.S. Biselli, S. Boiarinov, W.J. Briscoe, W.K. Brooks, V.D. Burkert, D.S. Carman, A. Celentano, G. Charles, T. Chetry, G. Ciullo, E. Cohen, P.L. Cole, V. Crede, R. Cruz-Torres, A. D'Angelo, N. Dashyan, E. De Sanctis, R. De Vita, A. Deur, S. Diehl, C. Djalali, R. Dupre, H. Egiyan, L. El Fassi, L. Elouadrhiri, P. Eugenio, G. Fedotov, R. Fersch, A. Filippi, T.A. Forest, G. Gavalian, G.P. Gilfoyle, F.X. Girod, E. Golovatch, R.W. Gothe, K.A. Griffioen, M. Guidal, L. Guo, K. Hafidi, H. Hakobyan, C. Hanretty, N. Harrison, F. Hauenstein, T.B. Hayward, K. Hicks, D. Higinbotham, M. Holtrop, C.E. Hyde, Y. Ilieva, D.G. Ireland, B.S. Ishkhanov, E.L. Isupov, H.S. Jo, S. Johnston, K. Joo, S. Joosten, M.L. Kabir, D. Keller, G. Khachatryan, M. Khachatryan, M. Khandaker, A. Kim, W. Kim, A. Klein, F.J. Klein, I. Korover, V. Kubarovsky, S.E. Kuhn, S.V. Kuleshov, L. Lanza, G. Laskaris, P. Lenisa, K. Livingston, I.J. MacGregor, N. Markov, B. McKinnon, S.M.T. Beck, T. Mineeva, M. Mirazita, V. Mokeev, R.A. Montgomery, C. Munoz Camacho, B. Mustapha, S. Niccolai, M. Osipenko, A.I. Ostrovidov, M. Paolone, R. Paremuzyan, K. Park, E. Pasyuk, M. Patsyuk, O. Pogorelko, J.W. Price, Y. Prok, D. Protopopescu, M. Ripani, D. Riser, A. Rizzo, G. Rosner, P. Rossi, F. Sabatié, C. Salgado, R.A. Schumacher, E.P. Segarra, Y.G. Sharabian, I.U. Skorodumina, D. Sokhan, N. Sparveris, S. Stepanyan, S. Strauch, M. Taiuti, J.A. Tan, M. Ungaro, H. Voskanyan, E. Voutier, D.P. Watts, X. Wei, M. Wood, N. Zachariou, J. Zhang, Z.W. Zhao, X. Zheng, Nature 566 (7744) (2019) 354–358.
[96] L.B. Weinstein, E. Piasetzky, D.W. Higinbotham, J. Gomez, O. Hen, R. Shneor, Phys. Rev. Lett. 106 (2011) 052301.
[97] J. Seely, A. Daniel, D. Gaskell, J. Arrington, N. Fomin, P. Solvignon, R. Asaturyan, F. Benmokhtar, W. Boeglin, B. Boillat, P. Bosted, A. Bruell, M.H.S. Bukhari, M.E. Christy, B. Clasie, S. Connell, M.M. Dalton, D. Day, J. Dunne, D. Dutta, L. El Fassi, R. Ent, H. Fenker, B.W. Filippone, H. Gao, C. Hill, R.J. Holt, T. Horn, E. Hungerford, M.K. Jones, J. Jourdan, N. Kalantarians, C.E. Keppel, D. Kiselev, M. Kotulla, C. Lee, A.F. Lung, S. Malace, D.G. Meekins, T. Mertens, H. Mkrtchyan, T. Navasardyan, G. Niculescu, I. Niculescu, H. Nomura, Y. Okayasu, A.K. Opper, C. Perdrisat, D.H. Potterveld, V. Punjabi, X. Qian, P.E. Reimer, J. Roche, V.M. Rodriguez, O. Rondon, E. Schulte, E. Segbefia, K. Slifer, G.R. Smith, V. Tadevosyan, S. Tajima, L. Tang, G. Testa, R. Trojer, V. Tvaskis, W.F. Vulcan, F.R. Wesselmann, S.A. Wood, J. Wright, L. Yuan, X. Zheng, Phys. Rev. Lett. 103 (2009) 202301.

[98] N. Fomin, J. Arrington, R. Asaturyan, F. Benmokhtar, W. Boeglin, P. Bosted, A. Bruell, M.H.S. Bukhari, M.E. Christy, E. Chudakov, B. Clasie, S.H. Connell, M.M. Dalton, A. Daniel, D.B. Day, D. Dutta, R. Ent, L. El Fassi, H. Fenker, B.W. Filippone, K. Garrow, D. Gaskell, C. Hill, R.J. Holt, T. Horn, M.K. Jones, J. Jourdan, N. Kalantarians, C.E. Keppel, D. Kiselev, M. Kotulla, R. Lindgren, A.F. Lung, S. Malace, P. Markowitz, P. McKee, D.G. Meekins, H. Mkrtchyan, T. Navasardyan, G. Niculescu, A.K. Opper, C. Perdrisat, D.H. Potterveld, V. Punjabi, X. Qian, P.E. Reimer, J. Roche, V.M. Rodriguez, O. Rondon, E. Schulte, J. Seely, E. Segbefia, K. Slifer, G.R. Smith, P. Solvignon, V. Tadevosyan, S. Tajima, L. Tang, G. Testa, R. Trojer, V. Tvaskis, W.F. Vulcan, C. Wasko, F.R. Wesselmann, S.A. Wood, J. Wright, X. Zheng, Phys. Rev. Lett. 108 (2012) 092502.
[99] B.R. Barrett, P. Navrátil, J.P. Vary, Prog. Part. Nucl. Phys. 69 (2013) 131–181.
[100] R.B. Wiringa, S.C. Pieper, J. Carlson, V.R. Pandharipande, Phys. Rev. C 62 (1) (2000) 014001.
[101] E. Epelbaum, H. Krebs, D. Lee, U.-G. Meissner, Phys. Rev. Lett. 106 (19) (2011) 192501.
[102] A.C. Dreyfuss, K.D. Launey, T. Dytrych, J.P. Draayer, R.B. Baker, C.M. Deibel, C. Bahri, Phys. Rev. C 95 (4) (2017) 044312.
[103] Y. Kanada-En'yo, H. Horiuchi, Progr. Theoret. Phys. Suppl. 142 (142) (2001) 205–263.
[104] H. Feldmeier, J. Schnack, Rev. Modern Phys. 72 (3) (2000) 655–688.
[105] T. Baba, M. Kimura, Phys. Rev. C 94 (4) (2016) 044303.
[106] M. Norrby, M. Brenner, T. LÖnnroth, K.M. KÄllman, Int. J. Mod. Phys. E 17 (10) (2008) 2025–2028.
[107] H. Horiuchi, K. Ikeda, Y. Suzuki, Suppl. Prog. Theor. Phys. 52 (1972) 89.
[108] M. Wiescher, T. Ahn, Nucl. Part. Correl. Clust. Phys. (2017) 203–255.
[109] A. Doté, H. Horiuchi, Y. Kanada-En'yo, Phys. Rev. C 56 (1997) 1844–1854.
[110] D. Suzuki, A. Shore, W. Mittig, J.J. Kolata, D. Bazin, M. Ford, T. Ahn, F.D. Becchetti, S. Beceiro Novo, D. Ben Ali, B. Bucher, J. Browne, X. Fang, M. Febbraro, A. Fritsch, E. Galyaev, A.M. Howard, N. Keeley, W.G. Lynch, M. Ojaruega, A.L. Roberts, X.D. Tang, Phys. Rev. C 87 (2013) 054301.
[111] T. Furuno, T. Kawabata, S. Adachi, Y. Ayyad, Y. Kanada-En'yo, Y. Fujikawa, K. Inaba, M. Murata, H.J. Ong, M. Sferrazza, Y. Takahashi, T. Takeda, I. Tanihata, D.T. Tran, M. Tsumura, Phys. Rev. C 100 (2019) 054322.
[112] T. Suhara, Y. Kanada-En'yo, Phys. Rev. C 82 (4) (2010) 044301.
[113] T. Baba, M. Kimura, Phys. Rev. C 99 (2) (2019) 021303.
[114] M. Freer, J.D. Malcolm, N.L. Achouri, N.I. Ashwood, D.W. Bardayan, S.M. Brown, W.N. Catford, K.A. Chipps, J. Cizewski, N. Curtis, K.L. Jones, T. Munoz-Britton, S.D. Pain, N. Soić, C. Wheldon, G.L. Wilson, V.A. Ziman, Phys. Rev. C 90 (2014) 054324.
[115] A. Fritsch, S. Beceiro-Novo, D. Suzuki, W. Mittig, J.J. Kolata, T. Ahn, D. Bazin, F.D. Becchetti, B. Bucher, Z. Chajecki, X. Fang, M. Febbraro, A.M. Howard, Y. Kanada-En'yo, W.G. Lynch, A.J. Mitchell, M. Ojaruega, A.M. Rogers, A. Shore, T. Suhara, X.D. Tang, R. Torres-Isea, H. Wang, Phys. Rev. C 93 (2016) 014321.
[116] H. Yamaguchi, D. Kahl, S. Hayakawa, Y. Sakaguchi, K. Abe, T. Nakao, T. Suhara, N. Iwasa, A. Kim, D. Kim, S. Cha, M. Kwag, J. Lee, E. Lee, K. Chae, Y. Wakabayashi, N. Imai, N. Kitamura, P. Lee, J. Moon, K. Lee, C. Akers, H. Jung, N. Duy, L. Khiem, C. Lee, Phys. Lett. B 766 (2017) 11–16.
[117] L. Carpenter, Cluster Structure and Three-Body Decay of ^{14}C (Ph.D. thesis), Michigan State University, 2019.
[118] R.J. deBoer, J. Görres, M. Wiescher, R.E. Azuma, A. Best, C.R. Brune, C.E. Fields, S. Jones, M. Pignatari, D. Sayre, K. Smith, F.X. Timmes, E. Uberseder, Rev. Modern Phys. 89 (2017) 035007.
[119] J.-P. Ebran, E. Khan, T. Nikšić, D. Vretenar, Nature 487 (7407) (2012) 341–344.
[120] K.D. Launey, A.C. Dreyfuss, J.P. Draayer, T. Dytrych, R. Baker, J. Phys. Conf. Ser. 569 (1) (2014).
[121] J.-P. Ebran, E. Khan, T. Nikšć, D. Vretenar, Phys. Rev. C 90 (2014) 054329.
[122] G.V. Rogachev, V.Z. Goldberg, T. Lönnroth, W.H. Trzaska, S.A. Fayans, K.-M. Källman, J.J. Kolata, M. Mutterer, M.V. Rozhkov, B.B. Skorodumov, Phys. Rev. C 64 (5) (2001) 051302.
[123] V.Z. Goldberg, G.V. Rogachev, W.H. Trzaska, J.J. Kolata, A. Andreyev, C. Angulo, M.J.G. Borge, S. Cherubini, G. Chubarian, G. Crowley, P. Van Duppen, M. Gorska, M. Gulino, M. Huyse, P. Jesinger, K.-M. Källman, M. Lattuada, T. Lönnroth, M. Mutterer, R. Raabe, S. Romano, M.V. Rozhkov, B.B. Skorodumov, C. Spitaleri, O. Tengblad, A. Tumino, Phys. Rev. C 69 (2) (2004) 024602.
[124] R. Talwar, T. Adachi, G.P.A. Berg, L. Bin, S. Bisterzo, M. Couder, R.J. deBoer, X. Fang, H. Fujita, Y. Fujita, J. Görres, K. Hatanaka, T. Itoh, T. Kadoya, A. Long, K. Miki, D. Patel, M. Pignatari, Y. Shimbara, A. Tamii, M. Wiescher, T. Yamamoto, M. Yosoi, Phys. Rev. C 93 (2016) 055803.
[125] B. Blank, M. Borge, Prog. Part. Nucl. Phys. 60 (2) (2008) 403–483.
[126] M.J.G. Borge, Phys. Scr. T 152 (2013) 014013.
[127] M. Pfützner, Phys. Scr. T 152 (2013) 014014.
[128] B. Blank, M. Płoszajczak, Rep. Progr. Phys. 71 (4) (2008) 046301.
[129] M. Pfützner, M. Karny, L.V. Grigorenko, K. Riisager, Rev. Modern Phys. 84 (2012) 567–619.
[130] D. Anthony, L. Buchmann, P. Bergbusch, J.M. D'Auria, M. Dombsky, U. Giesen, K.P. Jackson, J.D. King, J. Powell, F.C. Barker, Phys. Rev. C 65 (2002) 034310.
[131] R. Raabe, A. Andreyev, M.J.G. Borge, L. Buchmann, P. Capel, H.O.U. Fynbo, M. Huyse, R. Kanungo, T. Kirchner, C. Mattoon, A.C. Morton, I. Mukha, J. Pearson, J. Ponsaers, J.J. Ressler, K. Riisager, C. Ruiz, G. Ruprecht, F. Sarazin, O. Tengblad, P. Van Duppen, P. Walden, Phys. Rev. Lett. 101 (2008) 212501.
[132] Y. Ayyad, B. Olaizola, W. Mittig, G. Potel, V. Zelevinsky, M. Horoi, S. Beceiro-Novo, M. Alcorta, C. Andreoiu, T. Ahn, M. Anholm, L. Atar, A. Babu, D. Bazin, N. Bernier, S.S. Bhattacharjee, M. Bowry, R. Caballero-Folch, M. Cortesi, C. Dalitz, E. Dunling, A.B. Garnsworthy, M. Holl, B. Kootte, K.G. Leach, J.S. Randhawa, Y. Saito, C. Santamaria, P. Šiurytė, C.E. Svensson, R. Umashankar, N. Watwood, D. Yates, Phys. Rev. Lett. 123 (2019) 082501.
[133] B. Pfeiffer, K.-L. Kratz, M. Peter, Prog. Nucl. Energy 41 (1) (2002) 39–69.
[134] L.V. Grigorenko, M.V. Zhukov, Phys. Rev. C 76 (2007) 014008.
[135] R. Barton, R. McPherson, R.E. Bell, W.R. Frisken, W.T. Link, R.B. Moore, Can. J. Phys. 41 (12) (1963) 2007–2025.
[136] B. Blank, F. Boué, S. Andriamonje, S. Czajkowski, R.D. Moral, J. Dufour, A. Fleury, P. Pourre, M. Pravikoff, N. Orr, K.-H. Schmidt, E. Hanelt, Nuclear Phys. A 615 (1) (1997) 52–68.
[137] L. Axelsson, J. yst, M. Borge, L. Fraile, H. Fynbo, A. Honkanen, P. Hornshj, A. Jokinen, B. Jonson, P. Lipas, I. Martel, I. Mukha, T. Nilsson, G. Nyman, B. Petersen, K. Riisager, M. Smedberg, O. Tengblad, Nuclear Phys. A 634 (4) (1998) 475–496.
[138] J. Giovinazzo, B. Blank, C. Borcea, G. Canchel, J.-C. Dalouzy, C.E. Demonchy, F. de Oliveira Santos, C. Dossat, S. Grévy, L. Hay, J. Huikari, S. Leblanc, I. Matea, J.-L. Pedroza, L. Perrot, J. Pibernat, L. Serani, C. Stodel, J.-C. Thomas, Phys. Rev. Lett. 99 (2007) 102501.
[139] L. Audirac, P. Ascher, B. Blank, C. Borcea, B.A. Brown, G. Canchel, C.E. Demonchy, F. de Oliveira Santos, C. Dossat, J. Giovinazzo, S. Grévy, L. Hay, J. Huikari, S. Leblanc, I. Matea, J.L. Pedroza, L. Perrot, J. Pibernat, L. Serani, C. Stodel, J.C. Thomas, Eur. Phys. J. A 48 (12) (2012) 179.
[140] M. Pomorski, K. Miernik, W. Dominik, Z. Janas, M. Pfützner, C.R. Bingham, H. Czyrkowski, M. Ćwiok, I.G. Darby, R. Dabrowski, T. Ginter, R. Grzywacz, M. Karny, A. Korgul, W. Kuśmierz, S.N. Liddick, M. Rajabali, K. Rykaczewski, A. Stolz, Phys. Rev. C 83 (2011) 014306.
[141] C. Dossat, N. Adimi, F. Aksouh, F. Becker, A. Bey, B. Blank, C. Borcea, R. Borcea, A. Boston, M. Caamano, G. Canchel, M. Chartier, D. Cortina, S. Czajkowski, G. de France, F. de Oliveira Santos, A. Fleury, G. Georgiev, J. Giovinazzo, S. Grévy, R. Grzywacz, M. Hellström, M. Honma, Z. Janas, D. Karamanis, J. Kurcewicz, M. Lewitowicz, M.L. Jiménez, C. Mazzocchi, I. Matea, V. Maslov, P. Mayet, C. Moore, Nuclear Phys. A 792 (1) (2007) 18–86.

[142] K. Miernik, W. Dominik, Z. Janas, M. Pfützner, C.R. Bingham, H. Czyrkowski, M. Ćwiok, I.G. Darby, R. Dabrowski, T. Ginter, R. Grzywacz, M. Karny, A. Korgul, W. Kuśmierz, S.N. Liddick, M. Rajabali, K. Rykaczewski, A. Stolz, Phys. Rev. C 76 (2007) 041304.
[143] A.A. Lis, C. Mazzocchi, W. Dominik, Z. Janas, M. Pfützner, M. Pomorski, L. Acosta, S. Baraeva, E. Casarejos, J. Duénas-Díaz, V. Dunin, J.M. Espino, A. Estrade, F. Farinon, A. Fomichev, H. Geissel, A. Gorshkov, G. Kamiński, O. Kiselev, R. Knöbel, S. Krupko, M. Kuich, Y.A. Litvinov, G. Marquinez-Durán, I. Martel, I. Mukha, C. Nociforo, A.K. Ordúz, S. Pietri, A. Prochazka, A.M. Sánchez-Benítez, H. Simon, B. Sitar, R. Slepnev, M. Stanoiu, P. Strmen, I. Szarka, M. Takechi, Y. Tanaka, H. Weick, J.S. Winfield, Phys. Rev. C 91 (2015) 064309.
[144] M. Pomorski, M. Pfützner, W. Dominik, R. Grzywacz, A. Stolz, T. Baumann, J.S. Berryman, H. Czyrkowski, R. Dabrowski, A. Fijałkowska, T. Ginter, J. Johnson, G. Kamiński, N. Larson, S.N. Liddick, M. Madurga, C. Mazzocchi, S. Mianowski, K. Miernik, D. Miller, S. Paulauskas, J. Pereira, K.P. Rykaczewski, S. Suchyta, Phys. Rev. C 90 (2014) 014311.
[145] L. Janiak, N. Sokołowska, A.A. Bezbakh, A.A. Ciemny, H. Czyrkowski, R. Dabrowski, W. Dominik, A.S. Fomichev, M.S. Golovkov, A.V. Gorshkov, Z. Janas, G. Kamiński, A.G. Knyazev, S.A. Krupko, M. Kuich, C. Mazzocchi, M. Mentel, M. Pfützner, P. Pluciński, M. Pomorski, R.S. Slepniev, B. Zalewski, Phys. Rev. C 95 (2017) 034315.
[146] G. Canchel, L. Achouri, J. Äystö, R. Béraud, B. Blank, E. Chabanat, S. Czajkowski, P. Dendooven, A. Emsallem, J. Giovinazzo, J. Honkanen, A. Jokinen, M. Lewitowicz, C. Longour, F. de Oliviera Santos, K. Peräjärvi, M. Staniou, J. Thomas, The European Physical Journal A - Hadrons and Nuclei 12 (4) (2001) 377–380.
[147] M. Pfützner, W. Dominik, Z. Janas, C. Mazzocchi, M. Pomorski, A.A. Bezbakh, M.J.G. Borge, K. Chrapkiewicz, V. Chudoba, R. Frederickx, G. Kamiński, M. Kowalska, S. Krupko, M. Kuich, J. Kurcewicz, A.A. Lis, M.V. Lund, K. Miernik, J. Perkowski, R. Raabe, G. Randisi, K. Riisager, S. Sambi, O. Tengblad, F. Wenander, Phys. Rev. C 92 (2015) 014316.
[148] R. Raabe, J. Büscher, J. Ponsaers, F. Aksouh, M. Huyse, O. Ivanov, S.R. Lesher, I. Mukha, D. Pauwels, M. Sawicka, D. Smirnov, I. Stefanescu, J. Van de Walle, P. Van Duppen, C. Angulo, J. Cabrera, N. de Séréville, I. Martel, A.M. Sánchez-Benítez, C.A. Diget, Phys. Rev. C 80 (2009) 054307.
[149] E.M. Tursunov, D. Baye, P. Descouvemont, Phys. Rev. C 73 (2006) 014303.
[150] M. Pfützner, K. Riisager, Phys. Rev. C 97 (2018) 042501.
[151] B. Fornal, B. Grinstein, Phys. Rev. Lett. 120 (2018) 191801.
[152] D. McKeen, A.E. Nelson, S. Reddy, D. Zhou, Phys. Rev. Lett. 121 (2018) 061802.
[153] T.F. Motta, P.A.M. Guichon, A.W. Thomas, J. Phys. G: Nucl. Part. Phys. 45 (5) (2018) 05LT01.
[154] G. Baym, D.H. Beck, P. Geltenbort, J. Shelton, Phys. Rev. Lett. 121 (2018) 061801.
[155] A. Czarnecki, W.J. Marciano, A. Sirlin, Phys. Rev. Lett. 120 (2018) 202002.
[156] D. Dubbers, H. Saul, B. Märkisch, T. Soldner, H. Abele, Phys. Lett. B 791 (2019) 6–10.
[157] K. Riisager, O. Forstner, M. Borge, J. Briz, M. Carmona-Gallardo, L. Fraile, H. Fynbo, T. Giles, A. Gottberg, A. Heinz, J. Johansen, B. Jonson, J. Kurcewicz, M. Lund, T. Nilsson, G. Nyman, E. Rapisarda, P. Steier, O. Tengblad, R. Thies, S. Winkler, Phys. Lett. B 732 (2014) 305–308.
[158] Y. Ayyad, B. Olaizola, W. Mittig, G. Potel, V. Zelevinsky, M. Horoi, S. Beceiro-Novo, M. Alcorta, C. Andreoiu, T. Ahn, M. Anholm, L. Atar, A. Babu, D. Bazin, N. Bernier, S.S. Bhattacharjee, M. Bowry, R. Caballero-Folch, M. Cortesi, C. Dalitz, E. Dunling, A.B. Garnsworthy, M. Holl, B. Kootte, K.G. Leach, J.S. Randhawa, Y. Saito, C. Santamaria, P. Šiurytė, C.E. Svensson, R. Umashankar, N. Watwood, D. Yates, Phys. Rev. Lett. 123 (2019) 082501.
[159] J. Okołowicz, M. Płoszajczak, W. Nazarewicz, Phys. Rev. Lett. 124 (2020) 042502.
[160] N. Sokołowska, β-Delayed proton emission from ^{11}Be, 2019, https://people.nscl.msu.edu/%7Ebrown/procon-2019/procon-talks/Sokolowska-procon_web.pdf.
[161] J. Giovinazzo, B. Blank, M. Chartier, S. Czajkowski, A. Fleury, M.J. Lopez Jimenez, M.S. Pravikoff, J.-C. Thomas, F. de Oliveira Santos, M. Lewitowicz, V. Maslov, M. Stanoiu, R. Grzywacz, M. Pfützner, C. Borcea, B.A. Brown, Phys. Rev. Lett. 89 (2002) 102501.
[162] M. Pfützner, E. Badura, C. Bingham, B. Blank, M. Chartier, H. Geissel, J. Giovinazzo, L. Grigorenko, R. Grzywacz, M. Hellström, Z. Janas, J. Kurcewicz, A. Lalleman, C. Mazzocchi, I. Mukha, G. Münzenberg, C. Plettner, E. Roeckl, K. Rykaczewski, K. Schmidt, R. Simon, M. Stanoiu, J.-C. Thomas, Eur. Phys. J. A 14 (3) (2002) 279–285.
[163] C. Dossat, A. Bey, B. Blank, G. Canchel, A. Fleury, J. Giovinazzo, I. Matea, F.d.O. Santos, G. Georgiev, S. Grévy, I. Stefan, J.C. Thomas, N. Adimi, C. Borcea, D.C. Gil, M. Caamano, M. Stanoiu, F. Aksouh, B.A. Brown, L.V. Grigorenko, Phys. Rev. C 72 (2005) 054315.
[164] M. Pfützner, Nuclear Phys. A 738 (2004) 101–107, Proceedings of the 8th International Conference on Clustering Aspects of Nuclear Structure and Dynamics.
[165] L.V. Grigorenko, R.C. Johnson, I.G. Mukha, I.J. Thompson, M.V. Zhukov, Phys. Rev. C 64 (2001) 054002.
[166] L.V. Grigorenko, M.V. Zhukov, Phys. Rev. C 68 (2003) 054005.
[167] L.V. Grigorenko, I.A. Egorova, M.V. Zhukov, R.J. Charity, K. Miernik, Phys. Rev. C 82 (2010) 014615.
[168] J. Giovinazzo, B. Blank, C. Borcea, G. Canchel, J.-C. Dalouzy, C.E. Demonchy, F. de Oliveira Santos, C. Dossat, S. Grévy, L. Hay, J. Huikari, S. Leblanc, I. Matea, J.-L. Pedroza, L. Perrot, J. Pibernat, L. Serani, C. Stodel, J.-C. Thomas, Phys. Rev. Lett. 99 (2007) 102501.
[169] K. Miernik, W. Dominik, Z. Janas, M. Pfützner, L. Grigorenko, C.R. Bingham, H. Czyrkowski, M. Ćwiok, I.G. Darby, R. Dabrowski, T. Ginter, R. Grzywacz, M. Karny, A. Korgul, W. Kuśmierz, S.N. Liddick, M. Rajabali, K. Rykaczewski, A. Stolz, Phys. Rev. Lett. 99 (2007) 192501.
[170] P. Ascher, L. Audirac, N. Adimi, B. Blank, C. Borcea, B.A. Brown, I. Companis, F. Delalee, C.E. Demonchy, F. de Oliveira Santos, J. Giovinazzo, S. Grévy, L.V. Grigorenko, T. Kurtukian-Nieto, S. Leblanc, J.-L. Pedroza, L. Perrot, J. Pibernat, L. Serani, P.C. Srivastava, J.-C. Thomas, Phys. Rev. Lett. 107 (2011) 102502.
[171] T. Goigoux, P. Ascher, B. Blank, M. Gerbaux, J. Giovinazzo, S. Grévy, T. Kurtukian Nieto, C. Magron, P. Doornenbal, G.G. Kiss, S. Nishimura, P.-A. Söderström, V.H. Phong, J. Wu, D.S. Ahn, N. Fukuda, N. Inabe, T. Kubo, S. Kubono, H. Sakurai, Y. Shimizu, T. Sumikama, H. Suzuki, H. Takeda, J. Agramunt, A. Algora, V. Guadilla, A. Montaner-Piza, A.I. Morales, S.E.A. Orrigo, B. Rubio, Y. Fujita, M. Tanaka, W. Gelletly, P. Aguilera, F. Molina, F. Diel, D. Lubos, G. de Angelis, D. Napoli, C. Borcea, A. Boso, R.B. Cakirli, E. Ganioglu, J. Chiba, D. Nishimura, H. Oikawa, Y. Takei, S. Yagi, K. Wimmer, G. de France, S. Go, B.A. Brown, Phys. Rev. Lett. 117 (2016) 162501.
[172] O. Hahn, F. Strassmann, Naturwissenschaften 27 (1939) 11–15.
[173] V. Strutinsky, Nuclear Phys. A 95 (2) (1967) 420–442.
[174] K.-H. Schmidt, B. Jurado, Rep. Progr. Phys. 81 (10) (2018) 106301.
[175] Q. Ducasse, B. Jurado, M. Aïche, P. Marini, L. Mathieu, A. Görgen, M. Guttormsen, A.C. Larsen, T. Tornyi, J.N. Wilson, G. Barreau, G. Boutoux, S. Czajkowski, F. Giacoppo, F. Gunsing, T.W. Hagen, M. Lebois, J. Lei, V. Méot, B. Morillon, A.M. Moro, T. Renstrøm, O. Roig, S.J. Rose, O. Sérot, S. Siem, I. Tsekhanovich, G.M. Tveten, M. Wiedeking, Phys. Rev. C 94 (2) (2016).
[176] A.N. Andreyev, K. Nishio, K.-H. Schmidt, Rep. Progr. Phys. 81 (1) (2017) 016301.
[177] K.-H. Schmidt, S. Steinhuser, C. Bckstiegel, A. Grewe, A. Heinz, A. Junghans, J. Benlliure, H.-G. Clerc, M. de Jong, J. Mller, M. Pftzner, B. Voss, Nuclear Phys. A 665 (3) (2000) 221–267.
[178] G. Kessedjian, B. Jurado, M. Aiche, G. Barreau, A. Bidaud, S. Czajkowski, D. Dassi, B. Haas, L. Mathieu, L. Audouin, N. Capellan, L. Tassan-Got, J. Wilson, E. Berthoumieux, F. Gunsing, C. Theisen, O. Serot, E. Bauge, I. Ahmad, J. Greene, R. Janssens, Phys. Lett. B 692 (5) (2010) 297–301.
[179] J.E. Escher, F.S. Dietrich, Phys. Rev. C 74 (2006) 054601.
[180] K. Nishio, K. Hirose, V. Mark, H. Makii, R. Orlandi, K. Tsukada, M. Asai, A. Toyoshima, T.K. Sato, Y. Nagame, S. Chiba, Y. Aritomo, S. Tanaka, T. Ohtsuki, I. Tsekhanovich, C.M. Petrache, A. Andreyev, EPJ Web Conf. 163 (2017) 00041.

[181] J.E. Escher, J.T. Burke, F.S. Dietrich, N.D. Scielzo, I.J. Thompson, W. Younes, Rev. Modern Phys. 84 (2012) 353–397.
[182] R.J. Casperson, D.M. Asner, J. Baker, R.G. Baker, J.S. Barrett, N.S. Bowden, C. Brune, J. Bundgaard, E. Burgett, D.A. Cebra, T. Classen, M. Cunningham, J. Deaven, D.L. Duke, I. Ferguson, J. Gearhart, V. Geppert-Kleinrath, U. Greife, S. Grimes, E. Guardincerri, U. Hager, C. Hagmann, M. Heffner, D. Hensle, N. Hertel, D. Higgins, T. Hill, L.D. Isenhower, J. King, J.L. Klay, N. Kornilov, R. Kudo, A.B. Laptev, W. Loveland, M. Lynch, W.S. Lynn, J.A. Magee, B. Manning, T.N. Massey, C. McGrath, R. Meharchand, M.P. Mendenhall, L. Montoya, N.T. Pickle, H. Qu, J. Ruz, S. Sangiorgio, K.T. Schmitt, B. Seilhan, S. Sharma, L. Snyder, S. Stave, A.C. Tate, G. Tatishvili, R.T. Thornton, F. Tovesson, D.E. Towell, R.S. Towell, N. Walsh, S. Watson, B. Wendt, L. Wood, L. Yao, W. Younes, NIFFTE Collaboration, Phys. Rev. C 97 (2018) 034618.
[183] M. Petit, M. Aiche, G. Barreau, S. Boyer, N. Carjan, S. Czajkowski, D. Dassi, C. Grosjean, A. Guiral, B. Haas, D. Karamanis, S. Misicu, C. Rizea, F. Saintamon, S. Andriamonje, E. Bouchez, F. Gunsing, A. Hurstel, Y. Lecoz, R. Lucas, C. Theisen, A. Billebaud, L. Perrot, E. Bauge, Nuclear Phys. A 735 (3) (2004) 345–371.
[184] C. Rodríguez-Tajes, F. Farget, X. Derkx, M. Caamaño, O. Delaune, K.-H. Schmidt, E. Clément, A. Dijon, A. Heinz, T. Roger, L. Audouin, J. Benlliure, E. Casarejos, D. Cortina, D. Doré, B. Fernández-Domínguez, B. Jacquot, B. Jurado, A. Navin, C. Paradela, D. Ramos, P. Romain, M.D. Salsac, C. Schmitt, Phys. Rev. C 89 (2014) 024614.
[185] M. Veselsky, J. Klimo, N. Vujisicova, G.A. Souliotis, Opportunities for nuclear reaction studies at future facilities, 2016, arXiv:1604.01961 [nu-exp].
[186] R.N. Sahoo, M. Kaushik, A. Sood, P. Kumar, V.R. Sharma, A. Yadav, P.P. Singh, M.K. Sharma, R. Kumar, B.P. Singh, S. Aydin, R. Prasad, Nuclear Phys. A 983 (2019) 145–165.
[187] D. Ackermann, P. Bednarczyk, L. Corradi, D. Napoli, C. Petrache, P. Spolaore, A. Stefanini, K. Varier, H. Zhang, F. Scarlassara, S. Beghini, G. Montagnoli, L. Müller, G. Segato, F. Soramel, C. Signorini, Nuclear Phys. A 609 (1) (1996) 91–107.
[188] P.-W. Wen, Z.-Q. Feng, F. Zhang, C. Li, C.-J. Lin, F.-S. Zhang, Chin. Phys. C 41 (6) (2017) 064102.
[189] A. Shrivastava, A. Navin, A. Diaz-Torres, V. Nanal, K. Ramachandran, M. Rejmund, S. Bhattacharyya, A. Chatterjee, S. Kailas, A. Lemasson, R. Palit, V. Parkar, R. Pillay, P. Rout, Y. Sawant, Phys. Lett. B 718 (3) (2013) 931–936.
[190] H. Wang, H. Otsu, N. Chiga, S. Kawase, S. Takeuchi, T. Sumikama, S. Koyama, H. Sakurai, Y. Watanabe, S. Nakayama, D.S. Ahn, H. Baba, S.D. Chen, K. Chikaato, M.L. Cortés, N. Fukuda, A. Hirayama, R. Hosoda, T. Isobe, S. Kawakami, Y. Kondo, S. Kubono, Y. Maeda, S. Masuoka, S. Michimasa, I. Murray, R. Nakajima, T. Nakamura, K. Nakano, M. Nishimura, T. Ozaki, A. Saito, T. Saito, H. Sato, Y. Shimizu, S. Shimoura, P.A. Söderström, Y. Soudo, X.H. Sun, J. Suwa, D. Suzuki, H. Suzuki, H. Takeda, M. Takechi, Y. Togano, T. Tomai, H. Yamada, M. Yasuda, K. Yoshida, Commun. Phys. 2 (1) (2019) 78.
[191] A. Lemasson, A. Shrivastava, A. Navin, M. Rejmund, N. Keeley, V. Zelevinsky, S. Bhattacharyya, A. Chatterjee, G. de France, B. Jacquot, V. Nanal, R.G. Pillay, R. Raabe, C. Schmitt, Phys. Rev. Lett. 103 (2009) 232701.
[192] A.M. Vinodkumar, W. Loveland, R. Yanez, M. Leonard, L. Yao, P. Bricault, M. Dombsky, P. Kunz, J. Lassen, A.C. Morton, D. Ottewell, D. Preddy, M. Trinczek, Phys. Rev. C 87 (2013) 044603.
[193] J. Kolata, A. Howard, W. Mittig, T. Ahn, D. Bazin, F. Becchetti, S. Beceiro-Novo, Z. Chajecki, M. Febbrarro, A. Fritsch, W. Lynch, A. Roberts, A. Shore, R. Torres-Isea, Nucl. Instrum. Methods Phys. Res. A 830 (2016) 82–87.
[194] M. Cortesi, S. Rost, W. Mittig, Y. Ayyad-Limonge, D. Bazin, J. Yurkon, A. Stolz, Rev. Sci. Instrum. 88 (1) (2017) 013303.
[195] J.L. Fisker, H. Schatz, F.-K. Thielemann, Astrophys. J. Suppl. Ser. 174 (1) (2008) 261–276.
[196] R.H. Cyburt, A.M. Amthor, A. Heger, E. Johnson, L. Keek, Z. Meisel, H. Schatz, K. Smith, Astrophys. J. 830 (2) (2016) 55.
[197] J. Pereira, F. Montes, Phys. Rev. C 93 (2016) 034611.
[198] W.A. Fowler, Rev. Modern Phys. 56 (1984) 149–179.
[199] B. DiGiovine, D. Henderson, R. Holt, R. Raut, K. Rehm, A. Robinson, A. Sonnenschein, G. Rusev, A. Tonchev, C. Ugalde, Nucl. Instrum. Methods Phys. Res. A 781 (2015) 96–104.
[200] J.M. Blatt, V.F. Weisskopf, Theoretical Nuclear Physics, Courier Corporation, 1991.
[201] M. Gai, M.W. Ahmed, S.C. Stave, W.R. Zimmerman, A. Breskin, B. Bromberger, R. Chechik, V. Dangendorf, T. Delbar, R.H. France, S.S. Henshaw, T.J. Kading, P.P. Martel, J.E.R. McDonald, P.N. Seo, K. Tittelmeier, H.R. Weller, A.H. Young, J. Instrum. 5 (12) (2010) P12004–P12004.
[202] Y. Ayyad, M. Cortesi, W. Mittig, D. Bazin, J. Instrum. 12 (06) (2017) P06003–P06003.
[203] H. Schatz, K. Rehm, Nuclear Phys. A 777 (2006) 601–622, Special Isseu on Nuclear Astrophysics.
[204] A. Heger, A. Cumming, D.K. Galloway, S.E. Woosley, Astrophys. J. 671 (2) (2007) L141–L144.
[205] Z. Meisel, Astrophys. J. 860 (2) (2018) 147.
[206] Z. Meisel, G. Merz, S. Medvid, Astrophys. J. 872 (1) (2019) 84.
[207] Z. Meisel, A. Deibel, L. Keek, P. Shternin, J. Elfritz, J. Phys. G: Nucl. Part. Phys. 45 (9) (2018) 093001.
[208] M.L. Avila, K.E. Rehm, S. Almaraz-Calderon, A.D. Ayangeakaa, C. Dickerson, C.R. Hoffman, C.L. Jiang, B.P. Kay, J. Lai, O. Nusair, R.C. Pardo, D. Santiago-Gonzalez, R. Talwar, C. Ugalde, Phys. Rev. C 94 (2016) 065804.
[209] S. Almaraz-Calderon, P.F. Bertone, M. Alcorta, M. Albers, C.M. Deibel, C.R. Hoffman, C.L. Jiang, S.T. Marley, K.E. Rehm, C. Ugalde, Phys. Rev. Lett. 112 (2014) 152701.
[210] Z. Meisel, G. Merz, S. Medvid, Astrophys. J. 872 (1) (2019) 84.
[211] A. Matic, A.M. van den Berg, M.N. Harakeh, H.J. Wörtche, M. Beard, G.P.A. Berg, J. Görres, P. LeBlanc, S. O'Brien, M. Wiescher, K. Fujita, K. Hatanaka, Y. Sakemi, Y. Shimizu, Y. Tameshige, A. Tamii, M. Yosoi, T. Adachi, Y. Fujita, Y. Shimbara, H. Fujita, T. Wakasa, J.P. Greene, R. Crowter, H. Schatz, Phys. Rev. C 84 (2011) 025801.
[212] J.S. Randhawa, Y. Ayyad, W. Mittig, Z. Meisel, et al., First direct measurement of ^{22}mg(α,p)^{25}al and implications for x-ray burst model-observation comparisons, 2020, arXiv:2001.06087.
[213] M. Avila, Priv. Comm.
[214] NNDC, 2019, https://www.nndc.bnl.gov/.
[215] F. Becchetti, J. Kolata, Nucl. Instrum. Methods Phys. Res. B 376 (2016) 397–401, Proceedings of the XVIIth International Conference on Electromagnetic Isotope Separators and Related Topics (EMIS2015), Grand Rapids, MI, U.S.A., 11-15 May 2015.
[216] M. Cortesi, J. Yurkon, W. Mittig, D. Bazin, S. Beceiro-Novo, A. Stolz, J. Instrum. 10 (09) (2015) P09020–P09020.
[217] B. Davids, R.H. Cyburt, J. José, S. Mythili, Astrophys. J. 735 (1) (2011) 40.
[218] K.E. Rehm, A.H. Wuosmaa, C.L. Jiang, J. Caggiano, J.P. Greene, A. Heinz, D. Henderson, R.V.F. Janssens, E.F. Moore, G. Mukherjee, R.C. Pardo, T. Pennington, J.P. Schiffer, R.H. Siemssen, M. Paul, L. Jisonna, R.E. Segel, Phys. Rev. C 67 (2003) 065809.
[219] C. Wrede, B.E. Glassman, D. Pérez-Loureiro, J.M. Allen, D.W. Bardayan, M.B. Bennett, B.A. Brown, K.A. Chipps, M. Febbraro, C. Fry, M.R. Hall, O. Hall, S.N. Liddick, P. O'Malley, W.-J. Ong, S.D. Pain, S.B. Schwartz, P. Shidling, H. Sims, P. Thompson, H. Zhang, Phys. Rev. C 96 (2017) 032801.
[220] M. Friedman, T. Budner, D. Pérez-Loureiro, E. Pollacco, C. Wrede, J. José, B.A. Brown, M. Cortesi, C. Fry, B. Glassman, J. Heideman, M. Janasik, M. Roosa, J. Stomps, J. Surbrook, P. Tiwari, Phys. Rev. C 101 (2020) 052802.
[221] S. Seuthe, C. Rolfs, U. Schrder, W. Schulte, E. Somorjai, H. Trautvetter, F. Waanders, R. Kavanagh, H. Ravn, M. Arnould, G. Paulus, Nuclear Phys. A 514 (3) (1990) 471–502.
[222] A.L. Sallaska, C. Wrede, A. García, D.W. Storm, T.A.D. Brown, C. Ruiz, K.A. Snover, D.F. Ottewell, L. Buchmann, C. Vockenhuber, D.A. Hutcheon, J.A. Caggiano, Phys. Rev. Lett. 105 (2010) 152501.

[223] A. Saastamoinen, L. Trache, A. Banu, M.A. Bentley, T. Davinson, J.C. Hardy, V.E. Iacob, M. McCleskey, B.T. Roeder, E. Simmons, G. Tabacaru, R.E. Tribble, P.J. Woods, J. Äystö, Phys. Rev. C 83 (2011) 045808.
[224] T. Taddeucci, C. Goulding, T. Carey, R. Byrd, C. Goodman, C. Gaarde, J. Larsen, D. Horen, J. Rapaport, E. Sugarbaker, Nuclear Phys. A 469 (1) (1987) 125–172.
[225] M. Sasano, G. Perdikakis, R.G.T. Zegers, S.M. Austin, D. Bazin, B.A. Brown, C. Caesar, A.L. Cole, J.M. Deaven, N. Ferrante, C.J. Guess, G.W. Hitt, M. Honma, R. Meharchand, F. Montes, J. Palardy, A. Prinke, L.A. Riley, H. Sakai, M. Scott, A. Stolz, T. Suzuki, L. Valdez, K. Yako, Phys. Rev. C 86 (2012) 034324.
[226] R. Meharchand, R.G.T. Zegers, B.A. Brown, S.M. Austin, T. Baugher, D. Bazin, J. Deaven, A. Gade, G.F. Grinyer, C.J. Guess, M.E. Howard, H. Iwasaki, S. McDaniel, K. Meierbachtol, G. Perdikakis, J. Pereira, A.M. Prinke, A. Ratkiewicz, A. Signoracci, S. Stroberg, L. Valdez, P. Voss, K.A. Walsh, D. Weisshaar, R. Winkler, Phys. Rev. Lett. 108 (2012) 122501.
[227] R.G.T. Zegers, R. Meharchand, Y. Shimbara, S.M. Austin, D. Bazin, B.A. Brown, C.A. Diget, A. Gade, C.J. Guess, M. Hausmann, G.W. Hitt, M.E. Howard, M. King, D. Miller, S. Noji, A. Signoracci, K. Starosta, C. Tur, C. Vaman, P. Voss, D. Weisshaar, J. Yurkon, Phys. Rev. Lett. 104 (2010) 212504.
[228] T. Ichihara, T. Niizeki, H. Okamura, H. Ohnuma, H. Sakai, Y. Fuchi, K. Hatanaka, M. Hosaka, S. Ishida, K. Kato, S. Kato, H. Kawashima, S. Kubono, S. Miyamoto, H. Orihara, N. Sakamoto, S. Takaku, Y. Tajima, M. Tanaka, H. Toyokawa, T. Uesaka, T. Yamamoto, T. Yamashita, M. Yosoi, M. Ishihara, Nuclear Phys. A 569 (1) (1994) 287–296.
[229] S. Rakers, C. Bäumer, D. Frekers, R. Schmidt, A.M. van den Berg, V.M. Hannen, M.N. Harakeh, M.A. de Huu, H.J. Wörtche, D. De Frenne, M. Hagemann, J. Heyse, E. Jacobs, Y. Fujita, Phys. Rev. C 65 (2002) 044323.
[230] G. Alkhazov, S. Belostotsky, A. Vorobyov, Phys. Rep. 42 (2) (1978) 89–144.
[231] L.A. Riley, D. Bazin, J. Belarge, P.C. Bender, B.A. Brown, P.D. Cottle, B. Elman, A. Gade, S.D. Gregory, E.B. Haldeman, K.W. Kemper, B.R. Klybor, M.A. Liggett, S. Lipschutz, B. Longfellow, E. Lunderberg, T. Mijatovic, J. Pereira, L.M. Skiles, R. Titus, A. Volya, D. Weisshaar, J.C. Zamora, R.G.T. Zegers, Phys. Rev. C 100 (2019) 044312.
[232] L.X. Chung, C.A. Bertulani, P. Egelhof, S. Ilieva, D.T. Khoa, O.A. Kiselev, Phys. Lett. B 774 (2017) 559–563.
[233] M. von Schmid, S. Bagchi, S. Bönig, M. Csatlós, I. Dillmann, C. Dimopoulou, P. Egelhof, V. Eremin, T. Furuno, H. Geissel, R. Gernhäuser, M.N. Harakeh, A.-L. Hartig, S. Ilieva, N. Kalantar-Nayestanaki, O. Kiselev, H. Kollmus, C. Kozhuharov, A. Krasznahorkay, T. Kröll, M. Kuilman, S. Litvinov, Y.A. Litvinov, M. Mahjour-Shafiei, M. Mutterer, D. Nagae, M.A. Najafi, C. Nociforo, F. Nolden, U. Popp, C. Rigollet, S. Roy, C. Scheidenberger, M. Steck, B. Streicher, L. Stuhl, M. Thürauf, T. Uesaka, H. Weick, J.S. Winfield, D. Winters, P.J. Woods, T. Yamaguchi, K. Yue, J.C. Zamora, J. Zenihiro, EXL collaboration, Phys. Scr. T 166 (2015) 014005.
[234] U. Garg, G. Colò, Prog. Part. Nucl. Phys. 101 (2018) 55–95.
[235] B.A. Li, A.W. Steiner, Phys. Lett. B 642 (5–6) (2006) 436–440.
[236] C. Monrozeau, E. Khan, Y. Blumenfeld, C.E. Demonchy, W. Mittig, P. Roussel-Chomaz, D. Beaumel, M. Caamaño, D. Cortina-Gil, J.P. Ebran, N. Frascaria, U. Garg, M. Gelin, A. Gillibert, D. Gupta, N. Keeley, F. Maréchal, A. Obertelli, J.-A. Scarpaci, Phys. Rev. Lett. 100 (2008) 042501.
[237] M. Vandebrouck, J. Gibelin, E. Khan, N.L. Achouri, H. Baba, D. Beaumel, Y. Blumenfeld, M. Caamaño, L. Càceres, G. Colò, F. Delaunay, B. Fernandez-Dominguez, U. Garg, G.F. Grinyer, M.N. Harakeh, N. Kalantar-Nayestanaki, N. Keeley, W. Mittig, J. Pancin, R. Raabe, T. Roger, P. Roussel-Chomaz, H. Savajols, O. Sorlin, C. Stodel, D. Suzuki, J.C. Thomas, Phys. Rev. Lett. 113 (2014) 032504.